The Modern and Glacial Thermoclines along the Bahama Banks

by

Niall Charles Slowey

M.S. University of North Carolina, 1986
B.S. Tufts University, 1980

Submitted in partial fulfillment of the
requirements for the degree of

Doctor of Philosophy

at the

MASSACHUSETTS INSTITUTE OF TECHNOLOGY

and the

WOODS HOLE OCEANOGRAPHIC INSTITUTION

September 1990

Signature of Author .....
Joint Program in Oceanography
Massachusetts Institute of Technology
Woods Hole Oceanographic Institution
September 21, 1990

Certified by .....
William B. Curry
Associate Scientist
Thesis Supervisor

Accepted by .....
G. P. Lohmann
Chairman, Joint Committee for Marine Geology and Geophysics

Contents

0.1 Acknowledgments 5

1 On the hydrography of the Providence Channels, Bahamas **6**

1.1 Introduction 6

1.2 Data 7

1.3 Results and Discussion 8

1.4 Acknowledgements 10

1.5 References 11

1.6 Tables 13

1.7 Figure Captions 17

1.8 Figures 18

2 Structure of the glacial thermocline at Little Bahama Bank **37**

3 Physical structure and carbon cycling within the glacial thermocline of the western subtropical North Atlantic **42**

3.1 Heading 42

3.2 Introduction 42

3.3 Geologic and oceanographic setting 43

3.4 Methods and core stratigraphies 45

3.5 Ventilation and nutrient concentrations 48

3.6 Temperature gradient 51

3.7 Intermediate depth waters 52

3.8 Summary and speculation 54

3.9 References 55

3.10 Figure captions 60
3.11 Figures 62
3.12 Tables 73
3.13 Appendix A. Determining the carbonate mineralogy of sediments 92
3.13.1 References 93
3.13.2 Tables, Figure and Computer Program 94

4 Using ^{230}Th or ^{231}Pa in marine sediments to reconstruct the late Quaternary history of sea level 100

4.1 Abstract 100
4.2 Introduction 101
4.3 ^{230}Th and ^{231}Pa in the Ocean 103
4.4 Effect of Sea-level Change on ^{230}Th and ^{231}Pa Flux 105
4.5 Reconstructing Sea-level History 105
4.5.1 Approach 1: one core 106
4.6 Summary 112
4.7 Acknowledgements 113
4.8 References 114
4.9 Tables 118
4.10 Figure captions 121
4.11 Figures 122

The Modern and Glacial Thermoclines along the Bahama Banks

by

Niall Charles Slowey

Submitted to the Massachusetts Institute of Technology–
Woods Hole Oceanographic Institution
Joint Program in Oceanography
on September 21, 1990, in partial fulfillment of the
requirements for the degree of
Doctor of Philosophy

Abstract

As a primary feature of ocean circulation and a key component of the global carbon cycle, changes in the thermocline must be accounted for if we are to understand the processes involved in Quaternary climatic fluctuation. Toward this goal, this thesis contains studies of the modern and glacial thermoclines at the Bahama Banks and it presents an novel approach to determine sea level based on the flux of ^{230}Th and 231Pa from thermocline waters to the seafloor.

In the first chapter, the hydrography of the modern thermocline in Northwest and Northeast Providence Channels, Bahamas, is investigated using CTD data. Potential temperature–salinity relationships demonstrate that the deep waters and most of the thermocline waters in these channels originates in the Sargasso Sea. Cross channel sections of water properties suggest the following: (1) water from the shallow core of the Deep Western Boundary Current (Fine and Molinari, 1988) may circulate along the channel margins, and (2) where the western end of Northwest Providence Channel opens to the Florida Straits, shallow flow is toward the straits in the southern portion of the channel and away from the straits in the northern portion.

In the next two chapters, changes in the temperature and nutrient structures of the thermocline from the last glaciation to the recent Holocene are inferred from isotopic variations of the planktonic foraminifera *Globigerinoides ruber* (212–250 μm) and *G. sacculifer* (300–350 μm) and the benthic foraminifera *Planulina wuellerstorfi*, *P. ariminensis*, *P. foveolata* and *Cibicidoides pachyderma* (>250μm) in a suite of cores from the margins of Little and Great Bahama Banks. During the last glaciation, δ^{18}O values were from 1.4 to 1.9 per mil greater than during the recent Holocene. Based on the δ^{18}O/sea-level model of Fairbanks (1989), we estimate that the upper 1500 m of the water column was cooler by at least 1 °C—the deepest waters were several degrees cooler. The temperature gradient (dT/dz) was steeper and the base of the thermocline appears to have stayed at about the same depth or risen slightly. At all depths in the thermocline, δ^{13}C was greater during the last glaciation than during the recent Holocene by at least 0.1–0.2 per mil and as much as 0.6 per mil in the lower thermocline. While recent Holocene δ^{13}C reaches minimum values in the lower thermocline (the poorly-ventilated oxygen minimum/phosphate maximum layer), this feature was not present during the last glaciation. These data show that the concentrations of

nutrients throughout the thermocline were reduced and that there was no oxygen minimum layer, indicating greater, more uniform ventilation of thermocline waters.

These results are consistent with our understanding of the physics of thermocline circulation and evidence for hydrographic conditions at the ocean surface during the last glaciation, indicating a direct response of thermocline circulation to changes in climate. Cooler thermocline waters reflect cooler surface ocean temperatures at mid-latitudes where thermocline isopycnal surfaces outcrop. Increased, more uniform ventilation of the glacial thermocline is consistent with both more vigorous glacial winds leading to increased Ekman pumping and all isopycnal surfaces of the thermocline outcropping in the area of Ekman downwelling. Taken together with previous studies of intermediate-depth waters, these data document that the entire upper water column of the North Atlantic was depleted in nutrients during the last glaciation. A final suggestion of the third study is that Mediterranean and southern source waters contributed little to deeper intermediate-depth waters in the North Atlantic.

The fourth chapter presents two new approaches to reconstruct the sea-level history based on the fluxes of ^{230}Th and ^{231}Pa to the seafloor. The approaches rely on the fact that fluxes of these nuclides to a site on the seafloor are proportional to the height of the water column above the site. Consequently, a change in sea level causes changes in the ^{230}Th and ^{231}Pa fluxes which, at shallow sites, are large fractions of the total fluxes. Past sea level can be reconstructed using either the record of nuclide accumulation in a single core of sediment, or nuclide concentrations in synchronously deposited sediment samples from cores collected over a range of water depths. Importantly, this record of sea level is both continuous (not just high stands) and independent of the assumptions of constant seawater temperature or uplift rate required by some other approaches.

Thesis Supervisor: William B. Curry
Title: Associate Scientist

0.1 Acknowledgments

I thank Bill Curry for providing encouragement, support and sound advice during the course of this thesis as well as an example of thorough but efficient science. I thank my committee members, Mike Bacon, Ed Boyle, Lloyd Keigwin and Pat Lohmann, for willingly sharing their interest, insight and time.

Many people have assisted in sample collection and laboratory analyses. In particular, Rindy Ostermann has helped out in a wide range of activities. This thesis would not have been possible without the efforts of the captain, the crew, the scientific party and, especially, Jim Broda during *RV Oceanus* cruise 205-2. Bill Berggren, C. Chen, Julie Cole, Tom Davis, Alan Fleer, Eben Franks, Al Gagnon, Sheila Griffin, Lloyd Keigwin, Glenn Jones, Peter Mills, Amy Pallant, Wylie Poag, Peter Schweitzer and David Walsh have provided instruction or assistance in the lab. Chris Charles and Rick Fairbanks of Lamont-Doherty kindly provided some isotope analyses. Dawn Lavoie, Hank Mullins, Conrad Neumann and Cindy Pilskaln either provided samples or cruise time to try and collect them.

I have benefitted from discussions with many other present and former WHOI staff while working on this thesis, particularly Bill Jenkins, Mike McCartney, Dan McCorkle, John Milliman, David Musgrave, Delia Oppo, Brian Tucholke and Bruce Warren.

Abbie Jackson and Jake Pierson of the Education Office have always been very helpful.

As the end of this thesis is in sight, I am very thankful for my fellow students, scientists, friends and family whose kindness, support and good cheer have meant more to me than they will ever know. Most of all, I thank Michelle, Shane and Alison whose love has always been with me.

This work was supported by NSF grant number OCE-8813307 to W. Curry, NSF grant number OCE-8800693 to J. Broda and W. Curry and the Education Office of the MIT/WHOI Joint Program in Oceanography.

Chapter 1

On the hydrography of the Providence Channels, Bahamas

1.1 Introduction

Northeast Providence Channel (NEPC) and Northwest Providence Channel (NWPC) form an open-ended seaway which separates Little and Great Bahama Banks (Figure 1). For both physical oceanographic and geologic reasons, the hydrography of this seaway is of interest. It connects the western North Atlantic basin with the Straits of Florida and so is a site for the exchange of water between the Sargasso Sea and the Florida Current (e.g. Wennekens, 1959; Richardson and Finlen, 1967; Richardson et al., 1969; Leaman and Molinari, 1987). In addition, the circulation and chemistry of the water within the channels influence the deposition and diagenesis of peri-platform carbonate ooze on the floor of the channels (e.g. Boardman and Neumann, 1984; Droxler et al., 1988; Pilskaln et al., 1989).

Based upon temperature–salinity and nutrient–density relationships, Smith (1940) and Wennekens (1959) identified the western North Atlantic as the source of waters found deeper than about 250 m in the Providence Channels and implied a dominant western flow. Net western flow is consistent with short-term direct transport measurements made across the western end of NWPC (Richardson and Finlen, 1967) and increased transport of the Florida Current after it passes NWPC (Richardson et al., 1969; Leaman and Molinari, 1987).

Short-term measurements of the current structure across the channels (limited to the western end of NWPC) do not form a consistent picture. Richardson and Finlen (1967) observed easterly flow in the southern side (away from the Florida Straits) and westerly

flow in the northern side (toward the Florida Straits). Current meters deployed along the southern shore of Grand Bahama Island (Lee, 1977) also showed near surface currents with a mean flow toward the west, but with frequent reversals. In contast, the reverse pattern (i.e. flow toward the straits in southern side of NWPC and flow away from the straits in the northern side) is apparent in Acoustic Doppler Current Profiler sections by Leaman and Molinari (1987). Current measurements from the submarine NR-1 and dipping isotherms on a temperature section across the southern side of NWPC also indicate westward flow (Gardner et al., 1989). Finally, current meters deployed at 450 and 550 m depth along the axis of western NWPC showed dominant westward flow, though there was significant variability in the northward component of velocity (Pilskaln, et al., 1989).

Here we describe a suite of CTD profiles that bear on the hydrography of the Providence Channels. The previously suggested origin of main thermocline and deep waters within the channels is confirmed by comparison of their potential temperature–salinity (θ–S) relationships with those of waters within the adjacent Florida Straits and Sargasso Sea. Water properties and geostrophic velocities in several sections across the channels are described and provide insight into the pattern of water circulation.

1.2 Data

During *RV Oceanus* cruise 205–2 in December, 1988, hydrographic data was collected from both Providence Channels (Figure 2 and Table 1). CTD casts were made to a maximum depth of ~2000 m using a Sea-Bird Electronics model SBE 19 profiler with a Paroscientific Digiquartz pressure transducer.

A difference in the response times of conductivity and temperature sensors in a CTD results in salinity bias and spikes (e.g. Ochoa, 1989). To compensate for the difference that exists in our CTD, a range of advances were applied to the raw conductivity data in one profile (Figure 3) and the value which minimized salinity spikes (-0.4 sec) was applied to the raw conductivity data in all profiles. Raw data were then sorted into 2 db bins and averaged before physical properties were calculated. Data processing was carried out using software provided by Sea-Bird (version 3.2B) which utilizes the algorithims of UNESCO technical paper #44 (Fofonoff and Millard, 1983).

Salinity, temperature and pressure sensors were calibrated two weeks before the start of the cruise and were again calibrated 9 weeks after the finish. There was no significant change in the sensitivity of the temperature sensor, but the sensitivity of the conductivity sensor did drift between calibrations. A systematic pattern to this drift could not be discerned from the θ–S relationships of casts made at different times during the cruise, so no attempt was made to correct for drift in a systematic way. Instead, the average of the pre- and post-cruise calibrations was utilized. Considering both calibration uncertainties and the precision of the sensors listed by Sea-Bird, we believe that temperatures and salinities are accurate to about ± 0.003°C and ± 0.01 ppt, respectively.

CTD data for both the Florida Straits and the Sargasso Sea (Tables 2 and 3) were collected during *RV Atlantis II* cruise 109 (Roemmich and Wunsch, 1985) and *RV Endeavor* cruise 129 (Knapp, 1988). For these data, salinities are believed accurate to ± 0.003 ppt and temperatures are believed accurate to ± 0.002°C.

1.3 Results and Discussion

Situated at either end of the seaway formed by the Providence Channels, the Sargasso Sea and the Florida Straits are the two possible sources for waters found within the channels. Figure 4 shows the θ–S relationships for individual stations in the Florida Straits (just south of the western entrance to NWPC) and the Sargasso Sea. Though warm, shallow waters from both regions cannot be distinguished on the basis of θ–S characteristics, for $\theta \leq 15.5$°C, waters in the Sargasso Sea are consistently about 0.1 ppt saltier than in the Florida Straits. This subtle but significant difference makes it possible to determine the relative contributions from these two potential sources to main thermocline and deep waters within the Providence Channels.

The θ–S relationships at stations throughout the Providence Channels (Figure 5) fall on a relatively tight curve, indicating that thermocline and deep waters in all parts of the Providence Channels have a similar origin. Where this curve lies between Sargasso Sea and Florida Straits waters on a θ–S plot is proportional to the relative contributions of these two potential sources of water to the channels. θ–S relationships for these waters are plotted together in Figure 6. It is clear that the characteristics of channel waters with temperatures

$\leq$15.5°C ($\geq$500 m) are the same as that of Sargasso Sea waters—not intermediate between those of the Sargasso Sea and Florida Straits—so their source must be the Sargasso Sea alone.

Sections 1 and 2 are located at the eastern end of the seaway where it is relatively deep and opens into the Sargasso Sea (see Figure 2). Isopleths of temperature, salinity and density (Figures 7 and 8) generally have little slope across these sections; there is little lateral variation in water properties. Isopleths do dip slightly from the axis of the channel to the edges and preliminary geostrophic calculations (calculated assuming zero velocity at the greatest depth common to adjacent CTD profiles) indicates flow of about 10–20 cm/sec over the depth range of about 1000 to 1500 m (θ: ~4–6°C, S: ~35.0–35.1 ppt), indicating the presence of a westward flowing boundary current on the northern side of the channel and a eastward flowing boundary current on the southern side. A deep western boundary current (Labrador Sea type water) at the same depths and with similar physical property and velocity characteristics flows along the western margin of the North Atlantic basin and passes by the eastern margin of Little Bahama Bank (Olsen et al., 1984; Wilburn et al., 1987; Fine and Molinari, 1988). Our observations suggest that this current does not jump completely across the entrance to NEPC but at least a portion of it hugs topography—entering, traveling around and then exiting the Providence Channels before it continues southward.

Section 3 crosses the western end of NWPC where it opens into the Florida Straits (Figure 9). The depths of isopleths are about the same as in sections 1 and 2 indicating that there is little slope to isopleths along the axis of the channel and between the channel and the Sargasso Sea (see Roemmich and Wunsch, 1985, for comparison). In contrast, Luyten and Stommel (1984) note that the depths of temperature and density surfaces in the Sargasso Sea are about 100 m deeper than in the rapidly flowing, confined current in the Florida Straits. In waters shallower than about 300 m, isopleths are closely spaced and dip from the edges of the channel towards its axis. This pattern implies eastward flow in the northern portion of the channel and westward flow in the southern portion of the channel—consistent with the observations of Leaman and Molinari (1987) and Gardner et al. (1989) and in contrast to those of Richardson and Finlen (1967) and Lee (1977).

In summary, θ–S relationships of thermocline and deeper waters within the Providence Channels are consistent with a Sargasso Sea origin. Cross channel sections of water properties indicate that the lateral distribution of waters within the channels is generally homogeneous. These properties suggest two notable features of current flow within the channels. First, at the western end of NWPC, there is eastward flow in the northern portion of the channel and westward flow in the southern portion. Second, a portion of the North Atlantic deep western boundary current (core at ~1250 m) flows along the margins of NEPC and NWPC.

1.4 Acknowledgements

J. Broda helped obtain the CTD. We thank the captain, crew and scientific party of the *RV Oceanus* during cruise 205–2 for their efforts in collecting CTD profiles. R. Curry provided access to *RV Atlantis II* 109 and *RV Endeavor* 129 CTD data. We are especially indebted to C. Chen for helpful discussions and assistance with computer programs. We thank R. Kirshfield, M. McCartney, R. Millard, D. Walsh and B. Warren for helpful discussions. D. Ostermann maintained the CTD and aided in figure preparation. This work was supported by NSF grant OCE-8813307.

1.5 References

Boardman, M. R., and Neumann, A. C., 1984, Sources and cycles of off-bank carbonates: Northwest Providence Channel, Bahamas: Journal of Sedimentary Petrology, v. 54, p. 1110–1123.

Droxler, A. W., Morse, J. W., and Kornicker, W. A., 1986, Controls on carbonate mineral accumulation in Bahamian basins and adjacent Atlantic Ocean sediments: Journal of Sedimentary Petrology, v. 58, 54, p. 120–130.

Fine, R. A., and Molinari, R. L., 1988, A continuous deep western boundary current between Abaco (26.5°N) and Barbados (13°N): Deep-Sea Research, v. 35, p. 1441–1450.

Fofonoff, N. P., and Millard, R. C., Jr., 1983, Algorithms for computation of fundamental properties of seawater: Unesco Technical Papers in Marine Science, v. 44, 53 pp.

Gardner, W. D., Richardson, M. J., and Cacchione, D. A., 1989, Sedimentological effects of strong southward flow in the Straits of Florida: Marine Geology, v. 86, p. 155–180.

Gardner, W. D., Richardson, M. J., and Cacchione, D. A., 1989, Sedimentological effects of strong southward flow in the Straits of Florida: Marine Geology, v. 86, p. 155–180.

Knapp, G. P., 1988, Hydrographic data from *RV Endeavor* cruise 129: Woods Hole Oceanographic Institution Technical Report, WHOI–88–41, 111 p.

Leaman, K. D., and Molinari, R. L., 1987, Topographic modification of the Florida Current by Little Bahama Bank and Great Bahama Banks: Journal of Physical Oceanography, v. 17, p. 1724–1736.

Lee, N. T., 1977, Coastal currents along the southern shore of Grand Bahama Island: Bulletin of Marine Science, v. 27, p. 802–820.

Luyten, J., and Stommel, H., 1984, The density jump across Little Bahama Bank: Journal of Geophysical Research, v. 89, p. 2097–2100.

Ochoa, J., 1989, A practical determination of CTD platimum resistence thermometer response time, and its use to correct salinity bias and spikes: Deep-Sea Research, v. 36, p. 139–148.

Olson, D. B., Schott, F. A., Zantopp, R. J., and Leaman, K. D., 1984, The mean circulation east of the Bahamas as determined from a recent measurement program and historical XBT data: Journal of Physical Oceanography, v. 14, p. 1470–1487.

Pilskaln, C. H., Neumann, A. C., and Bane, J. M., 1989, Periplatform carbonate flux in the northern Bahamas: Deep-Sea Research, v. 26, p. 1391–1406.

Richarson, W. S., and Finlen, J. R., 1967, The transport of Northwest Providence Channel: Deep-Sea Research, v. 14, p. 361–367.

Richarson, W. S., Schmitz, W. J., and Niiler, P. P., The velocity structure of the Florida Current from the Straits of Florida to Cape Fear: Deep-Sea Research, v. 16, p. 225–231.

Roemmich, D., and Wunsch, C., 1985, Two transatlantic sections: meridional circulation and heat flux in the subtropical North Atlantic Ocean: Deep-Sea Research, v. 32, p. 619–664.

Smith, C. L., 1940, The Great Bahama Bank. I. General hydrographic and chemical features: Journal of Marine Research, v. 3, p. 147–170.

Wennekens, M. P., 1959, Water mass properties of the Straits of Florida and related waters: Bulletin of Marine Science of the Gulf and Caribbean, v. 9, p. 1–52.

Wilburn, A. M., Johns, E., and Bushnell, M., Current velocity and hydrographic observations in the Straits of Florida, The Caribbean Sea and offshore of the Antillean Archipelago: Subtropical Atlantic Climate Studies (STACS) 1986: NOAA Data Report ERL AOML–10, 247 pp.

1.6 Tables

TABLE 1. CTD Stations in the Providence Channels

Cruise	Station	Latitude (°N)	Longitude (°W)
OC205–2	1	26.1637	77.6518
OC205–2	2	26.1750	77.6508
OC205–2	8	26.1225	77.7137
OC205–2	12	26.1695	77.7050
OC205–2	16	26.3263	77.8133
OC205–2	20	26.1173	77.7357
OC205–2	22	26.1570	77.7193
OC205–2	24	26.1882	77.7040
OC205–2	27	26.1892	77.7138
OC205–2	28	26.1767	77.7108
OC205–2	31	26.1835	77.6500
OC205–2	33	26.2210	77.6912
OC205–2	35	26.2245	77.7042
OC205–2	38	26.2183	77.6635
OC205–2	40	26.2657	77.7055
OC205–2	41	26.2277	77.6732
OC205–2	44	26.2682	78.2843
OC205–2	45	26.2595	77.7037
OC205–2	63	26.1265	77.7320
OC205–2	66	26.1540	77.7412
OC205–2	80	25.5632	76.8935
OC205–2	82	25.6065	76.9315
OC205–2	83	25.6558	76.9723
OC205–2	84C	25.6962	77.0112
OC205–2	85	25.7450	77.0607
OC205–2	86	25.7925	77.0952
OC205–2	87	25.8408	77.2668

TABLE 1. Continued

Cruise	Station	Latitude (°N)	Longitude (°W)
OC205–2	88	25.7997	77.3398
OC205–2	89	25.7613	77.4123
OC205–2	90	25.7358	77.4900
OC205–2	91	25.7027	77.5597
OC205–2	92	25.6657	77.6367
OC205–2	93	25.9417	77.8267
OC205–2	96	25.9327	77.8447
OC205–2	98	25.9747	78.0210
OC205–2	100	26.0612	78.0277
OC205–2	102	26.0703	78.0562
OC205–2	103	26.0663	78.0640
OC205–2	108	25.9838	78.1797
OC205–2	110	25.9483	78.2455
OC205–2	111	25.9237	78.1227
OC205–2	113	25.8803	78.1368
OC205–2	114	25.9062	78.1097
OC205–2	116	26.0333	77.8748
OC205–2	118	26.1240	77.7347
OC205–2	121	26.1547	77.7243
OC205–2	140	26.2002	77.7005
OC205–2	143	26.2297	77.7035
OC205–2	145	26.2163	77.6598
OC205–2	148	26.2595	77.6715
OC205–2	151	26.2303	77.6723
OC205–2	153	26.1948	77.7093
OC205–2	155	26.4572	78.6882
OC205–2	156	26.3858	78.7092
OC205–2	157B	26.3105	78.7273
OC205–2	158	26.2542	78.7515
OC205–2	159	26.1860	78.7728
OC205–2	160	26.1192	78.7938
OC205–2	161	26.0490	78.8170

TABLE 2. CTD Stations in the Florida Straits

Cruise	Station	Latitude (°N)	Longitude (°W)
AT109	240	26.033	79.230
AT109	241	26.041	79.344
AT109	242	26.058	79.378
AT109	243	26.033	79.480
AT109	244	26.030	79.562
AT109	245	26.042	79.670
AT109	246	26.033	79.767
AT109	247	26.033	79.850
AT109	248	26.092	79.933
AT109	249	26.092	80.020
AT109	250	26.092	80.067

TABLE 3. CTD Stations in the Sargasso Sea

Cruise	Station	Latitude (°N)	Longitude (°W)
AT109	215	24.516	64.932
AT109	223	24.529	70.023
AT109	232	24.496	74.412
AT109	233	24.513	74.723
AT109	234	24.510	75.011
AT109	235	24.502	75.285
AT109	236	24.492	75.420
AT109	237	24.471	75.440
AT109	238	24.501	75.524
AT109	239	24.510	75.538
EN129	30	23.985	64.499
EN129	34	26.000	64.490
EN129	37	27.498	64.502
EN129	38	28.000	64.504

1.7 Figure Captions

Figure 1. The geographic setting of the Northeast and Northwest Providence Channels.

Figure 2. Bathymetry of the Northeast and Northwest Providence Channels in meters (after NOAA SE United States regional map). Solid circles indicate the locations of CTD stations occupied during *RV Oceanus* cruise 205–2.

Figure 3. Vertical profiles of salinity calculated after advancing measured conductivity in time relative to measured temperature. Notice the changes in the magnitude and sense of spikes with different advances. The minimal salinity spikes associated with the -0.4 second advance suggests that this value best compensates for the inherent mis-match in the response time of the CTD's conductivity and temperature sensors.

Figure 4. θ–S relationships for the Florida Straits (dashes) and the Sargasso Sea (lines).

Figure 5. θ–S relationships for the Northeast and Northwest Providence Channels.

Figure 6. θ–S relationships for the Florida Straits (dashes), the Sargasso Sea (lines) and the Providence Channels (dots). If Providence Channel waters were a mixture of Sargasso Sea and Florida Straits waters, the channel waters would have a θ–S relationship that falls between those of the Florida Straits and the Sargasso Sea. However, Providence Channel waters have the same θ–S relationship as Sargasso Sea waters and, for $\theta \leq 15.5°C$, a distinctly different θ–S than the Florida Straits. This demonstrates that these waters have a Sargasso Sea origin.

Figure 7. Distribution of a) temperature b) salinity, c) potential density and d) geostrophic velocity (assumed to be zero at greatest depth common to adjacent CTD profiles, positive value out of page) for section 1 across Northeast Providence Channel. Circles at top of section indicate locations of CTD stations.

Figure 8. Same as Figure 7 except for section 2 across eastern end of Northwest Providence Channel.

Figure 9. Same as Figure 7 except for section 3 across western end of Northwest Providence Channel.

1.8 Figures

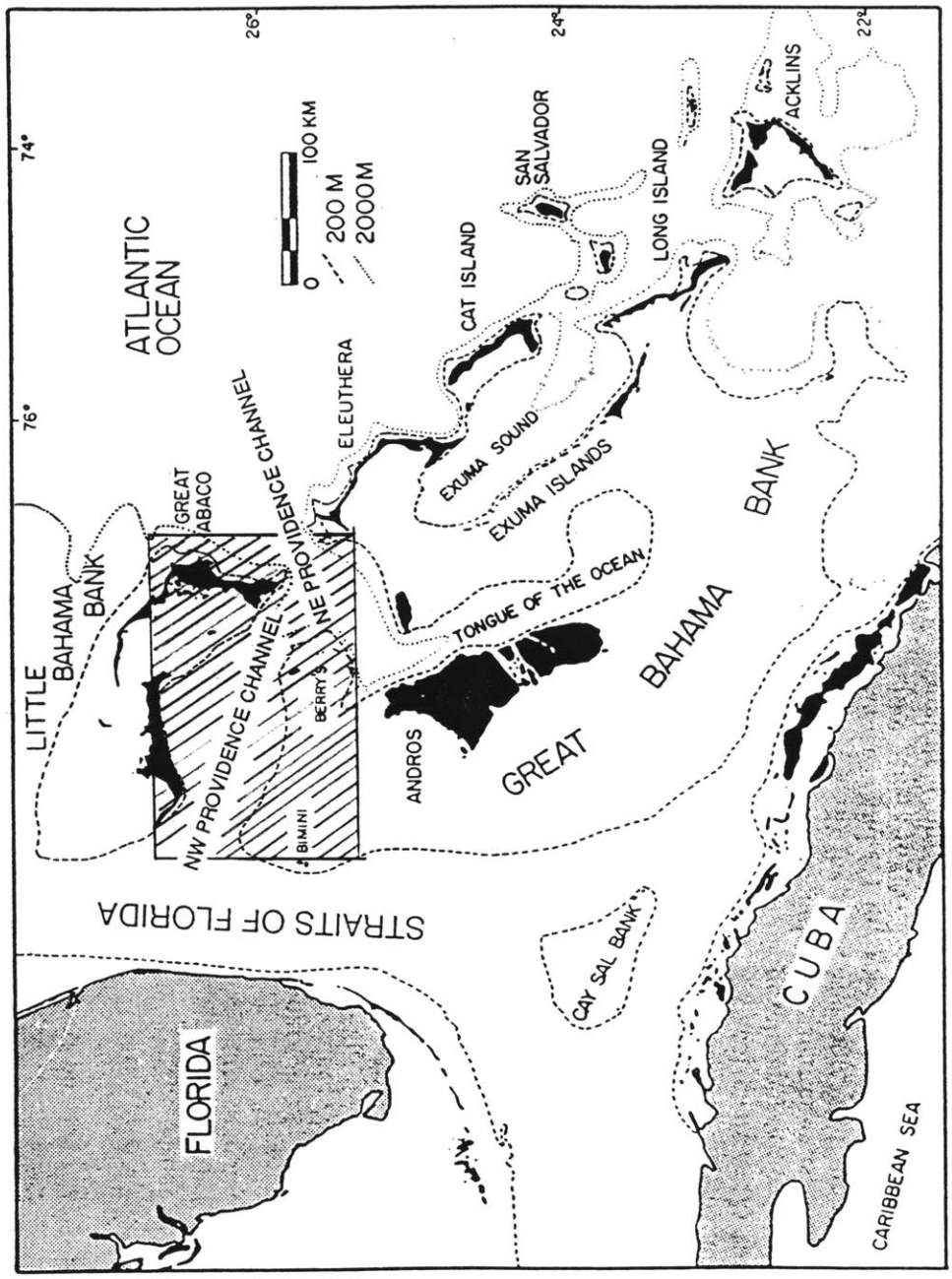
ATLANTIC OCEAN
LITTLE BAHAMA BANK
GREAT ABACO
NW PROVIDENCE CHANNEL
NE PROVIDENCE CHANNEL
BERRY IS.
BIMINI
ELEUTHERA
CAT ISLAND
SAN SALVADOR
LONG ISLAND
ACKLINS
EXUMA SOUND
EXUMA ISLANDS
TONGUE OF THE OCEAN
ANDROS
GREAT BAHAMA BANK
STRAITS OF FLORIDA
FLORIDA
CAY SAL BANK
CUBA
CARIBBEAN SEA
0 100 KM
200 M
2000 M
74°
76°
26°
24°
22°

Figure 1.

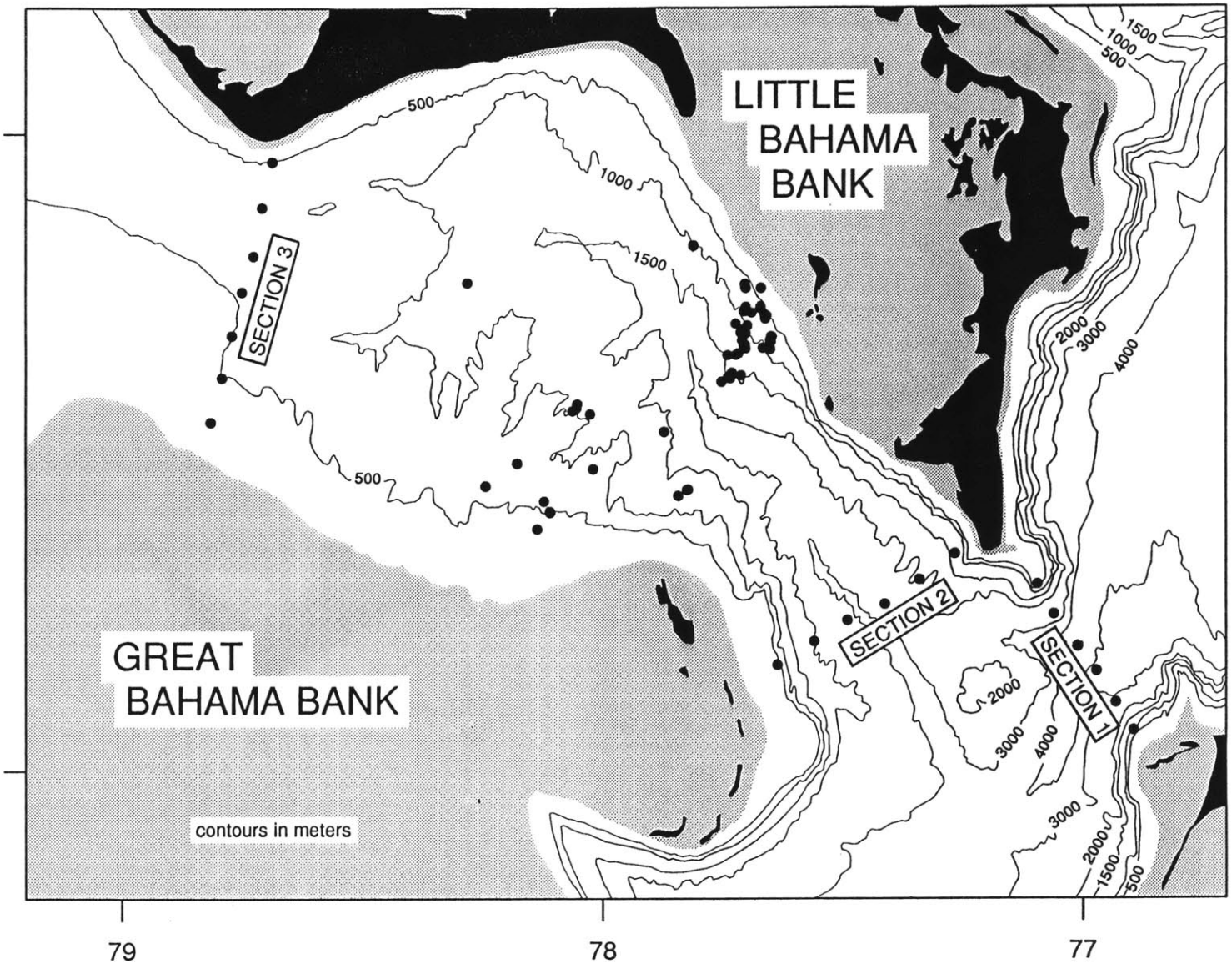
LITTLE
BAHAMA
BANK
GREAT
BAHAMA BANK
SECTION 1
SECTION 2
SECTION 3
contours in meters
500
1000
1500
2000
3000
4000
26.5
25.5
79
78
77

Figure 2.

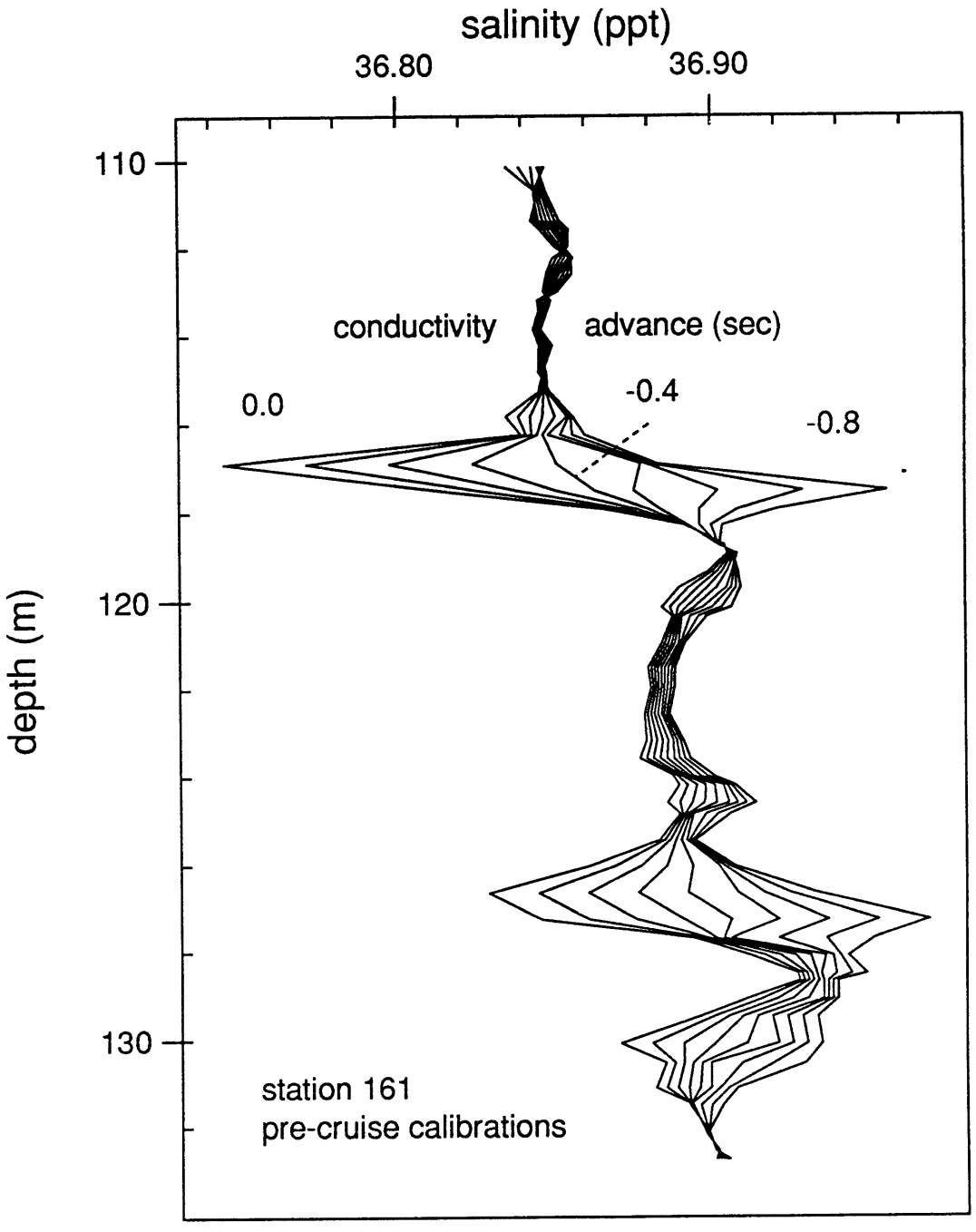
salinity (ppt)
36.80
36.90
110
120
130
depth (m)
conductivity
advance (sec)
0.0
-0.4
-0.8
station 161
pre-cruise calibrations

Figure 3.

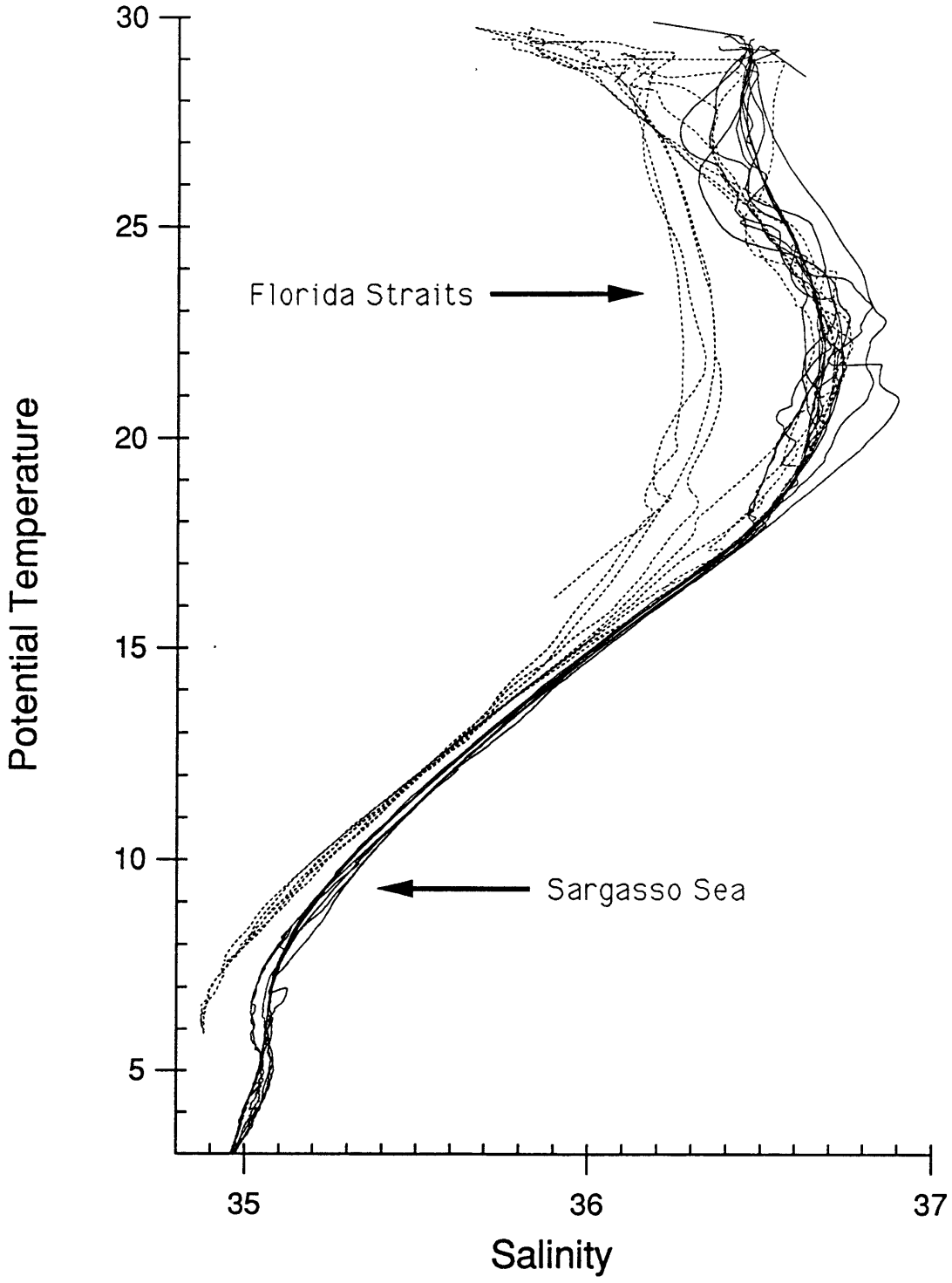
30
25
20
15
10
5
Potential Temperature
Florida Straits
Sargasso Sea
35
36
37
Salinity

Figure 4.

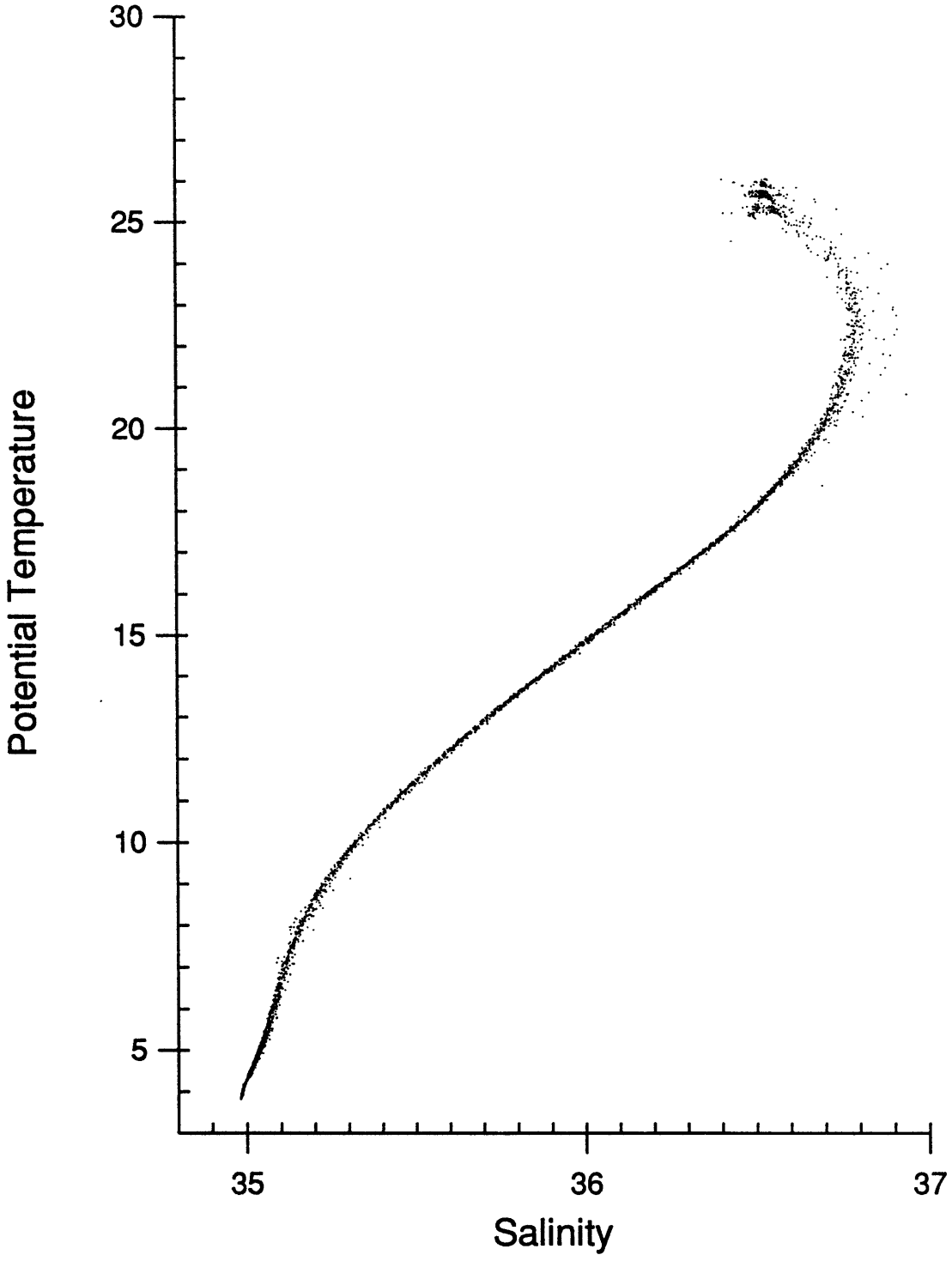

Figure 5.

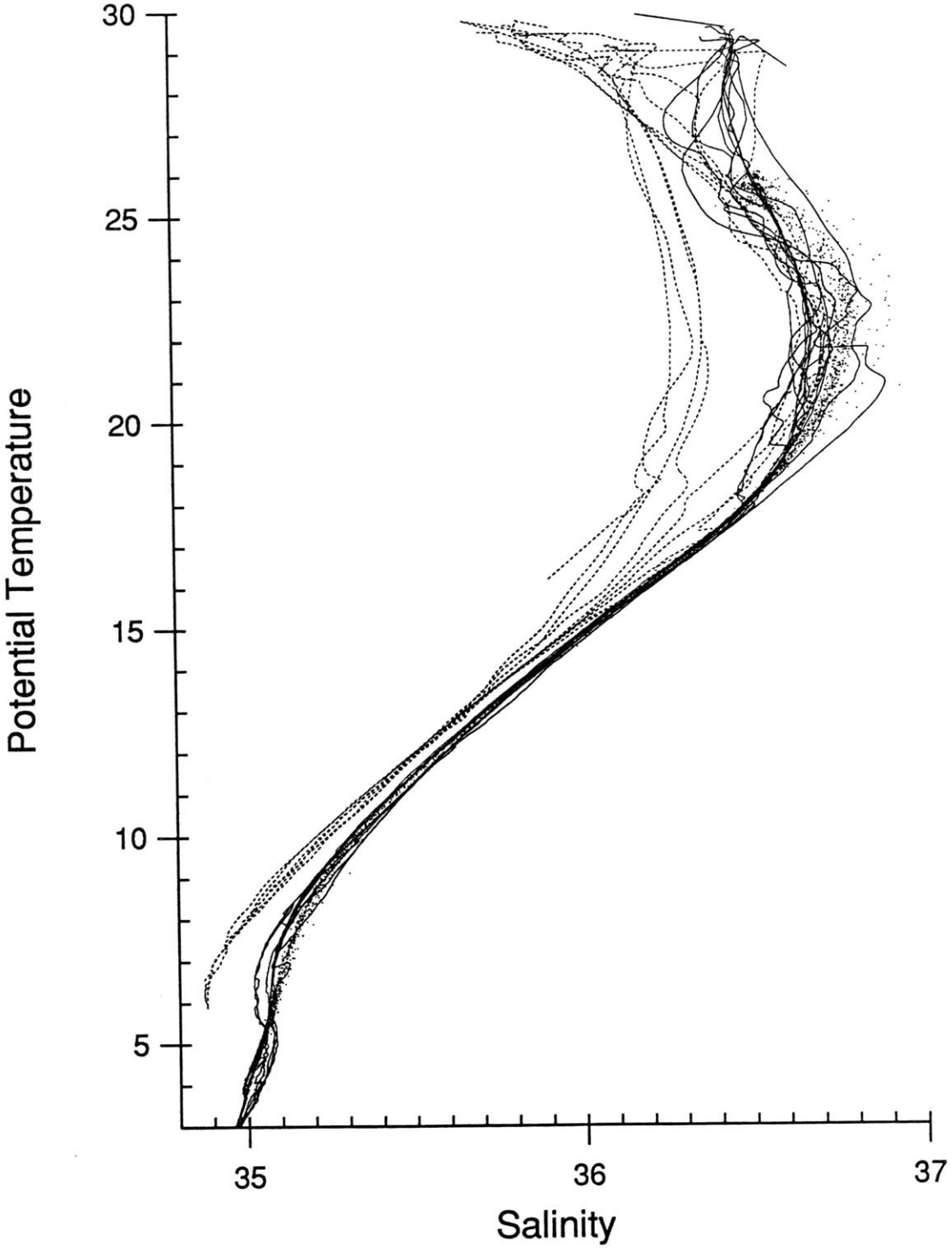

Figure 6.

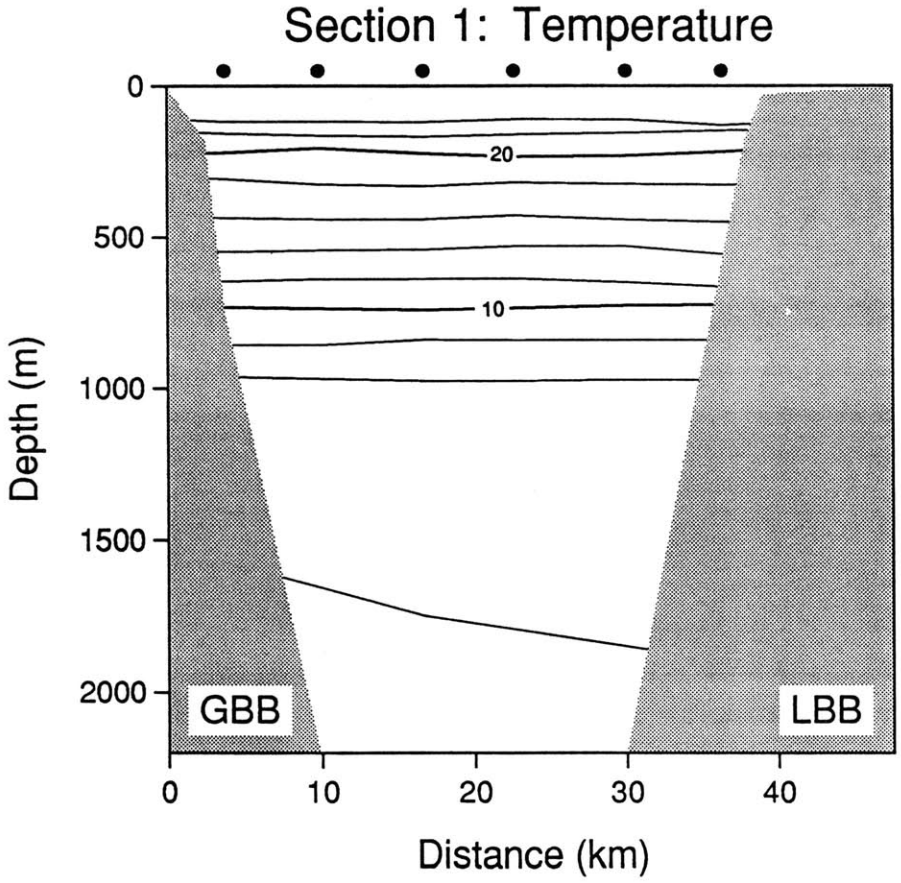
Section 1: Temperature
0
500
1000
1500
2000
Depth (m)
20
10
GBB
LBB
0
10
20
30
40
Distance (km)

Figure 7a.

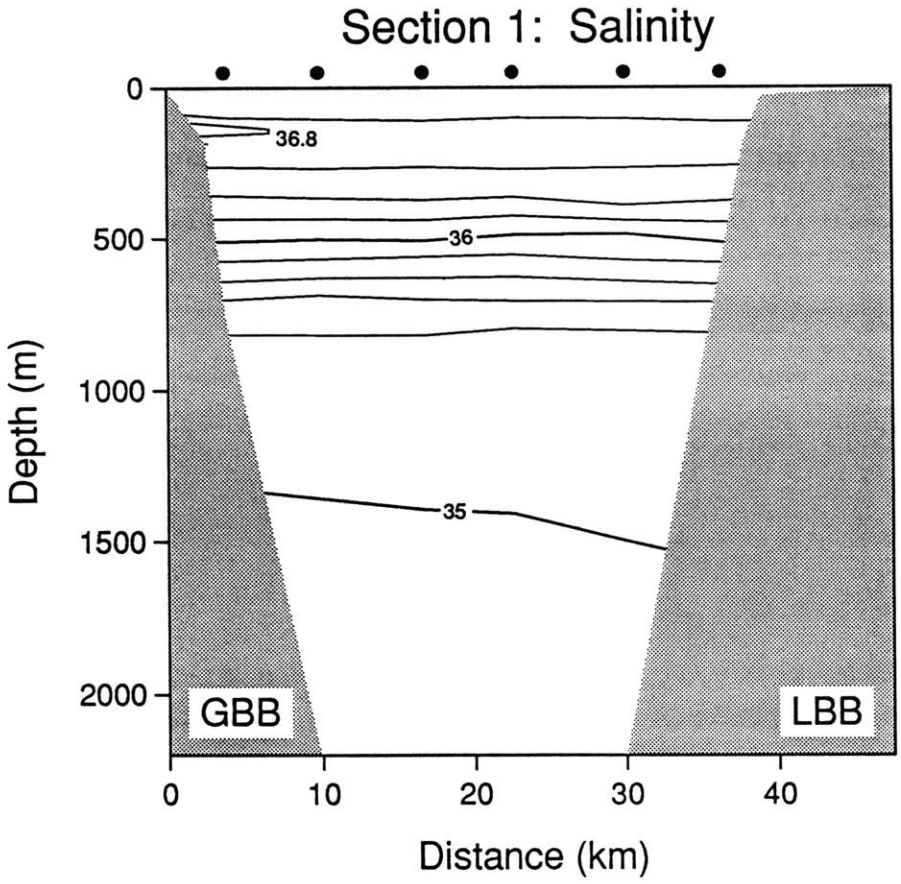
Section 1: Salinity
0
500
1000
1500
2000
Depth (m)
36.8
36
35
GBB
LBB
0
10
20
30
40
Distance (km)

Figure 7b.

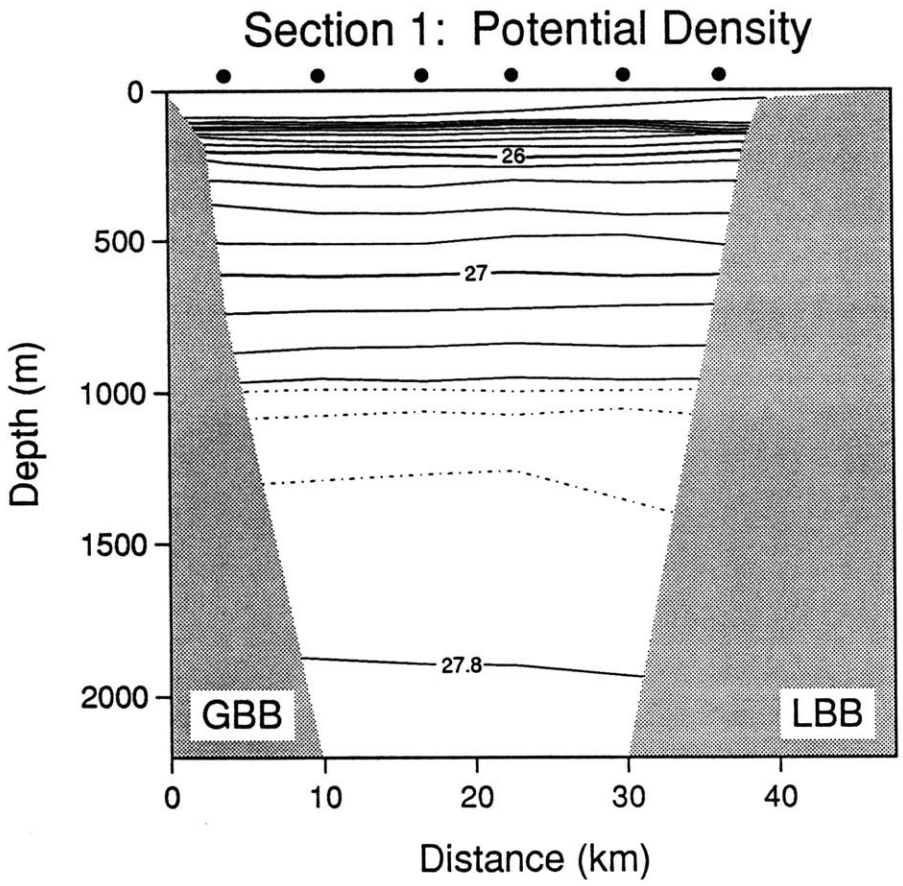
Section 1: Potential Density
Depth (m)
0
500
1000
1500
2000
26
27
27.8
GBB
LBB
0
10
20
30
40
Distance (km)

Figure 7c.

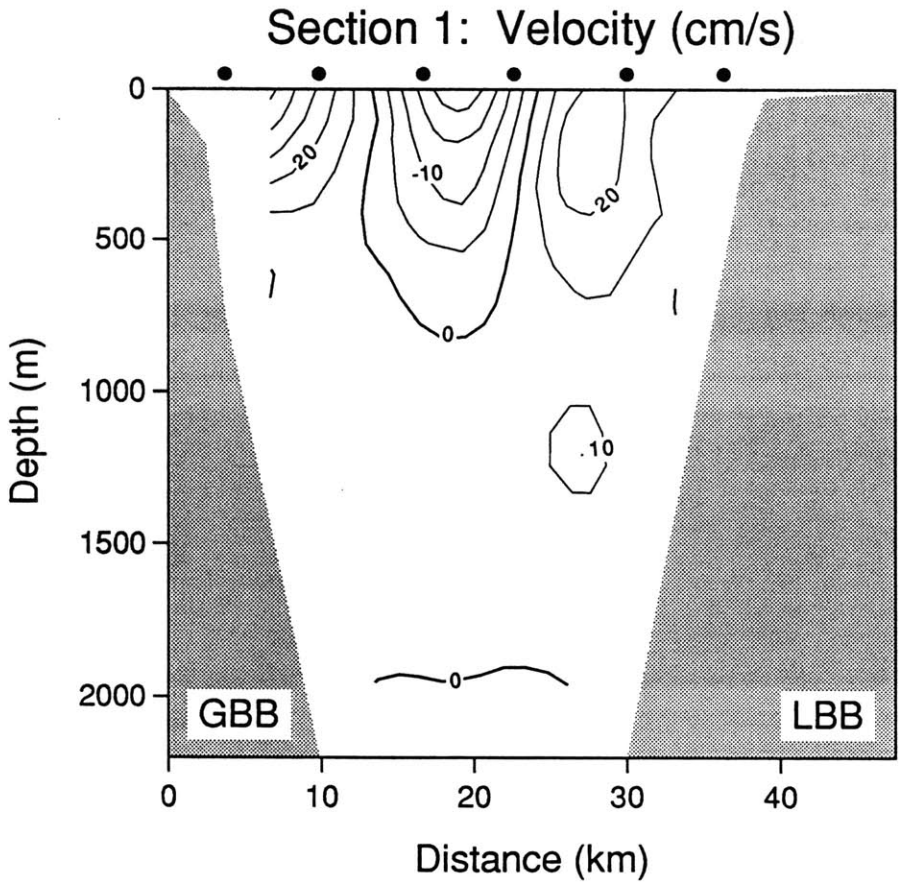
Section 1: Velocity (cm/s)
Depth (m)
0
500
1000
1500
2000
-20
-10
20
0
10
0
GBB
LBB
0
10
20
30
40
Distance (km)

Figure 7d.

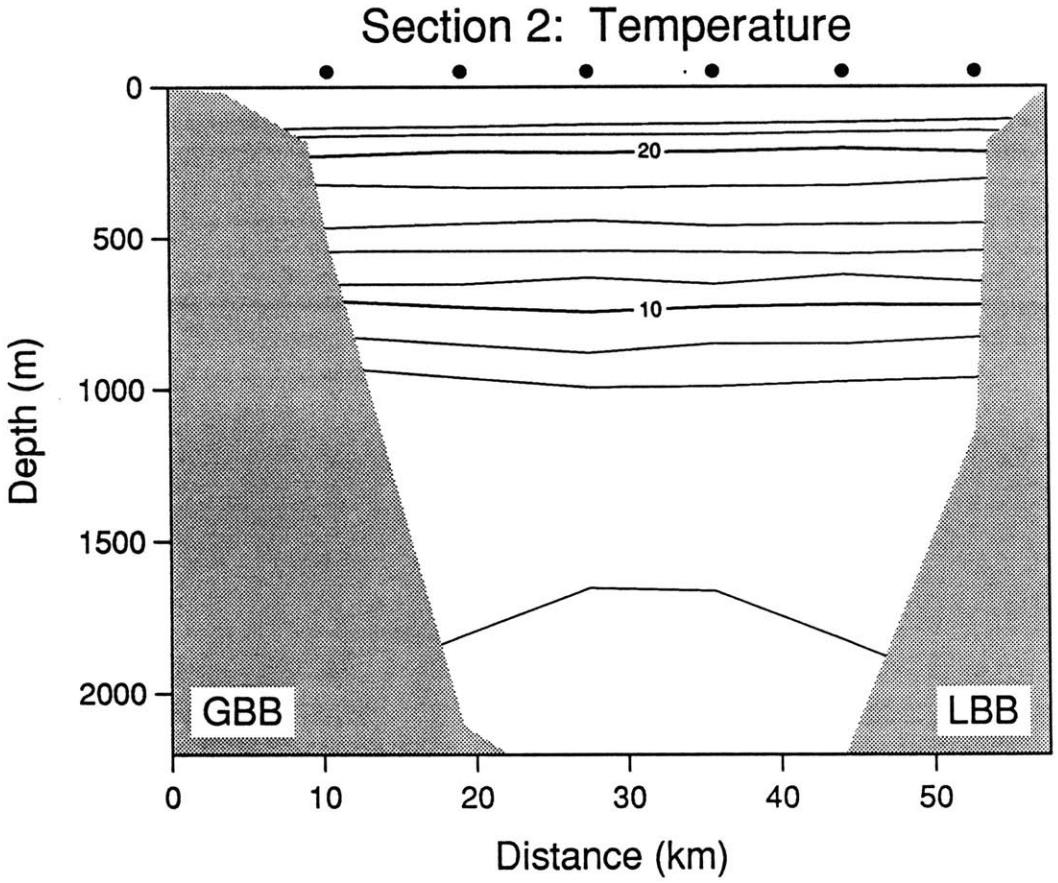
Section 2: Temperature
0
500
1000
1500
2000
Depth (m)
20
10
GBB
LBB
0
10
20
30
40
50
Distance (km)

Figure 8a.

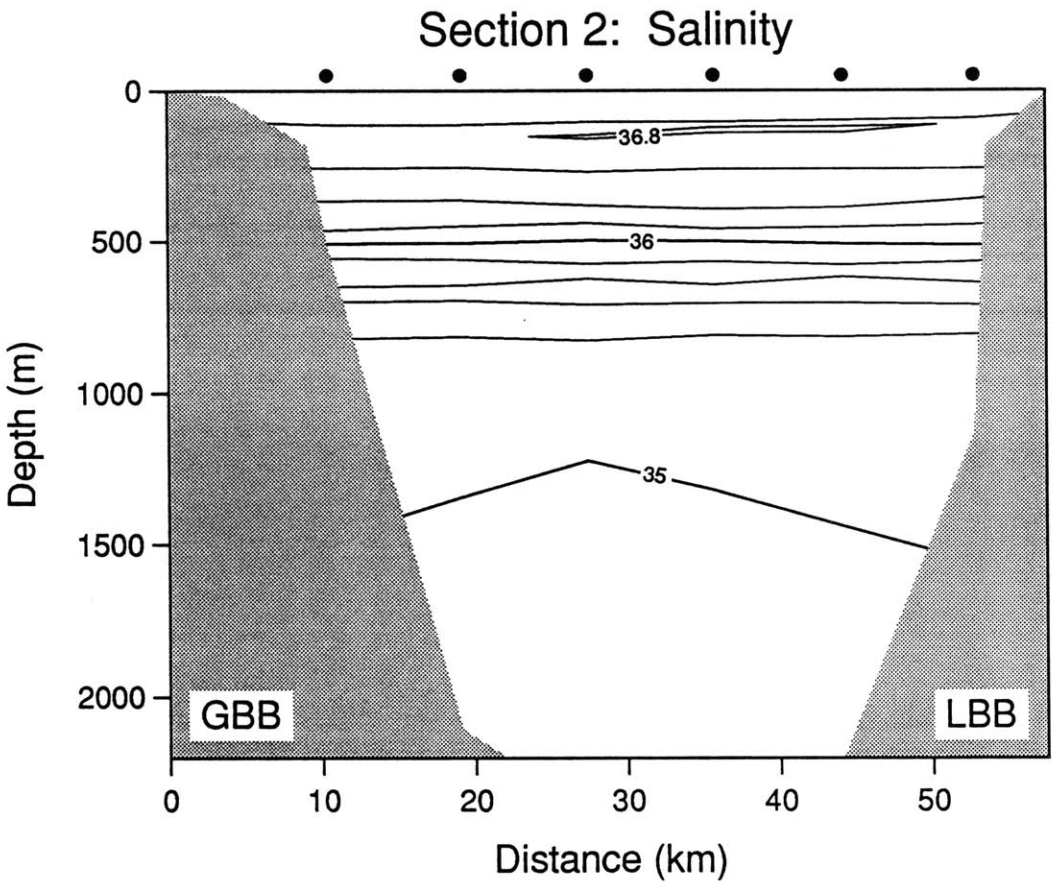
Section 2: Salinity
0
500
1000
1500
2000
Depth (m)
36.8
36
35
GBB
LBB
0
10
20
30
40
50
Distance (km)

Figure 8b.

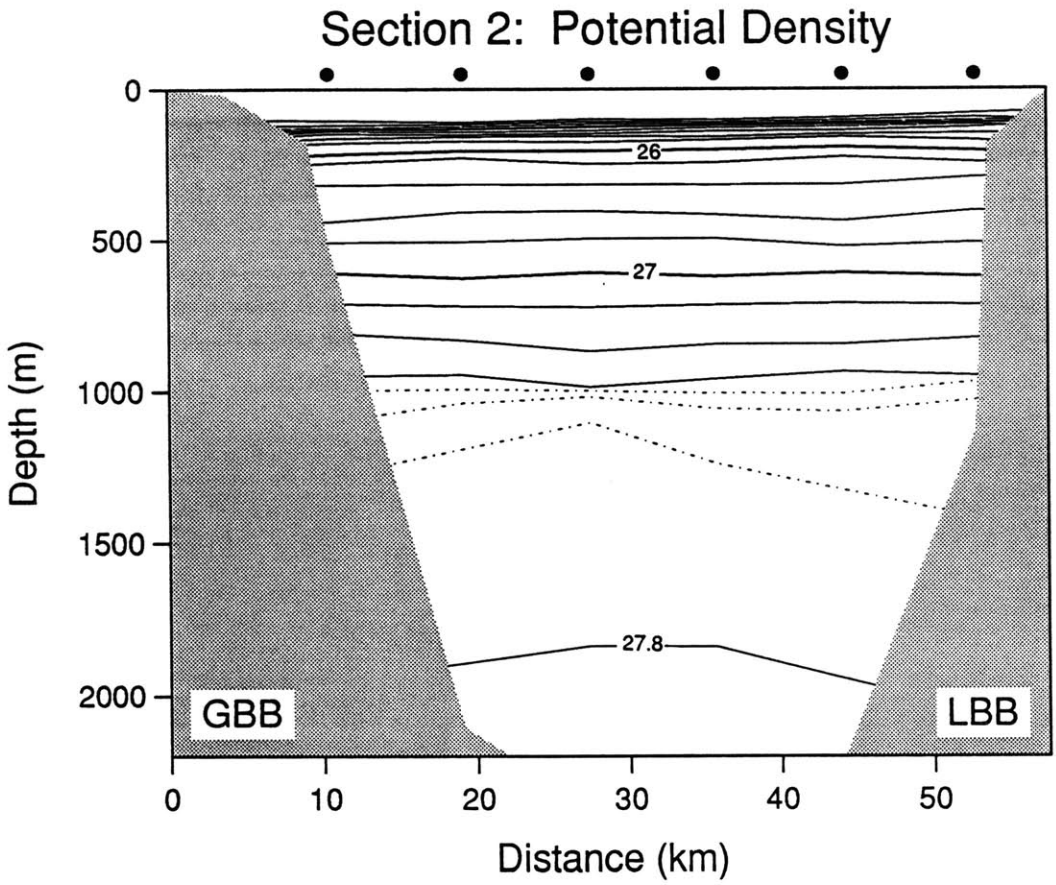
Section 2: Potential Density
Depth (m)
0
500
1000
1500
2000
26
27
27.8
GBB
LBB
0
10
20
30
40
50
Distance (km)

Figure 8c.

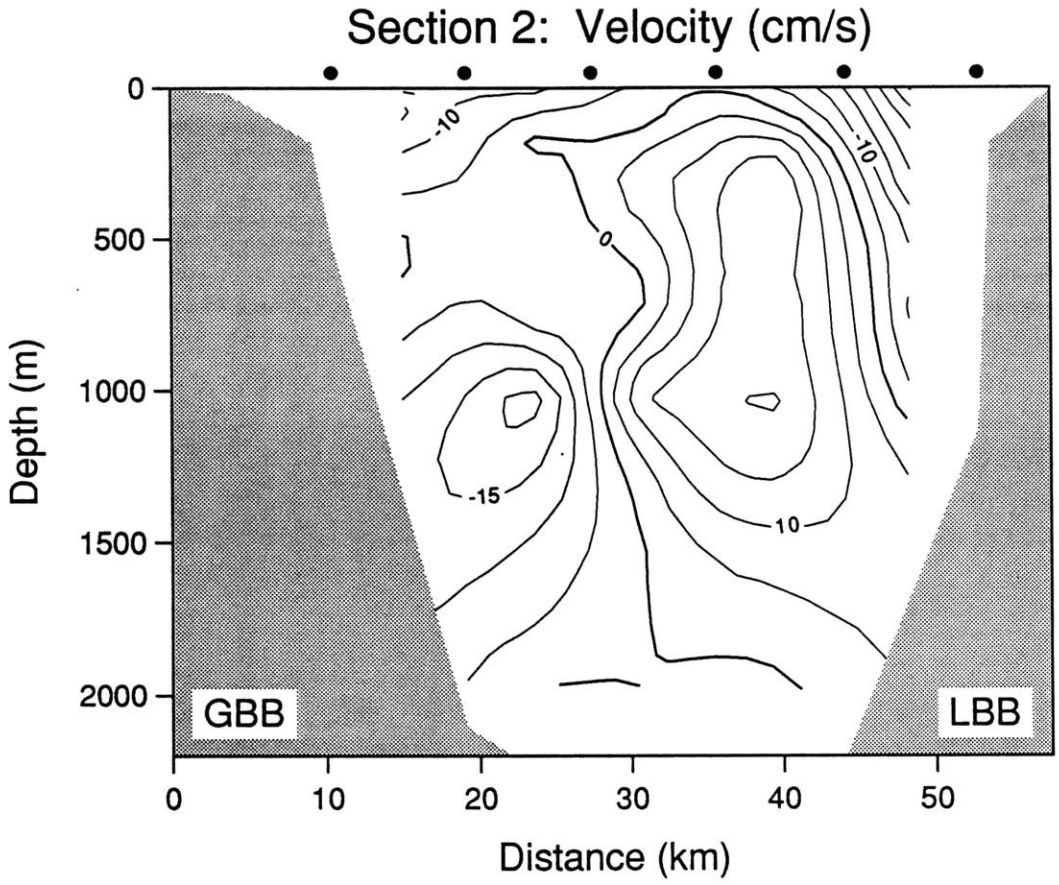
Section 2: Velocity (cm/s)
Depth (m)
0
500
1000
1500
2000
-10
-10
0
-15
10
GBB
LBB
0
10
20
30
40
50
Distance (km)

Figure 8d.

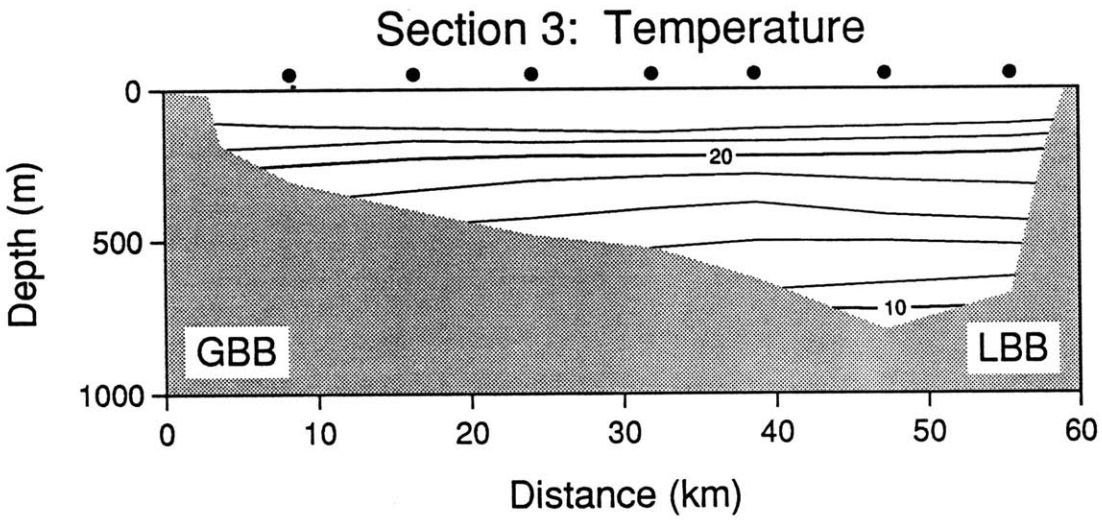
Section 3: Temperature
Depth (m)
0
500
1000
20
10
GBB
LBB
0
10
20
30
40
50
60
Distance (km)

Figure 9a.

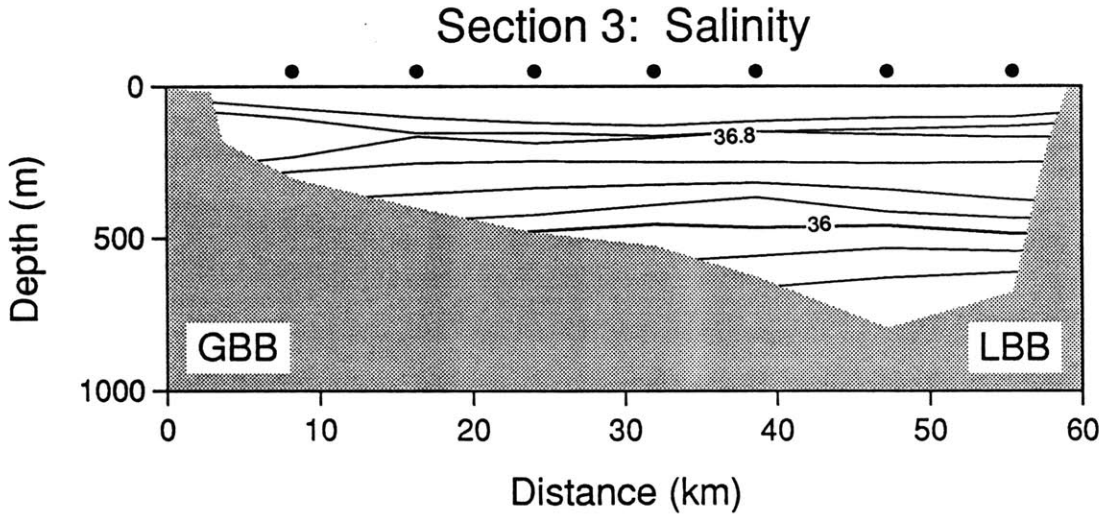
Section 3: Salinity
Depth (m)
0
500
1000
36.8
36
GBB
LBB
0
10
20
30
40
50
60
Distance (km)

Figure 9b.

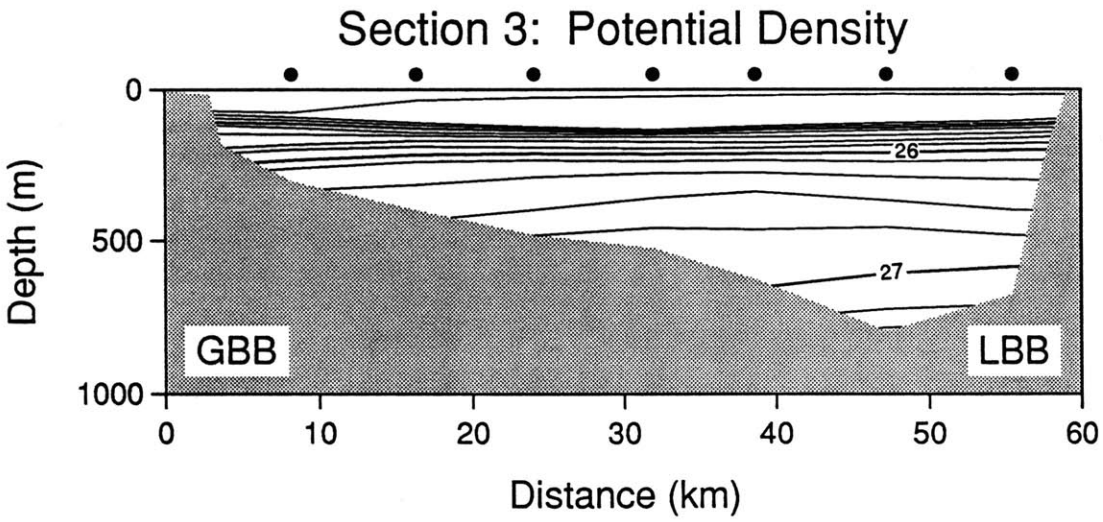
Section 3: Potential Density
Depth (m)
0
500
1000
26
27
GBB
LBB
0
10
20
30
40
50
60
Distance (km)

Figure 9c.

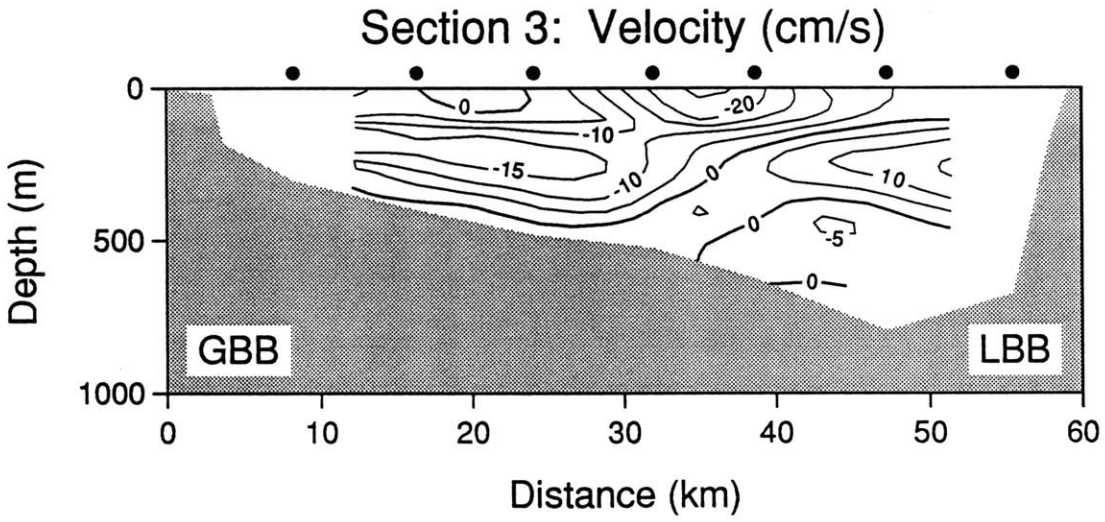
Section 3: Velocity (cm/s)
Depth (m)
0
500
1000
0
10
20
30
40
50
60
Distance (km)
GBB
LBB
0
-10
-20
-15
-10
0
10
0
-5
0

Figure 9d.

Chapter 2

Structure of the glacial thermocline at Little Bahama Bank

Structure of the glacial thermocline at Little Bahama Bank

Niall C. Slowey* & William B. Curry†

* WHOI/MIT Joint Program in Oceanography, Woods Hole, Massachusetts 02543, USA
† Department of Geology and Geophysics, Woods Hole Oceanographic Institution, Woods Hole, Massachusetts 02543, USA

Within the thermocline of the western North Atlantic, bathymetric gradients of hydrographic properties are controlled by the lateral movement of water along isopycnal surfaces[1-4]. This movement is driven by air–sea interaction processes: Ekman pumping and surface heat (buoyancy) flux. By affecting the intensity of these processes, glacial–interglacial climatic change should also affect the bathymetric gradients of properties within the thermocline. Benthic foraminifera live on carbonate bank margins that intersect the thermocline. These foraminifera record the hydrographic gradients in their isotopic shell chemistry, providing the means to reconstruct changes in thermocline structure and circulation. We have measured the $\delta^{18}O$ compositions of a near-surface planktonic foraminifer, *Globigerinoides ruber*, and a shallow-water benthic foraminifer, *Cibicidoides floridanus*, in a core recovered from Little Bahama Bank. *Cibicidoides floridanus* exhibits a glacial–interglacial range in $\delta^{18}O$ that is 0.5‰ less than *G. ruber*'s, because individuals of this species lived and calcified ~110 m shallower on the thermocline ~18,000 yr ago. After glacio-eustatic changes in thermocline position are accommodated, we estimate that temperature at 540 m palaeodepth cooled by ~2 °C. *Globigerionoides ruber* $\delta^{18}O$ values suggest that surface water temperature at this location also cooled by ~2 °C. This uniform cooling of the upper 600 m of the water column is consistent with the observation that surface water where isopycnals outcrop was ~2 °C cooler during the glacial maximum[5-8].

During January 1982, the RV *Cape Hatteras* recovered piston core CH0182-36 from the southwest margin of Little Bahama Bank, Bahamas. Seismic profiles of the site (26.1797° N, 77.6460° W, 651 m) and the down-core carbonate stratigraphy indicate undisturbed hemi-pelagic deposition in the vicinity of CH0182-36 (refs 9, 10). Sediments are foraminifera-pteropod ooze which appear to be partly lithified at ~40–45 cm depth[9]. Over the depth range of 0–90 cm, four bulk sediment radiocarbon ages[9,10] (Table 1) and $\delta^{18}O$ provide chronologic control. We sampled the core at 2-cm intervals for isotopic analyses and present a record with average spacing of 1,000 yr. Oxygen-isotope analyses of *C. floridanus*[11] (equivalent to *C. pachyderma* (Rzehak)[12], >250 μm) and *G. ruber* (white variety, 212–250 μm) were made by using standard methods[13], and our results are presented in δ notation with respect to PDB (Table 1).

The $\delta^{18}O$ records (Fig. 1) extend from the Late Holocene back through the last glacial period (~18 kyr). Ages were assigned to samples by correlating the $\delta^{18}O$ records of *G. ruber* in CH0182-36 and *Uvigerina* in core V19-30[14] (age model of Shackleton and Pisias[15]). Ages obtained by correlation agree reasonably well with the radiocarbon ages (~2 kyr mean deviation). Inaccuracies in the V19-30 age model and difficulties in using bulk sediment radiocarbon dates for high resolution stratigraphy[16-18] may cause some differences between the age scales. For this study it is much more important to have closely correlated CH0182-36 with V19-30 than to determine the absolute age of the sediment, because we use V19-30 as both a record of eustatic sea-level and a monitor of the effect of continental ice volume on the $\delta^{18}O$ of sea water.

There are two notable differences between the planktonic and benthic $\delta^{18}O$ records. (1) As is typically observed in deep-sea sediment cores, $\delta^{18}O$ values for the benthic *C. floridanus* are always greater than corresponding values for planktonic *G. ruber* because the benthic foraminifer lives in sea water that is cooler

Table 1 Visual correlation chronology, ^{14}C ages and oxygen-isotopic data for CH0182-36

Depth (cm)	Age* (kyr)	$\delta^{18}O_{PDB}$ (*G. ruber*)	$\delta^{18}O_{PDB}$ (*C. floridanus*)	Depth (cm)	Age* (kyr)	$\delta^{18}O_{PDB}$ (*G. ruber*)	$\delta^{18}O_{PDB}$ (*C. floridanus*)
0	0.0†			47	12.8	−0.38	2.41
1	0.4	−1.74	—	49	13 3	−0 40	1 47
	1.27 ± 0.06‡			50	16.96 ± 0.29‡		
3	1.1	−1.62	1.04	51	13.8	−0.17	2.37
5	1.8	−2.01	1.07	53	14 3	−0.22	2.06
7	2.5	−1.75	1.08	55	14.8†	−0.74	1.72
9	3.2	−1.86	1.04	57	15.1	−0.27	2.06
11	3.9	−1.90	1.05	59	15.5	0.02	2.15
13	4.6	−1.52	1.06	61	15.8	−0 10	2.37
15	5.3	−1.92	0.98	63	16.1†	0.17	2.01
17	6.0†	−1.64	1.08	65	17 4	−0.12	2.36
18	4.08 ± 0 10‡			67	18.7	−0.23	2.12
19	6.4	−1.86	0.90	69	20.0	−0.44	2.15
21	6.8	−1.85	1.29	70	20.6	−0.09	2.28
23	7.2	−1.90	1.20	73	22.6	−0.29	1.95
25	7.6	−1.87	0.95	74	23.2	−0.24	2.19
27	8.0	−1.87	1.27	76	24.5	−0.21	2.25
29	8.5	−1.75	1.42	77	25.1	−0.27	2.06
31	8.9	−1.69	1.21	78	26.3†		
32	7.27 ± 0.11‡			79	26.4	−0.73	1.84
33	9.3	−1.31	1.21	81	27.7	−1.00	1.97
35	9.7†	−2.00	1.16	83	29.0	−0.55	2.10
37	10.2	−1.44	1.28	85	30.3	−0.79	1.87
39	10.8	−1.58	1.30	87	31.5	−0.67	—
41	11.3	−1.47	1.56	89	32.8	−1.34	—
43	11.8	−1.00	1.89	91	34.1	−0.82	—
45	12.3	−0.82	2.35	93	35 4	−1.03	—
46	12.6†						

* Unless otherwise noted, obtained by linear interpolation between tie points from visual correlation between $\delta^{18}O$ of *G. ruber* and V19-30 *Uvigerina*[14,15].
† Visual correlation tie point.
‡ From bulk sediment ^{14}C dating[9,10].

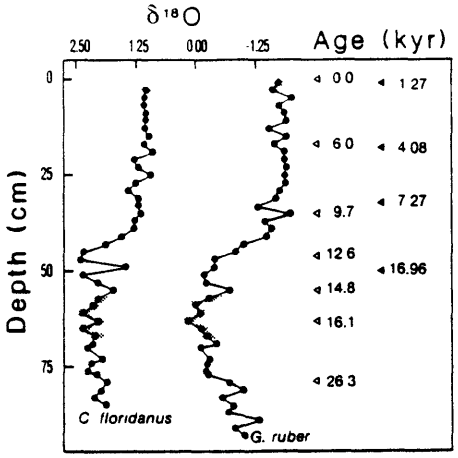

Fig. 1 Oxygen-isotope data for *C. floridanus* and *G. ruber* from core CH0182-36. Correlation points of the $\delta^{18}O$ records of *G. ruber* in CH0182-36 and *Uvigerina* in V19-30 (refs 14, 15) (open triangles), bulk sediment ^{14}C ages[9,10] (solid triangles), and both recent Holocene (0–4 cm) and glacial maximum (56–68 cm) $\delta^{18}O$ data (shaded) are indicated.

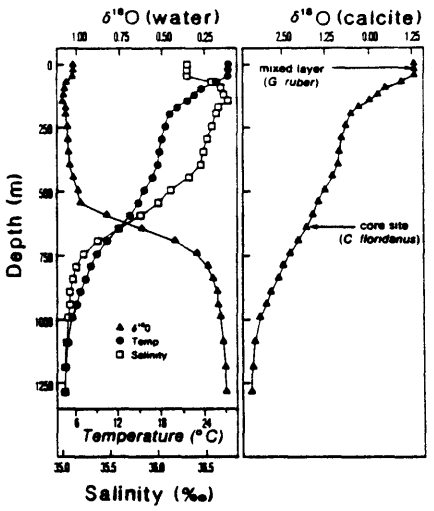

Fig. 2 *a*, Profiles of temperature, salinity and $\delta^{18}O$ for the present-day water column near the site of CH0182-36 (25.7833° N, 77.0000° W, RV Researcher cruise ANT80). Values of $\delta^{18}O$ were calculated from the salinity data by using salinity-$\delta^{18}O$ relations (R. G. Fairbanks, personal communication) for Sargasso Sea Water and North Atlantic Deep Water. *b*, Profile of the $\delta^{18}O$ of equilibrium calcite and the depths at which *G. ruber* and *C. floridanus* live today.

(10–15 °C) than the surface water (~25 °C). (2) The magnitude of the glacial–interglacial change of *C. floridanus* (1.1‰) is significantly less than that of *G. ruber* (1.6‰). The differences between the records result from the relative positions of the planktonic and benthic foraminifera within the thermocline, and the vertical migration of the thermocline along the bank margin (where *C. floridanus* lives) that accompanies glacio-eustatic sea level changes.

The $\delta^{18}O$ of calcite deposited in equilibrium with the present sea water at Little Bahama Bank increases with depth because of a large decrease in temperature within the thermocline. Figure 2*a* shows the measured temperature and salinity (25.7833° N, 77.0000° W, RV *Researcher* cruise ANT80), and estimated oxygen isotopic composition of sea water ($\delta^{18}O_w$) as a function of depth as it is today near the site of CH0182-36. Because the principal source of this water is the Gulf Stream recirculation system[19], $\delta^{18}O_w$ was calculated from $\delta^{18}O_w$-salinity relations for Sargasso Sea Water and North Atlantic Deep Water (R. G. Fairbanks personal communication). In the surface waters, salinity decreases from lower to higher latitudes, and higher salinities correlate with enriched $\delta^{18}O_w$ values because evaporation increases salinity while fractionating $H_2^{16}O$ from $H_2^{18}O$[20,21]. Both salinity and $\delta^{18}O_w$ values decrease with depth at this location because deeper thermocline waters are supplied along isopycnals from the ocean surface at higher latitudes[1–4]. Despite this decrease in $\delta^{18}O_w$, the $\delta^{18}O$ of calcite precipitated in equilibrium with the sea water shows a consistent increase with depth in the water column (Fig. 2*b*) because of the overwhelming effect of the large temperature decrease[22,23].

The $\delta^{18}O$ difference between *G. ruber* and *C. floridanus* reflects this bathymetric gradient. *Globigerinoides ruber* live and deposit their tests within the mixed layer[24–30], so their equilibrium $\delta^{18}O$ composition should equal −1.3‰. The mean value observed for the interval 0.4–1.1 kyr is −1.7‰. The observed difference between our recent Holocene average and the calculated equilibrium $\delta^{18}O$ value is −0.4‰, which agrees with previously reported disequilibria of −0.25–−0.5‰[28–30]. Much of this difference has been attributed to the effects of symbiotic algae[29]. Sediment-trap studies in the Sargasso Sea indicate that the flux of *G. ruber* to the sea floor is relatively constant thoughout the year[31,32]. We assume that this same seasonal pattern of *G. ruber* production existed during the glacial maximum, so that the $\delta^{18}O$ of *G. ruber* reflects the average annual surface water palaeotemperature. For individual *Cibicidoides* species, the offset from equilibrium has been reported to range between −0.64 and −1.0‰[33–37]. Our most recent Holocene value is 1.0‰ and expected equilibrium at 651-m water depth is 1.8‰, indicating that vital effects of *C. floridanus* fall within the range of previously investigated *Cibicidoides* species. We assume that the vital effects remain constant through time so that foraminiferal and equilibrium $\delta^{18}O$ values have the same spatial and temporal gradients.

Figure 3 shows the average measured interglacial and glacial maximum $\delta^{18}O$ values of *G. ruber* and *C. floridanus* along with the glacial foraminifera $\delta^{18}O$ values that would be expected if the thermocline maintained its present depth structure while the sea level changed. Also shown are the $\delta^{18}O$ values that would exist if sea-water temperatures at this location decreased by increments of 1 °C. Palaeodepths and past sea-level are based on the history of eustatic sea-level inferred from the $\delta^{18}O$ record of benthic foraminifera in V19-30[14,15] (corrected for effects of deep-water temperature change[38]). Eustatic sea-level changes were calculated by assuming that a 0.1‰ increase in $\delta^{18}O$ corresponds to a 10 m fall in sea-level[38,39]. The expected $\delta^{18}O$ values were generated by the palaeotemperature equation[22,23] and the data in Fig. 2 (after accounting for ice volume effects as indicated by the V19-30 record).

For the surface-dwelling planktonic foraminifer, *G. ruber*, the expected $\delta^{18}O$ composition follows a simple response to sea-level change because its position within the water column does not change with respect to sea-level. The benthic foraminifer, *C. floridanus*, has a more complicated response to sea-level change because its $\delta^{18}O$ composition is affected not only by enrichment and depletion that correspond to ice volume growth and decay, but also by changes in its position within the thermocline as sea level changes. Thus whereas the isotopic composition of *G. ruber* is affected mostly by changes in ice volume and sea surface temperature, *C. floridanus* is affected by ice volume, migration of the thermocline and changes in the temperature structure within the thermocline.

The average glacial $\delta^{18}O$ compositions for both *G. ruber* and *C. floridanus* show that near-surface and mid-thermocline water

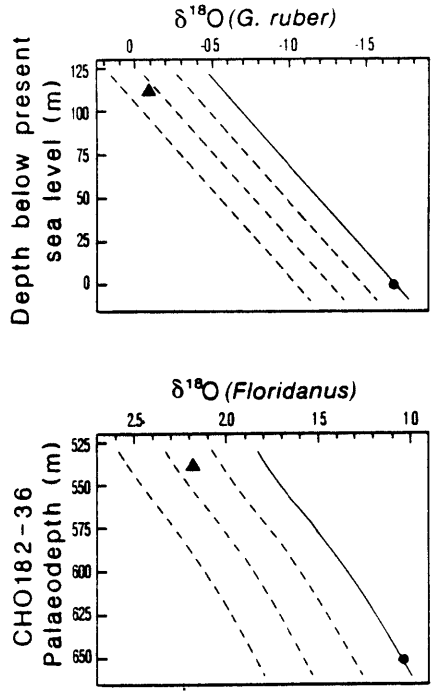

Fig. 3 The average measured $\delta^{18}O$ of recent Holocene foraminifera are represented by circles. If water temperatures near the surface and within the thermocline have remained the same from the last glacial maximum through today, then the solid lines trace the $\delta^{18}O$ of foraminifera that would be expected as ice volume and sea level changed; dashed lines trace the $\delta^{18}O$ of foraminifera if water temperatures were decreased by 1 °C increments. For a given *y*-axis value, heavier $\delta^{18}O$ values indicate cooler water temperatures and the dashed lines provide a scale to calibrate the temperature of water in which foraminifera lived. The averaged measured $\delta^{18}O$ of glacial foraminifera (triangles) are heavier than expected, indicating that glacial water temperatures were cooler than today at (*a*) the surface and (*b*) 540 m palaeodepth.

temperatures were colder by about 2.3 and 1.7 °C, respectively, during the last glacial maximum than today. If only differences in ice volume and eustatic sea level change affected the $\delta^{18}O$ of *C. floridanus*, then its glacial $\delta^{18}O$ value should be 1.8‰ during the lowest sea level (sea-level change −110 m, CH0182-36 palaeodepth ~540 m) (Fig. 3*b*). The predicted net difference from today of 0.7‰ reflects the combined effects of a 1.1‰ change due to greater ice volume and a −0.4‰ change due to calcification shallower in the thermocline at warmer temperatures (see Fig. 2*b*). This predicted glacial $\delta^{18}O$ value is 0.4‰ less than the measured glacial value, indicating that the thermocline at that paleodepth (540 m) was about 1.7 °C cooler than at 540 m depth in the modern ocean. Similarly, if glacial near-surface waters had the same temperature as today, then the predicted $\delta^{18}O$ value of *G. ruber* would be −0.6‰ during the glacial maximum, 1.1‰ greater than today due to greater ice volume (Fig. 3*a*). This value is 0.5‰ less than our measured glacial value for *G. ruber*, indicating that surface water temperature cooled by 2.3 °C. Precisely how variations in evaporation and precipitation affected the $\delta^{18}O$ of the water during glacial times is not known. Our glacial-interglacial surface temperature decrease agrees closely with faunal assemblage estimates (about −2 °C) for the same region[5-8,40,41], implying that any such effects on near-surface water are small.

We have assumed that eustatic and local sea levels are the same. Because the site of CH0182-36 is more than 200 km from the continental margin of eastern Florida, we suspect that there is little difference between eustatic and local sea levels. In any case, using a simple Airy model of isostatic compensation, we estimate that the difference between changes of eustatic and local sea level was at most 34 m. Consequently, our estimate of the glacial-interglacial change in mid-thermocline temperatures may be in error by up to 0.4 °C because of isostatic effects. The effects of even this maximum possible difference in sea level change would hardly be detected because the mid-thermocline temperature estimate from the $\delta^{18}O$ of *C. floridanus* is not more precise than about ±0.3 °C.

Our temperature estimates require that the effect of glacial ice volume on $\delta^{18}O_w$ has been correctly determined by Chappel and Shackleton[38]. However, the $\delta^{18}O$ difference between *G. ruber* and *C. floridanus* can be used to reconstruct the past vertical structure (i.e. temperature gradient) of the water column at Little Bahama Bank without this stipulation. As illustrated in Fig. 3, if the same thermocline structure existed during the glacial climate, then the glacial-interglacial range for *C. floridanus* should be 0.4‰ less than for *G. ruber*. Our measurements show that the $\Delta\delta^{18}O$ value for *C. floridanus* is 0.5‰ less than that of *G. ruber*. Thus no changes in thermocline structure are necessary to accommodate the differences between the surface water and mid-thermocline isotopic records. If our palaeotemperature estimates are correct, glacial cooling of the surface ocean affected at least the upper 600 m of the water column.

These results are consistent with inferences drawn from the simple ventilated thermocline model of Luyten *et al.*[3,42]. In this model, the structure of the thermocline reflects the latitudes at which isopycnal surfaces outcrop at the ocean surface and the strength of wind-driven Ekman pumping. During the last glacial maximum, stronger trade winds[5,8,43-49] and westerlies[5,50] increased Ekman pumping, and isopycnal surfaces outcropped at lower latitudes because of decreased surface temperature[5-8] and southward migration of the oceanic polar front[5,6,51]. Consistent with the model of Luyten *et al.*[3,41], our data indicate that the thermocline structure at the latitude, longitude and palaeodepth (~540 m) of CH0182-36 was relatively insensitive to the glacial-interglacial changes in either Ekman pumping or isopycnal outcrop location. The ~2 °C glacial cooling of the upper water column indicated by our data is consistent with the observation that much of the ocean surface where the isopycnal surfaces outcropped was ~2 °C cooler[5-8].

We thank D. Graham, L. Keigwin and G. P. Lohmann for critical reviews; S. Burns and A. C. Neumann for permission to sample CH0182-36; D. Olson for hydrographic data; W. A. Berggren for providing the correct identification of the shallow-water benthic *C. floridanus*; and, especially, D. Ostermann and J. Cole for help with foraminifera identification and oxygen-isotope analysis. Supported by a graduate fellowship from the WHOI/MIT Joint Program in Oceanography to N.C.S. and NSF grants to W.B.C. Collection and storage of CH0182-36 was supported by an NSF grant to A. C. Neumann and M. R. Boardman.

Received 22 September 1986, accepted 6 April 1987

1 Islen, C O'D *Trans. Am geophys Un* **20**, 414–417 (1939)
2 Jenkins, W J. *J. mar Res* **38**, 533-569 (1980)
3 Luyten, J., Pedlosky, J & Stommel, H *J Phys. Oceanogr* **13**, 292-309 (1983)
4 Luyten, J. & Stommel, H J *J phys Oceanogr* **16**, 1551-1560 (1986)
5 CLIMAP Project Members *Science* **191**, 1131-1137 (1976)
6 McIntyre, A. *et al. Geol. Soc. Am. Mem.* **145**, 43-76 (1976)
7 CLIMAP Project Members *Geol Soc Am. Map Chart Ser* 36 (1981)
8 Manabe, S. & Broccoli A J *J geophys Res* **90**, 2167-2190 (1985)
9 Burns, S J M. S thesis Univ North Carolina (1983)
10 Burns, S J & Neumann, A. C *Marine Geology* (Submitted)
11 Poag, C W *Ecologic Atlas of Benthic Foraminifera of the Gulf of Mexico* (Hutchison Ross, Stroudsburg, 1981)
12 van Morkhoven, F P C M., Berggren, W A & Edwards, A S *Cenozoic Cosmopolitan Deep-water Benthic Foraminifera* (Elf Aquitaine, Pau, 1986)
13 Curry, W B & Lohmann, G. P *Quat. Res.* **18**, 218-235 (1982)
14 Shackleton, N J., Imbrie, J & Hall, M A *Earth planet Sci. Lett* **65**, 233-244 (1983)
15 Shackleton, N J & Pisias, N G *Geophys Monog* **32**, 303-317 (1985)
16 Keigwin, L D., Corliss, B H., Druffel, E. R M & Laine, E P *Quat Res* **22**, 383-386 (1984)
17 Berger, W H., Killingley, J S & Vincent, E *Nature* **314**, 156-158 (1985)

18 Duplessy, J. C., Arnold, M., Maurice, P., Bard, E., Duprat, J. & Moyes, J. *Nature* **320**, 350–352 (1986)
19 Olson, D. B., Schott, F. A., Zantopp, R. J. & Leaman, K. D. *J. phys. Oceanogr.* **14**, 1470–1487 (1984)
20 Epstein, S. & Mayeda, T. *Geochim. cosmochim. Acta* **4**, 213–224 (1953)
21 Broecker, W. S. *Quat. Res.* **26**, 121–134 (1986)
22 Epstein, S., Buchsbaum, R., Lowenstam, H. & Urey, H. C. *Bull. geol. Soc. Am.* **64**, 1315–1326 (1953)
23 Craig, H. in *Proc. Spoleto Conf. on Stable Isotopes in Oceanographic Studies and Paleotemperatures* Vol. 3 (ed. Tongiorgi, E.) (1965)
24 Emiliani, C. *Am. J. Sci.* **252**, 149–158 (1954)
25 Jones, J. I. *Micropaleont.* **13**, 489–501 (1967)
26 Lidz, B., Kehm, A. & Miller, H. *Nature* **217**, 245–247 (1968)
27 Berger, W. H. *Deep Sea Res.* **16**, 1–24 (1969)
28 Shackleton, N. J. & Vincent, E. *Mar. Micropaleont.* **3**, 1–13 (1978)
29 Fairbanks, R. G., Wiebe, P. H. & Be, A. W. H. *Science* **207**, 61–63 (1980)
30 Curry, W. B. & Matthews, R. K. *Mar. Micropaleont.* **6**, 327–337 (1981)
31 Deuser, W. G. *Deep Sea Res.* (in the press)
32. Deuser, W. G. *Palaeogeogr. Palaeoclimatol. Palaeoecol.* **33**, 103–127 (1981)
33 Shackleton, N. J. & Opdyke, N. D. *Quat. Res.* **3**, 39–55 (1973).
34 Shackleton, N. J. in *Fate of Fossil Fuel CO_2* (eds Andersen, N. R. & Malahoff, A.) 401–427 (Plenum, New York, 1977)
35 Woodruff, F., Savin, S. M. & Douglas, R. G. *Mar. Micropaleont.* **5**, 3–11 (1980)
36 Belanger, P. E., Curry, W. B. & Matthews, R. K. *Palaeogeogr. Palaeoclimatol. Palaeoecol.* **33**, 205–220 (1981)
37 Graham, D. W., Corliss, B. H., Bender, M. L. & Keigwin, L. D. *Mar. Micropaleont.* **6**, 483–497 (1981)
38 Chappell, J. & Shackleton, N. J. *Nature* **324**, 137–140 (1986)
39 Fairbanks, R. G. & Matthews, R. K. *Quat. Res.* **10**, 181–196 (1978)
40 Hunter, G. E. M. S. thesis Miami Univ. (1984)
41 Boardman, M. R., Neumann, A. C., Baker, P. A., Dulin, L. A., Kenter, R. J., Hunter, G. E. & Kiefer, K. B. *Geology* **14**, 28–31 (1986)
42. Luyteen, J., Pedlosky, J. & Stommel, H. *Clim. Change* **5**, 183–191 (1983)
43 Hays, J. D. & Perruzza, A. *Quat. Res.* **2**, 355–362 (1972)
44 Parkin, D. W. & Shackleton, N. J. *Nature* **245**, 455–457 (1973)
45 Parkin, D. W. *Proc. R. Soc. Lond. A* **337**, 73–100 (1974)
46. Parkin, D. W. & Padgham, R. C. *Proc. R. Soc. Lond. A* **346**, 245–260 (1975)
47 Gates, W. L. *Science* **191**, 1138–1144 (1976)
48. Gardner, J. V. & Hays, J. D. *Geol. Soc. Am. Mem.* **145**, 221–246 (1976)
49 Kolla, V., Biscaye, P. E. & Hanley, A. *Quat. Res.* **11**, 261–277 (1979)
50. Kutzbach, J. E. & Guetter, P. J. *J. atmos. Sci.* **43**, 1726–1759 (1986)
51. Ruddiman, W. F. & McIntyre, A. *Quat. Res.* **3**, 117–130 (1973)

Chapter 3

Physical structure and carbon cycling within the glacial thermocline of the western subtropical North Atlantic

3.1 Heading

Benthic foraminifera shells accumulating on the margins of the Bahamas Banks had higher $\delta^{18}O$ and $\delta^{13}C$ during the last glaciation than today. These data show that glacial North Atlantic thermocline waters were colder, better ventilated and depleted of nutrients. Such changes result from the direct response of thermocline circulation to glacial surface ocean climate.

3.2 Introduction

The subtropical gyre of the western North Atlantic is characterized by a steep gradient in temperature, or main thermocline, that extends from the base of the surface mixed layer (~150 m) to uniformly cool deep waters (~1200 m). Pedlosky [1990] has reviewed the dynamics of gyre circulation. Within the thermocline, gradients of water properties with depth reflect the lateral flow of water along isopycnal surfaces. Wind-driven Ekman transport and bouyancy (density) flux drive water into the thermocline when isopycnals outcrop at the ocean surface during late winter. Water then flows along isopycnals to greater depths at lower latitudes along paths that minimize changes in potential vorticity. In this "ventilated" region of the thermocline, the fluxes and trajectories of water and therefore its

vertical structure, depend largely on the climatic conditions at the ocean surface where and when isopycnals outcrop.

Together with circulation, biological processes control the vertical distribution of nutrients in the thermocline. Marine plants produce oxygen and deplete surface waters of nutrients and isotopically-light carbon, while the decomposition of settling organic matter at depth consumes oxygen and releases nutrients and isotopically-light carbon back into the water. As a result, concentrations of phosphate, nitrate, silicate and total dissolved inorganic carbon all increase with depth, and the concentration of dissolved oxygen and the $\delta^{13}C$ of the dissolved inorganic carbon decrease [Spencer, 1972; Kroopnick et al., 1972]. The steepness of gradients in these parameters reflects the fact that the thermocline is the principal site of nutrient and carbon cycling in the oceans, that is, ~90% of the organic matter produced in the surface mixed layer is recycled before sinking through the base of the thermocline [see Broecker and Peng, 1982; Sundquist, 1985].

Abundant evidence exists for glacial-interglacial changes in surface ocean climate and the chemistries of the atmosphere and ocean (see below). Such changes relate in a predictable manner to the bathymetric distributions of temperature and nutrients within the thermocline. By accurately reconstructing these distributions for times in the past, strong constraints can be placed on the mechanisms driving these changes. In this paper, $\delta^{18}O$ and $\delta^{13}C$ of benthic foraminifera from a suite of Bahamaian sediment cores provide the basis of the first detailed reconstructions of the temperature and nutrient distributions of the glacial thermocline. These distributions reflect thermocline circulation and are interpreted in terms of glacial surface ocean climate.

3.3 Geologic and oceanographic setting

We focused our efforts on the margins of Little Bahama Bank and Great Bahama Bank which bound the eastern end of Northwest Providence Channel for two reasons (Fig. 1). First, the banks are one of the few topographic features in the western North Atlantic where benthic foraminifera live and which intersect subtropical-gyre thermocline waters. Second, prior experience indicated that it would be possible to recover undisturbed, continuously deposited sequences of sediments that contained abundant benthic foraminifera [Mullins

and Neumann, 1979; Burns and Neumann, 1987; Slowey and Curry, 1987].

Northeast and Northwest Providence Channels form a seaway that connects the western North Atlantic basin with the Florida Straits. The hydrography of the seaway is reviewed in Chapter 1. Today, temperature–salinity, oxygen–density and temperature–depth relationships of thermocline and underlying waters within the seawway are characteristic of the Sargasso Sea and North Atlantic Deep Water and flow is dominantly westward from the Atlantic toward the Florida Straits. We assume that this was also the case during the last glaciation. While some flow of water from the Florida Straits into the western end of Northwest Providence Channel does occur, such events are relatively uncommon and of short duration. More importantly, they are confined to waters shallower than ~275 m, that is, above the main thermocline. Noting that the intrusion of western North Atlantic water from Northwest Providence Channel into the Florida Straits does not extend below ~450 m, Wennekens [1959] suggested that an underwater sediment spur, which extends along the seafloor from the western tip of Great Bahama Bank past the southern margin of Little Bahama Bank, isolates deeper waters in Northwest Providence Channel from those in the Florida Straits. During the last glacial maximum, the spur would have been even shallower as sea level was lower at that time.

At our study site, the margin of Little Bahama Bank is steep and irregular due to a series of ridges and gullies extending down its face; the margin of Great Bahama Bank is more gently sloping and broader [Mullins and Neumann, 1979; Burns and Neumann, 1987]. Though downslope processes were once active, high-resolution seismic profiles display continuous, parallel, unbroken reflectors, indicating that veneer of Quaternary periplatform ooze now drapes both margins [Mullins and Neumann, 1979; Mullins et al., 1979; Burns and Neumann, 1987]. The compositions and downcore stratigraphies of late Quaternary sediment samples recovered from the margins also display few effects of downslope processes such as turbidity and grain flows [Mullins and Neumann, 1979; Boardman and Neumann, 1984; Burns and Neumann, 1987].

In addition to the normal rain of pelagic detritus, periplatform ooze contains fine-grained algal debris and other bank-top derived material that is composed primarily of aragonite and magnesian calcite [Schlager and James, 1978]. This material is suspended into the water

column by tides and storms and then settles through the water column to the seafloor [Neumann and Land, 1975; Boardman and Neumann, 1984]. Importantly, changes in the aragonite content of the ooze corresponds closely with changes in climate as indicated by foraminiferal $\delta^{18}O$ such that it is greatest during interglaciations and least during glaciations [Droxler et al., 1983; Boardman et al., 1986]. Two explanations have been suggested: (1) aragonite production is greater when the bank tops are flooded during interglacial highstands of sea level [Kier and Pilkey, 1971; Boardman and Neumann, 1984; Boardman et al., 1986], and (2) aragonite dissolution on the seafloor is greater during glaciations [Lynts, 1973; Droxler et al., 1983; Droxler, 1985]. As a result of fluctuations of aragonite content, the sedimentation rates of periplatform ooze are typically higher during interglacials than during glacials [e.g. Kier and Pilkey, 1971; Droxler et al., 1983; Boardman et al., 1986; Burns and Neumann, 1987].

3.4 Methods and core stratigraphies

A suite of giant gravity cores (GGC, 4 inch diameter), jumbo piston cores (JPC, 4 inch diameter) with trigger weight cores (TC), and box cores (BC) were recovered from the study site in December, 1988, during *RV Oceanus* cruise 205–2. Whenever possible, we recovered these cores from ridge crests and other local topographic highs to avoid the possible influence of downslope processes. Two previously existing standard piston cores (PC, 2.25 in diameter) were also available [Burns and Neumann, 1987]. Fig. 2 and Table 1 show the location, water depth and length of recovery of the cores utilized in this study. Core sites are from a limited area along the bank margins with a depth distribution (425–1534 m) that spans almost the entire thermocline and extends into upper North Atlantic Deep Water.

Two approaches were followed to check the stratigraphic integrity of the gravity and piston cores. First, each core was visually inspected, then sampled at 10 cm intervals and the percentage of aragonite relative to total aragonite and calcite in bulk sediment was determined using x-ray diffraction [after Neumann, 1965, see Appendix to this Chapter]. As noted above, previous work by Droxler et al. [1983] and Boardman et al. [1986] has shown a strong correspondence of aragonite percentage with foraminiferal $\delta^{18}O$ in this region.

The standard deviation of duplicate determinations is about ±1%. The algorithim used to analyze x-ray data slightly over-estimated the aragonite content of some glacial samples that contained quartz. Therefore, on average, true glacial-interglacial ranges in aragonite content are about 4 percent greater than presented here. This difference in no way affected the stratigraphic interpretation of the aragonite percentages. If sedimentation appeared continuous and undisturbed from the last glaciation through the recent Holocene, the core was resampled at ~3 cm intervals near its top and across the glacial-aged section. Shells of the planktonic foraminifera *Globogerinoides sacculifer* (300–350 μm) were picked from each sample and their oxygen isotopic composition measured on a VG Micromass 602E mass spectrometer at the Woods Hole Oceanographic Institution using standard methods [Curry and Lohmann, 1982]. Replicate analyses of the standard NBS-20 indicate that analytical precision is better than ±0.1 per mil.

Sediments deposited during the recent Holocene and last glacial maximum (LGM) were identified in each core based on these two stratigraphies (Fig. 3). While the stratigraphic relationships of the other cores are straightforward, it was clear from the shape of the aragonite profile of core 120JPC that some Holocene sediments were missing and so it has been spliced together with its trigger weight core (120T). High aragonite content and low $\delta^{18}O$ values confirm that core-top sediments are recent Holocene while low aragonite and high $\delta^{18}O$ typify glacial sediments. Sediments spanning the depths where *G. sacculifer* $\delta^{18}O$ is most positive are taken to be from the LGM [Emiliani, 1955; Shackleton and Opdyke, 1973]. When two glacial $\delta^{18}O$ maxima occurred, the youngest was chosen. If the ages of this event is 18 kyrs [Mix and Ruddiman, 1985; Bard et al., 1990] and the core tops are 0 kyrs, then the average glacial to recent sedimentation rates for the cores range from about 3 to 13.5 cm/kyr. Since the supply of aragonite from the bank tops is greater during interglaciations, it is likely actual interglacial sedimentation rates are greater than these averages and glacial rates are lower.

The LGM to recent Holocene ranges of aragonite content and *G. sacculifer* $\delta^{18}O$ are all about 28 to 74% and -1.6 to 0.3 per mil, respectively, suggesting no significant disturbance by bioturbation or coring processes. Sediments in core 7JPC may be an exception, as they display a low sedimentation rate and the smallest ranges of aragonite content and

foraminiferal $\delta^{18}O$ (see benthic values below). Core 149JPC barely penetrated the glacial sediments. Thus, while the aragonite content and $\delta^{18}O$ of *G. sacculifer* at its base are consistent with a LGM age, we cannot be certain on this basis alone.

The shell compositions of *Planulina* species of benthic foraminifera are believed to faithfully record gradients of $\delta^{13}C$ in ΣCO_2 and $\delta^{18}O$ of ambient seawater [Belanger et al., 1982; Graham et al., 1982]. As no one species of *Planulina* is found over the entire range of thermocline depths [e.g. van Morkhoven et al., 1986], shells (>250 μm) of several species—*P. foveolata* (shallowest), *P. ariminensis* and *P. wuellerstorfi* (deepest)—were picked from the recent Holocene and LGM sediments for analysis. Isotope ratios were measured using a Carousel-48 automatic preparation system attached to a Finnigan-MAT 251 mass spectrometer at Lamont-Doherty Geological Observatory. In contrast to the procedure followed at Woods Hole, shells were not crushed prior to reaction with acid and the acid temperature was 90°C instead of 50°C. The means of the standard deviations of 15 duplicate analyses of foraminiferal $\delta^{18}O$ and $\delta^{13}C$ were 0.053 and 0.023 per mil, respectively.

Using data from Zahn et al. [1987] and our data presented here for the Bahamas, the isotopic compositions of *P. ariminensis* and *P. wuellerstorfi* are compared (Fig. 4). Zahn et al. ignored about half of their data because it had large inter-species differences due to bioturbational mixing. Two points of the Bahamas data (identified by the symbol '?') were not used in determining the mean isotopic compositions of the foraminifera because we suspect slight downslope creep of *P. ariminensis* shells. Their $\delta^{18}O$ values are like the *P. ariminensis* found ~50–150 m further up the bank margins (see Fig. 6 below). As the gradient of water column $\delta^{13}C$ is greatest over these depths, this might explain the particularly large differences between the $\delta^{13}C$ of these *P. ariminensis* and *P. wuellerstorfi*. The mean $\delta^{18}O$ of *P. ariminensis* is 0.1 per mil less than that of *P. wuellerstorfi* and the mean $\delta^{13}C$ of *P. ariminensis* is 0.02 per mil greater than that of *P. wuellerstorfi*. For these species, the means of $\delta^{13}C$ and $\delta^{18}O$ are essentially the same (given the analytical precision of the measurements) and changes in their isotopic compositions correspond nearly one to one one. Therefore, these data can be combined to produce a single profile.

3.5 Ventilation and nutrient concentrations

Fig. 5 shows the measured concentration of phosphate in the water column, the estimated $\delta^{13}C$ of the dissolved inorganic carbon in the water column and the measured $\delta^{13}C$ of *Planulina* species in both recent Holocene and glacial maximum sediments. The water $\delta^{13}C$ estimates are based upon along-isopycnal differences in phosphate between the GEOSECS II hydrographic station [Spencer, 1972; Kroopnick et al., 1972] and the Bahamas, assuming phosphate and carbon are released into the water from "Redfield" organic matter with $\delta^{13}C$ of -18.1 per mil. To correct for lower sea level, 120 m was subtracted from the depths of LGM foraminifera [Fairbanks, 1989]. Importantly, the $\delta^{13}C$ profile of recent Holocene benthic foraminifera reaches a minimum at about the same depth as the characteristic lower thermocline maximum of nutrients and minima of dissolved oxygen and the $\delta^{13}C$ of the dissolved inorganic carbon within the modern North Atlantic subtropical gyre. This close correspondence lends confidence to the use of fossil $\delta^{13}C$ as a proxy for past phosphate and oxygen concentrations and indicates that modern foraminifera were not significantly affected by downslope transport. In this carbonate platform environment, downslope processes are even less active during the glacial lowstand of sea level [Mullins, 1983; Droxler and Schlager, 1985].

Bathymetric profiles of modern North Atlantic subtropical gyre waters typically display a maximum in phosphate and minimum in dissolved oxygen concentrations near the base of the thermocline. A minimum of the $\delta^{13}C$ in ΣCO_2 occurs at the same depth—consistent with biological consumption of O_2 and the release of phosphate and ^{13}C during organic matter degradation [Kroopnick et al., 1972]. These extrema occur in waters where the potential density anomaly ranges from about 27.2 to 27.5 kg/m^3. They reflect the presence of poorly-ventilated lower thermocline waters separating well-ventilated, oxygen-rich shallow thermocline waters and intermediate depth Labrador and Mediteranean Sea waters [e.g. Jenkins, 1980; Sarmiento et al., 1982]. Vertical diffusion cannot by itself account for the presence of the oxygen minimum because lateral advection of water along isopycnals is much more significant than vertical mixing [Jenkins, 1980]. However, several other processes may be involved.

The concentration of dissolved oxygen in thermocline waters primarily reflects how well

ventilated they are to the atmosphere. Waters remain saturated with dissolved oxygen while at the ocean surface; but once they are subducted into the thermocline, biological consumption outpaces supply by advection or diffusion, and the concentration of oxygen falls. Waters corresponding to isopycnals that outcrop along the surface of the subtropical gyre belong to the "ventilated" region of the thermocline [Luyten et al., 1983a]. Driven directly into the thermocline by Ekman pumping and bouyancy flux, they circulate rapidly around the gyre and are frequently ventilated as indicated by high tritium concentrations and young tritium–^{3}He ages [Broecker and Ostlund, 1979; Jenkins 1980, 1987, 1988; Sarmiento et al., 1982]. In contrast, the isopycnal surfaces that correspond to the oxygen minimum are poorly ventilated. They are deeper and outcrop farther north in the subpolar gyre—north of the line of zero wind stress curl—where Ekman upwelling occurs, which does not contribute to ventilation [Jenkins, 1980, 1987, 1988; McCartney, 1982; Sarmiento, 1982; Luyten et al., 1983a]. Waters may also circulate about the subpolar gyre before communicating with the subtropical gyre, during which time oxygen is depleted and nutrients are accumulated [Sarmiento et al., 1982; Pedlosky, 1990; McCartney, personal communication]. To some extent, the oxygen minimum of the North Atlantic thermocline may be enhanced by mixing with older (in this sense, poorly ventilated), low-oxygen waters from the south [Jenkins, 1980; Tsuchiya, 1989]. The volume of poorly-ventilated, low-oxygen waters increases along the southeastern margin of the gyre [e.g. Sarmiento et al., 1982; Kawase and Sarmiento, 1985; Jenkins, 1987]. This increase is consistent with the "shadow" zone predicted as a consequence of the anticyclonic trajectory of water subducted from the gyre surface [Luyten et al., 1983a]. Yet, the actual contribution of this mechanism cannot be evaluated until after the physical circulation in the region is considered [Stramma and Siedler, 1988; Spall, 1990]. Finally, degradation of organic matter beneath the upwelling zone off of Africa also contributes to the oxygen depletion of these waters [e.g. Menzel and Ryther, 1968].

The recent Holocene and glacial maximum δ^{13}C profiles differ in two significant ways. Glacial δ^{13}C values are at least 0.1–0.2 per mil more positive than recent Holocene values and as much as 0.6 per mil more positive at the depth of the modern ocean δ^{13}C minimum. The LGM profile does not possess a local minimum, rather, δ^{13}C values decrease steadily from the upper thermocline to greater depths. These data are consistent with greater, more

uniform ventilation rates for thermocline waters driven by glacial surface ocean climate. During the LGM, geologic evidence and climatic models suggest stronger trade winds [e.g. Hays and Perruzza, 1972; Parkin and Shackleton, 1973; CLIMAP, 1976; Gates, 1976; Gardner and Hays, 1976; Manabe and Hahn, 1977; Kolla et al., 1979; Sarnthein et al., 1982; Manabe and Broccoli, 1985; Kutzbach and Guetter, 1986] and westerlies [Manabe and Broccoli, 1985; Kutzbach and Guetter, 1986], implying stronger Ekman pumping and greater thermocline ventilation. The models emphasize that the westerlies flowed along the margin of sea ice. Therefore, in contrast to today, all glacial thermocline isopycnals outcropped in the region of Ekman downwelling south of the zero wind stress curl line and so all were well ventilated.

A model by Boyle [1986] illustrated that increased wind-driven ventilation of the upper thermocline would lead to lower nutrient concentrations. Our results are consistent with this suggestion, though whereas Boyle focused on increased low-latitude pumping, we suggest that the high-latitude processes, such as increased strength and shift in the position of the westerlies, were also quite significant. It is only at higher latitudes that all thermocline isopycnals are ventilated and subject to direct atmospheric forcing.

An anticipated consequence of higher ventilation rates is that the concentration of nutrients in thermocline waters decreases. To infer a change in the concentration of the nutrient phosphate from foraminiferal $\delta^{13}C$ requires knowledge of the $\delta^{13}C$ to phosphate ratio in seawater. Core-top benthic foraminifera are assumed to be on average at least 100 years old, so their $\delta^{13}C$ does not reflect the input into the oceans of isotopically light CO_2 from fossil fuels; in contrast, the $\delta^{13}C$ of rapidly ventilated thermocline waters to some extent does [Broecker and Peng, 1982]. Based upon the mean ocean $\delta^{13}C$ to phosphate ratio of Broecker and Peng [1982] (-0.93 per mil/μmol kg^{-1}) which has been corrected for this effect, the phosphate concentrations of glacial thermocline waters were from about 0.1 to 0.65 μmol kg^{-1} less than today—the biggest difference occurring at the depth of the modern $\delta^{13}C$ minimum. It is currently estimated that the mean $\delta^{13}C$ of glacial ocean water was $\sim$0.3 per mil less than during the recent Holocene [Curry et al., 1988; Duplessy et al., 1988] due to the transfer of ^{12}C encriched terrestrial carbon to the oceans [Shackleton, 1977]. Taking this into account, glacial phosphate concentrations within the thermocline must have been

from about 0.4 to 0.9 μmol kg^{-1} less than today. The δ^{13}C to phosphate ratio and decrease in mean ocean δ^{13}C are consistent with the changes in Cd/Ca and δ^{13}C reported by Boyle and Keigwin [1987] for Carribean core KNR 65 Sta 5 core 5PG.

3.6 Temperature gradient

Bathymetric profiles of temperature, the δ^{18}O of equilibrium calcite and the measured δ^{18}O in both recent Holocene and LGM *Planulina* species are shown in Fig. 6. To correct for lower sea level, 120 m was subtracted from the depths of LGM foraminifera [Fairbanks, 1989]. The δ^{18}O of equilibrium calcite was calculated using $\delta^{18}O_w$–salinity relations for the Sargasso Sea (R. Fairbanks, personal communication) and the paleotemperature relationship of Erez and Luz [1983]. Like Zahn and Mix [submitted], we find that this relationship (offset by -1.0 per mil) compares better with foraminiferal δ^{18}O than either the Craig [1965] modification of the Epstein et al. [1953] relationship (offset by -1.0 per mil) or the relationship of O'Neil et al. [1969] (offset by -1.0 per mil) (Fig. 7). The average difference between foraminiferal and equilibrium δ^{18}O is about -1.0 per mil, within the range of -0.64 to -1.0 reported for individual *Planulina* and *Cibicidioides* species [e.g. Shackleton and Opdyke, 1973; Shackleton, 1977; Woodruff et al. 1980; Belanger et al., 1981; Graham et al., 1981].

If we assume that vital effects on foraminiferal δ^{18}O and the bathymetric gradients of the δ^{18}O of water remain constant through time, then bathymetric gradients of foraminiferal δ^{18}O can be used to *estimate* temperature gradients. The foraminiferal δ^{18}O gradient is steeper during the LGM than during the recent Holocene. After subtracting 1.2 per mil from LGM values to account for the mean change in the δ^{18}O of ocean water due to increased glacial ice volume [Fairbanks, 1989], the LGM–recent Holocene difference in δ^{18}O ranges from about 0.2 to 0.7 per mil with increasing depth which is roughly equivalent to temperature decreases of about 1 to 3 °C during the LGM. Thus, the upper 1500 m of the water column was cooler by at least 1 °C during the LGM—the deepest waters were several degrees cooler. This is consistent with the general wintertime latitudinal sea surface temperatures and their gradients indicated by CLIMAP [1976, 1981] and climate models [Manabe and Broccoli, 1985; Kutzbach and Guetter, 1986], that is, the source waters of the glacial thermocline. From their model, Luyten et al. [1983b] infer that the response of

thermocline structure to changes in wind stress is mostly local. At a western, low-latitude location like the Bahamas, the base of the thermocline would deepen if low-latitude Ekman pumping doubled, while it would not show much effect if high-latitude pumping increased. Within the resolution of the data, the break in slope that marks the thermocline–deep water boundary (~1100 m during the recent Holocene) was shallower by ~100 m during the LGM. Either glacial trade winds were not greatly increased during the LGM, or the model with boundary conditions of Luyten et al. [1983b] do not adequately reflect the glacial ocean.

3.7 Intermediate depth waters

Evidence exists for nutrient-depleted intermediate-depth waters in the Atlantic during the LGM [Cofer-Shabica and Peterson, 1986; Boyle and Keigwin, 1986, 1987; Oppo and Fairbanks, 1987; Zahn et al., 1987]. Zahn et al. [1987] attributed glacial ^{13}C enrichment of waters along the northwest margin of Africa to increased outflow of Mediterranean water. Oppo and Fairbanks [1987] contend that the nutrient depletion observed at other points in the Atlantic basin reflects the presence of the Mediterranean water. Due to lower sea level, Duplessy et al. [1988] suggest the Mediterranean outflow would have decreased during the LGM, and Boyle and Keigwin [1987] argue it is unlikely that the volume of Mediterranean outflow would be sufficient to so strongly affect the character of intermediate depth water as far west as the Caribbean. The distribution of preliminary foraminiferal Ba/Ca data from Caribbean and Mediterranean cores also conflicts with the notion of greatly enhanced influence of glacial Mediterranean water [Lea, 1990].

Boyle and Keigwin [1987] suggest that less-saline, nutrient-depleted North Atlantic surface waters formed intermediate waters during the last glaciation. That northern source waters extended as far south as the passages leading to the Caribbean is consistent with both $\delta^{13}C$ [Oppo and Fairbanks, 1989] and preliminary Ba/Ca data [Lea, 1990].

To shed light on the processes involved in the glacial ^{13}C enrichment of Mediterranean water and the origins of glacial intermediate depth waters, Figs. 8 and 9 show glacial isotopic compositions of *Planulina* and *Cibicidoides* species from the Bahamas, the Caribbean, the Mediterranean, the African margin by Gibraltar and the intermediate-depth North Atlantic [Boyle and Keigwin, 1987; Oppo and Fairbanks, 1987; Zahn et al., 1987]. So that the

data could be considered in the context of mixing among water masses, end members for water types were identified in the fashion of Oppo and Fairbanks [1987]: wintertime, low-latitude North Atlantic surface water (wNASW); Mediterranean Intermediate Water (MIW); Northern Component Water (NCW); southern component water and North Atlantic Intermediate Water (NAIW). Oppo and Fairbanks [1987] note that the type data they chose for NCW actually contains a southern component in addition to its primary northern character, therefore, core V28–14 [Curry et al., 1988] is also included in the hopes of being a more representative end member. Data from low-latitude, intermediate-depth cores are also shown (KW–31, 1181 m [Pastouret et al., 1978]; BT4, 1000 m [Curry et al., 1988]). Finally, there are no data available from the South Atlantic thermocline and so at this time the influence of these waters cannot be considered.

Existing Ba/Ca data [Lea, 1990] plotted versus the isotopic ratios provides an additional constraint (Figs. 9b and 10). We have converted the Ba/Ca of glacial planktonic foraminifera [Lea, 1990] to an equivalent benthic Ba/Ca using the appropriate distribution coefficients [Lea, 1990] and assumed it applies to wNASW. This assumption is consistent with the uniform distribution of Ba in surface waters of the modern North Atlantic [GEOSECS executive committee, 1987].

There is a general trend of decreasing $\delta^{13}C$ with increasing $\delta^{18}O$, consistent with a steady transitions between thermocline waters and NAIW and between NAIW and deep waters with a both northern and southern components. While NAIW falls between southern water, MIW and wNASW in $\delta^{13}C$–$\delta^{18}O$ space (Figs. 8 and 9a), it does not in either $\delta^{13}C$–Ba/Ca or Ba/Ca–$\delta^{18}O$ space (Figs. 9b and 10), indicating that NAIW cannot be simply a mixture of MIW, wNASW and southern waters.

Several possibilities remain: (1) NAIW is a mixture of wNASW, northern and southern component waters (Fig. 9c), (2) NAIW is a mixture of wNASW, MIW and northern component waters (Fig. 9d), (3) NAIW is a discrete water mass. NAIW falls directly on the mixing line between wNASW and northern component water, that is, along the edge of the mixing fields in possibilities (1) and (2). Assuming core V28–14 represents northern component water, any contribution of MIW or southern waters to NAIW must be minimal. Further Ba/Ca data may help to constrain whether NAIW could be a mixture between

these wNSW and deep northern component water or is a discrete water type. If core V28–14 actually reflects a mixture of northern and southern waters then NAIW will fall within the wNASW, northern and southern component water mixing field and southern waters could contribute to NAIW (Fig. 9e). NAIW would be out of the wNASW, MIW and northern water mixing field and, again, MIW could not contribute to NAIW (Fig. 9f).

In the North Atlantic today, the thermocline is underlain by Upper North Atlantic Deep Water—Labrador Sea waters along the western margin of the basin and waters which contain a percentage of MIW in the central and eastern part of the basin [e.g. Wust, 1978; Worthington, 1976; Talley and McCartney, 1982]. MIW quickly entrains Atlantic waters as it leaves the Mediterranean so that MIW makes up only ~1/4 of outflow waters near Gibraltar [e.g. Oppo and Fairbanks, 1987, Fig. 1] and less than 1/10 of the waters in the western portion of the basin [e.g. Wust, 1978]. The $\delta^{13}C$ of Zahn et al. [1987] suggest that MIW was similarly diluted as it entered the Atlantic near Gibraltar during the LGM. Yet, the $\delta^{13}C$ values of glacial Bahamas foraminifera equal or exceed the maximum values reported by Zahn et al. [1987] for the Mediterranean outflow waters (Fig. 8). Thus, unless these outflow waters crossed the ocean basin without entraining any other waters—which seems unlikely—MIW could not have been the main source of the high $\delta^{13}C$ found in the western North Atlantic during the LGM.

During the LGM, the $\delta^{13}C$ of the shallow thermocline waters at the Bahamas were at least ~0.1–0.2 per mil greater than that of MIW and the difference between surface ocean and MIW was probably greater still. If all glacial North Atlantic thermocline waters were similarly enriched, then ^{13}C enrichment of MIW would occur if for no other reason than its surface ocean source waters were similarly enriched. As a consequence of stronger glacial Ekman pumping, a decrease in the size of the oxygen-depleted "shadow" region along the eastern margin of the gyre [Luyten et al., 1983a] might enhance the increase in the $\delta^{13}C$ of these waters.

3.8 Summary and speculation

Thermocline circulation in the North Atlantic subtropical gyre responds directly to the driving forces of surface ocean climate. During the last glaciation, the nutrient concentrations

and the temperatures of thermocline waters decreased and a poorly-ventilated oxygen minimum layer did not exist. These changes are consistent with our understanding of the physics of thermocline circulation and evidence for stronger winds and cooler wintertime surface ocean temperatures. We suggest that because of the influence of glacial ice on the strength and position of the westerlies, all thermocline isopycnals outcropped within the zone of Ekman downwelling and so were well ventilated. Boyle [1986] has previously shown how increased wind-driven, low-latitude upwelling could lead to such a vertical re-distribution of nutrients. Glacial North Atlantic Intermediate waters originating within the gyre and the Mediterranean would thus form with low initial nutrient concentrations. The contribution to these waters from the Mediterranean was minimal [Boyle and Keigwin, 1987].

Our thermocline data together with prior evidence from intermediate depths shows that the entire upper water column of the North Atlantic was depleted in ^{12}C and nutrients during the last glacial maximum while deep waters were enriched. This observation is significant because Boyle [1988] envisions a major role for such nutrient re-distribution in controlling concentrations of atmospheric CO_2.

Further thermocline reconstructions are necessary to verify that the nutrient depletion observed at the Bahamas was a gyre-wide phenomenon and to sort out the variable response of thermocline structure to local climatic forcing both in the North Atlantic and in other oceans. Finally, our consideration has focused on changes in the wind-driven component of thermocline ventilation because data on changes in glacial winds exists, and our understanding of the physics of the modern thermocline can accommodate it. Yet, bouyancy flux processes also play a significant role in thermocline ventilation [Sarmiento et al., 1982; Woods, 1985; Luyten and Stommel, 1986] and must be considered if the response of ocean circulation to climatic change is to be fully understood.

3.9 References

Bard, E., Hamelin, B., Faribanks, R. G., & Zindler, A., *Nature* **345,** 405–410 (1990).

Belanger, P. E., Curry, W. B., & Matthews, R. K., *Palaeogeogr. Palaeoclimatol. Palaeoecol.* **33,** 205–220 (1981).

Boardman, M. R., & Neumann, A. C. *J. Sed. Pet.* **54,** 1110–1123 (1984).

Boardman, M. R., Neumann, A. C., Baker, P. A., Dulin, L. A., Kenter, R. J., Hunter, G. E., & Keifer, K. B., *Geology* **14,** 28–31 (1986).

Boyle, E. A., in *Mesozoic and Cenozoic Oceans* (ed Hsu, K. J.,) 49–60 (AGU, Washington, D.C., 1986).

Boyle, E. A., & Keigwin, L., *EOS Trans. AGU* **67,** 868–869 (1987).

Boyle. E. A., & Keigwin, L., *Nature* **330,** 35–40 (1987).

Boyle, E. A., *J. Geopys. Res.* **93,** 15701–15714 (1988).

Broecker, W. S., & Ostlund, H. G., *J. Geophys. Res.* **84,** 1145–1154 (1979).

Broecker, W.S., & Peng, T-H., Tracers in the Sea, (Eldigio Press, New York, 1982).

Burns, S. J., & Neumann, A. C., *Mar. Geol.,* **77,** 277–286, (1987).

CLIMAP Project Members, *Science* **191,** 1131–1137 (1976).

CLIMAP Project Members, *Geol. Soc. Am. Map Chart Ser.* **36,** (1981).

Cofer-Shabica, N. B., & Peterson, L. C., *Geol. Soc. Am. Abstracts with Programs* **18,** 567 (1986).

Craig, H., in *Proc. Spoleto Conf. on Stable Isotopes in Oceanographic Studies and Paleotemperatures* Vol. 3 (ed Tongiorgi, E.,) (1965).

Curry, W. B., & Lohamnn, G. P., *Quat. Res.* **18,** 218–235 (1982).

Curry, W. B., Duplessy, J. C., Labeyrie, L. D., & Shackleton, N. J., *Paleoceanography* **3,** 317–341 (1988).

Droxler, A. W., in *The carbonate cycle and atmospheric CO_2: Natural variations from Archean to present* (eds Sundquist, E. T., & Broecker, W. S.) 195–207 (AGU, Washington, D.C., 1985).

Droxler, A. W., & Schlager, W., *Geology* **13,** 799–802 (1985).

Droxler, A. W., Schlager, W., & Whallon, C. C., *Geology* **11,** 235–239 (1983).

Duplessy, J.-C., Shackleton, Fairbanks, R. G., Labeyrie, L., Oppo, D., & Kallel, N., *Paleoceanography* **3,** 343–360 (1988).

Emiliani, C., *J. Geol.* **63,** 538–578 (1955).

Epstein, S., Buchsbaum, R., Lowenstam, H. A., & Urey, H. C., *Geol. Soc. Am. Bull.,* 64, 13115–1325, 1953.

Erez, J., & Luz, B., Geochim. Cosmochim. Acta **47,** 1025–1031 (1983).

Fairbanks, R. G., *Nature* **342,** 637–642 (1989).

Gardner, J. V., & Hays, J. D., in *et al. Geol. Soc. Am. Mem.* **145,** (eds Cline, R. M., and Hays, J. D.) 221–146 (1976).

Gates, W. L., *Science* **191,** 1138–1144 (1972).

GEOSECS executive committee *GEOSECS Atlantic, Pacific, and Indian Ocean Expeditions, volume 7: Shorebased Data and Graphics* (National Science Foundation, Washington, D.C., 1987).

Graham, D. W., Corliss, B. H., Bender, M. L., & Keigwin, L. D., *Mar. Micropaleont.* **6,** 483–497 (1981).

Hays, J.D., & Perruzza, A., *Quat. Res.* **2,** 355–362 (1972).

Jenkins, W. J. *J. mar. Res.* **38,** 533–569 (1980).

Jenkins, W. J. *J. Phys. Oceanogr.* **17,** 7633–783 (1987).

Jenkins, W. J. *Phil. Trans. R. Soc. Lond.* A **325,** 43–61 (1988).

Kawase, M., & Sarmiento, J. L., *J. Geophys. Res.* **90,** 8961–8979 (1985).

Keir, J. S., & Pilkey, O. H., *Mar. Geol.* **11,** 189–200 (1971).

Kolla, V. E., Biscaye, P. E., & Hanley, A., *Quat. Res.* **11,** 261–277 (1979).

Kroopnick, P., Weiss, R. F., & Craig, H., *Earth planet. Sci. Lett.* **16,** 103–110 (1972).

Kutzbach, J. E., & Guetter, P. J., *J. Atmos. Sci.* **43,** 1726–1759 (19).

Lea, D. W., Foraminiferal and Coralline Barium as Paleoceanographic Tracers, *PH.D. Thesis, MIT/WHOI,* **WHOI–90–06** 173 pp (1990).

Luyten, J., Pedlosky, J. & Stommel, H. *J. Phys. Oceanogr.* **13,** 192–309 (1980).

Luyten, J., Pedlosky, J. & Stommel, H. *Climatic Change* **5,** 183–191 (1983).

Luyten, J., & Stommel, H. *J. Phys. Oceanogr.* **16,** 1551–1560 (1986).

Lynts, G. W., Judd, J. B., & Stehmen, C. F., *Geol. Soc. Am. Bull.* **84,** 2665–2684 (1973).

Manabe, S., & Broccoli, A. J., *J. Geophys. Res.* **90,** 2167–2190 (1985).

Manabe, S., & Hahn, D. G., *J. Geophys. Res.* **82,** 3889–3911 (1977).

McCartney, M. *J. Mar. Res.* **40, Supplement** 427–464 (1982).

Menzel, S. W., & Ryther, J. H., *Deep-Sea Res.* **15,** 327–338 (1968).

Mix, A. C., & Ruddiman, W. F., *Quat. Sc. Rev.* **4,** 59–108 (1985).

Mullins, H. T., *Geology* **11,** 57–60 (1983).

Mullins, H. T., & Neumann, A. C., in *SEPM Special Publication 27* (eds Doyle, L. J., & Pilkey, O. H.) 165–192 (1979).

Mullins, H. T., Boardman, M. R., & Neumann, A. C., *Mar. Geol.* **32,** 251–268 (1980).

Neumann, A. C., & Land L. S., *J. Sed. Pet.* **45,** 763–786 (1975).

Neumann, A. C., *Bull. Mar. Science* **15,** 987–1035 (1965).

O'Neil, J. R., Clayton, R. N., & Mayeda, T. K., *J. Chem. Phys.* **51,** 5547–5558 (1969).

Oppo, D. W., & Fairbanks, R., *Earth planet. Sci. Lett.* **86,** 1–15 (1987).

Parkin, D.W., & Shackleton, N.J., *Nature* **245,** 455–457 (1973).

Pastouret, L., Chamley, H., Delibrias, G., Duplessy, J. C., & Thiede, J., *Oceanol. Acts* **1,** 217–232 (1978).

Pedlosky, J., *Science* **248,** 316–322 (1990).

Ruddiman, W. S., & McIntyre, A., *Quat. Res.* **3,** 117–130 (1973).

Sarmiento, J. L., *J. Phys. Oceanogr.* **13,** 1924–1939 (1983).

Sarmiento, J. L., Rooth, C. G., & Roether, W., *J. Geophys. Res.* **87,** 8047–8056 (1982).

Sarnthein, M., Thiede, J., Pflaumann, U., Erlenkeuser, H., Futterer, D., Koopmann, B., Lange, H., & Seibold, E., in *Geology of the Northwest African Continental Margin* (eds van Rad, U., Sarnthein, M., & Seibold, E.,) 547–604 (Springer-Verlag, Berlin, 1982).

Schlager, W., & James, N. P., *Sedimentology,* 25, 675–702, 1978.

Shackleton, N. J., in *Fate of Fossil Fuel* CO_2 (eds Andersen, N. R., & Malahoff, A.,) 401–427 (Plenum, New York, 1973).

Shackleton, N. J., & Opdyke, N. D., *Quat. Res.* **3,** 39–55 (1973).

Slowey, N. C., & Curry, W. B., *Nature* **328,** 54–58, (1987).

Spall, M. A., *J. Geophys. Res.* **95,** 9611–9628 (1990).

Spencer, D. W., *Earth planet. Sci. Lett.* **16,** 91–102 (1972).

Stommel, H. *Proc. natn. Acad. Sci. U.S.A.* **76,** 3051–3055 (1979).

Stramma, L., & Siedler, G., *J. Geophys. Res.* **93,** 8111–8118 (1988).

Sundquist, E. T., in *The carbonate cycle and atmospheric* CO_2*: Natural variations from Archean to present* (eds Sundquist, E. T., & Broecker, W. S.) 5–60 (AGU, Washington, D.C., 1985).

Talley, L., & McCartney, M., *J. Phys. Ocean.* **12,** 1189–1205 (1982).

Tsuchiya, M., *J. Mar. Res.* **47**, 747–755 (1989).

van Morkhoven, F. P. C. M., Berggren, W. A., & Edwards, A. S. *Cenozoic Cosmopolitan Deep-water Benthic Foraminifera* (Elf Aquitaine, Pau, 1986).

Wennekens, M. P., *Bull. Mar. Science* **9**, 1–52 (1959).

Worthington, V., *Johns Hopkins Oceanographic Studies* **VI**, (Johns Hopkins University Press, Baltimore and London, 1976)

Woods, J. D., in *Coupled-Ocean Atmosphere Models* (ed Nihoul, J. C. J.,) 543–590 (Elsevier, Amsterdam, 1985).

Wust, G., *The Stratosphere of the Atlantic Ocean* (english translation ed Emery, W.,) (original german edition published in 1935) (Amerind Publishing Co. Pvt. Ltd., New Delhi, 1978).

Zahn, R., & Mix, A. C., *Paleoceanography* (submitted).

Zahn, R., Sarnthein, M., & Erlenkeuser, H., *Paleoceanography* **2**, 543–559 (1987).

3.10 Figure captions

Figure 1. The geographic setting of Little and Great Bahama Banks. Hatched area indicates location of study site.

Figure 2. Bathymetry of study site in meters (after NOAA SE United States regional map). Open symbols indicate locations of sediment cores utilized in this study and listed in Table 1 (circles = piston and gravity cores, boxes = box cores).

Figure 3. Aragonite content (open circles) and $\delta^{18}O$ of planktonic foraminifera (dots) versus depth in the upper 260 cm of piston and gravity cores. High aragonite and low $\delta^{18}O$ at the core tops indicate they are recent Holocene in age while low aragonite and high $\delta^{18}O$ indicate glacial-aged sediments. Benthic foraminifera were picked from core tops and sediments deposited during the last glacial maximum (stippling).

Figure 4. Comparison of the isotopic compositions of *P. wuellerstorfi* and *P. ariminensis* found in the same sediment samples (filled circles = Zahn et al., 1988; open circles = this study). Both species have essentially the same $\delta^{13}C$ values and the difference in the mean compositions of $\delta^{18}O$ is quite small. Therefore, no corrections are applied to *P. ariminensis* isotope values before comparing them to those of *P. wuellerstorfi*.

Figure 5. The concentration of phosphate in seawater near the Little Bahama Bank (AT109 station 137 [Roemmich and Wunsch, 1985]), the estimated $\delta^{13}C$ of the dissolved inorganic carbon in seawater (dashed line) and the average $\delta^{13}C$ of recent Holocene (open symbols) and glacial-aged (filled symbols) foraminifera from the margin of Little and Great Bahama Banks (box = *P. foveolata*, circle = *P. ariminensis*, triangle = *P. wuellerstorfi*. Bars indicate the standard error of averaged values. Modern phosphate concentrations reach maximum values and recent Holocene $\delta^{13}C$ reach mimimum values at about 800 m water depth. Glacial $\delta^{13}C$ values are more positive than recent Holocene values and do not possess a local mimimum.

Figure 6. Bathymetric profile of water temperature near Little Bahama Bank (OC205-2 station 93, Chapter 1) and the $\delta^{18}O$ of benthic foraminifera (see Fig. 7). Foraminiferal $\delta^{18}O$ displays a steep gradient with depth that results primarily from the characteristic temperature gradient of thermocline waters. The bathymetric gradient of recent Holocene foraminifera corresponds closely to that of equilibrium calcite (dashed line). Symbols are the same as Fig. 5. During the last glacial maximum, values are more positive and the gradient was steeper than during the recent Holocene.

Figure 7. Qualitative comparison of the $\delta^{18}O$ of recent benthic foraminifera and the expected equilibrium values (offset by -1.0 per mil) based upon the equations of (a) Erez and Luz [1983], (b) O'Neil et al. [1969] and (c) Craig's [1965] modification of Epstein et al. [1953].

Figure 8. A "mixing" diagram for glacial foraminiferal $\delta^{18}O$ and $\delta^{13}C$. End members are

identified and usually correspond to circles (see text, and Oppo and Fairbanks [1987] for description).

Figure 9. Schematic illustration of data in Fig. 8 and 10. (a) NAIW falls within the $\delta^{13}C$–$\delta^{18}O$ mixing field of wNASW, southern component water and Mediterranean water; however, (b) NAIW does not fall within the Ba/Ca–$\delta^{18}O$ mixing field of these components and so is not a mixture of all of them. (c) NAIW falls on the edge of the mixing field between wNASW, southern and northern component waters, indicating little contribution by southern waters. (d) NAIW falls on the edge of the mixing field between wNASW, Mediterranean and northern component waters, indicating little contribution by Mediterranean waters. (e) If the end member for northern component water is different than above, some contribution of southern water to NAIW is possible. However, no contribution of Mediterranean water to NAIW is possible.

Figure 10. "Mixing" diagrams for (a) glacial foraminiferal Ba/Ca and $\delta^{13}C$, and (b) glacial foraminiferal Ba/Ca and $\delta^{18}O$. Symbols are as in Fig. 8.

3.11 Figures

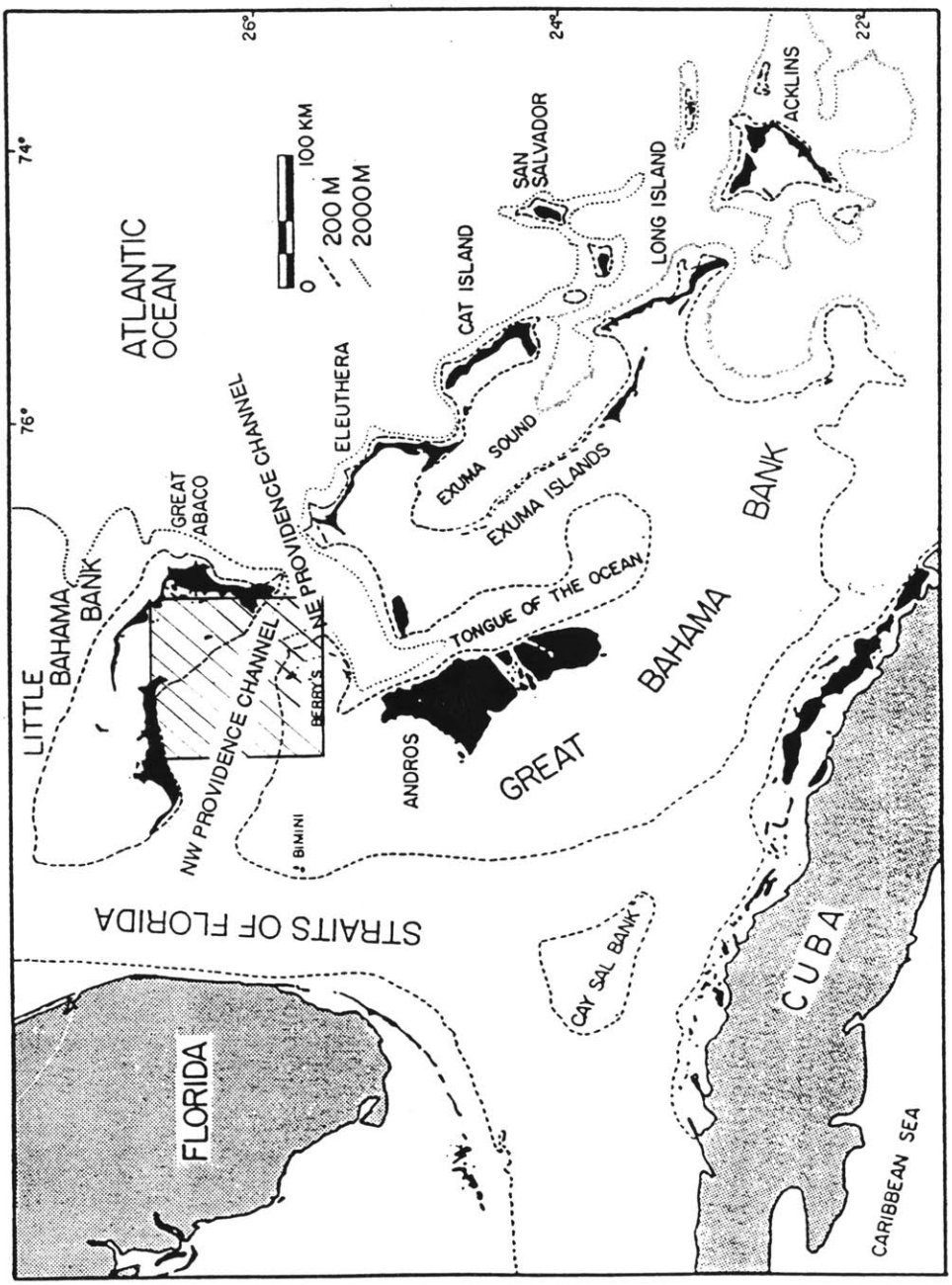
ATLANTIC OCEAN
LITTLE BAHAMA BANK
GREAT ABACO
NW PROVIDENCE CHANNEL
NE PROVIDENCE CHANNEL
PERRY'S
BIMINI
ELEUTHERA
CAT ISLAND
SAN SALVADOR
LONG ISLAND
ACKLINS
EXUMA SOUND
EXUMA ISLANDS
TONGUE OF THE OCEAN
ANDROS
GREAT BAHAMA BANK
STRAITS OF FLORIDA
FLORIDA
CAY SAL BANK
CUBA
CARIBBEAN SEA
0
100 KM
200 M
2000M
74°
76°
26°
24°
22°

Figure 1.

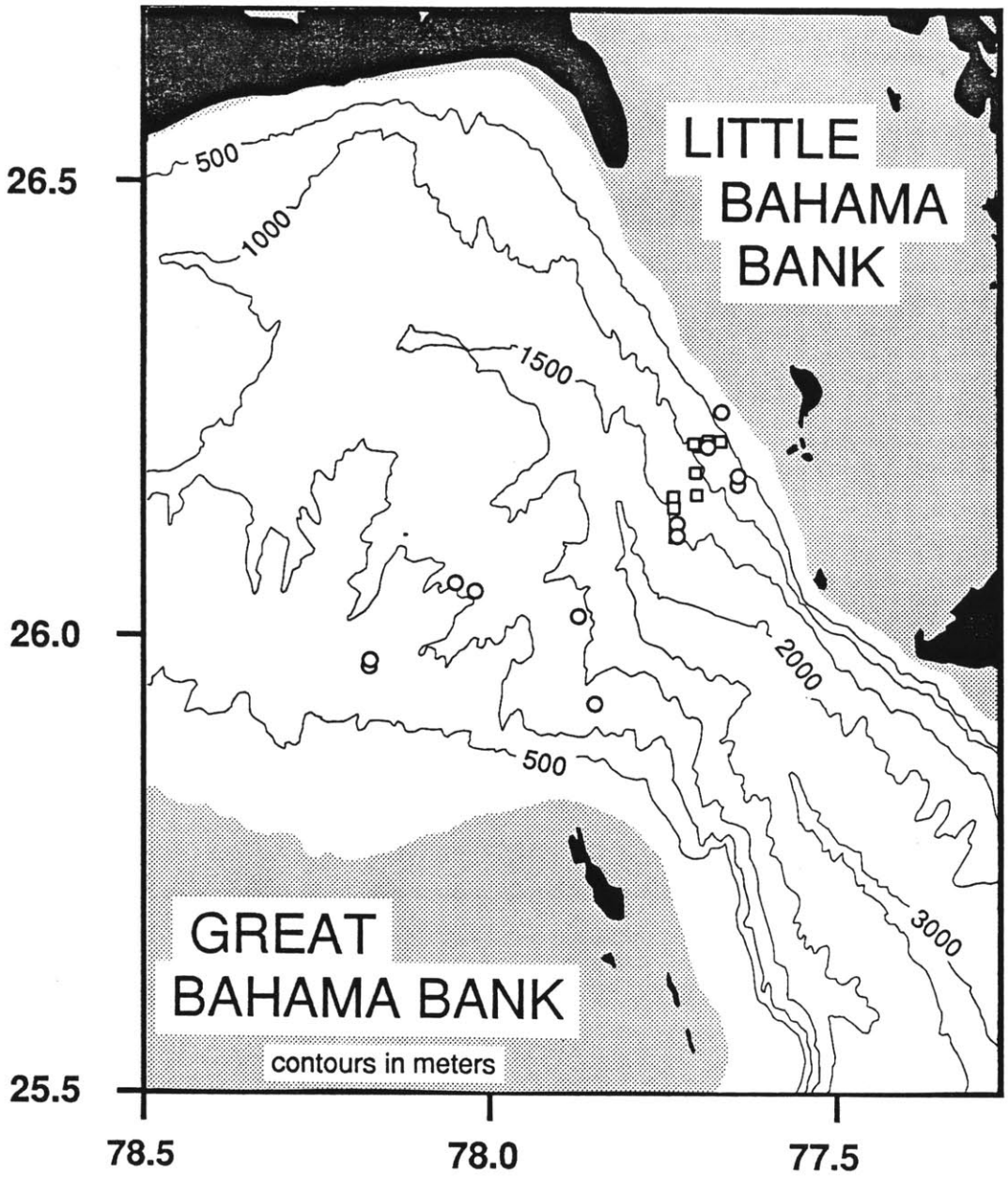
LITTLE
BAHAMA
BANK
GREAT
BAHAMA BANK
contours in meters
500
1000
1500
2000
500
3000
26.5
26.0
25.5
78.5
78.0
77.5

Figure 2.

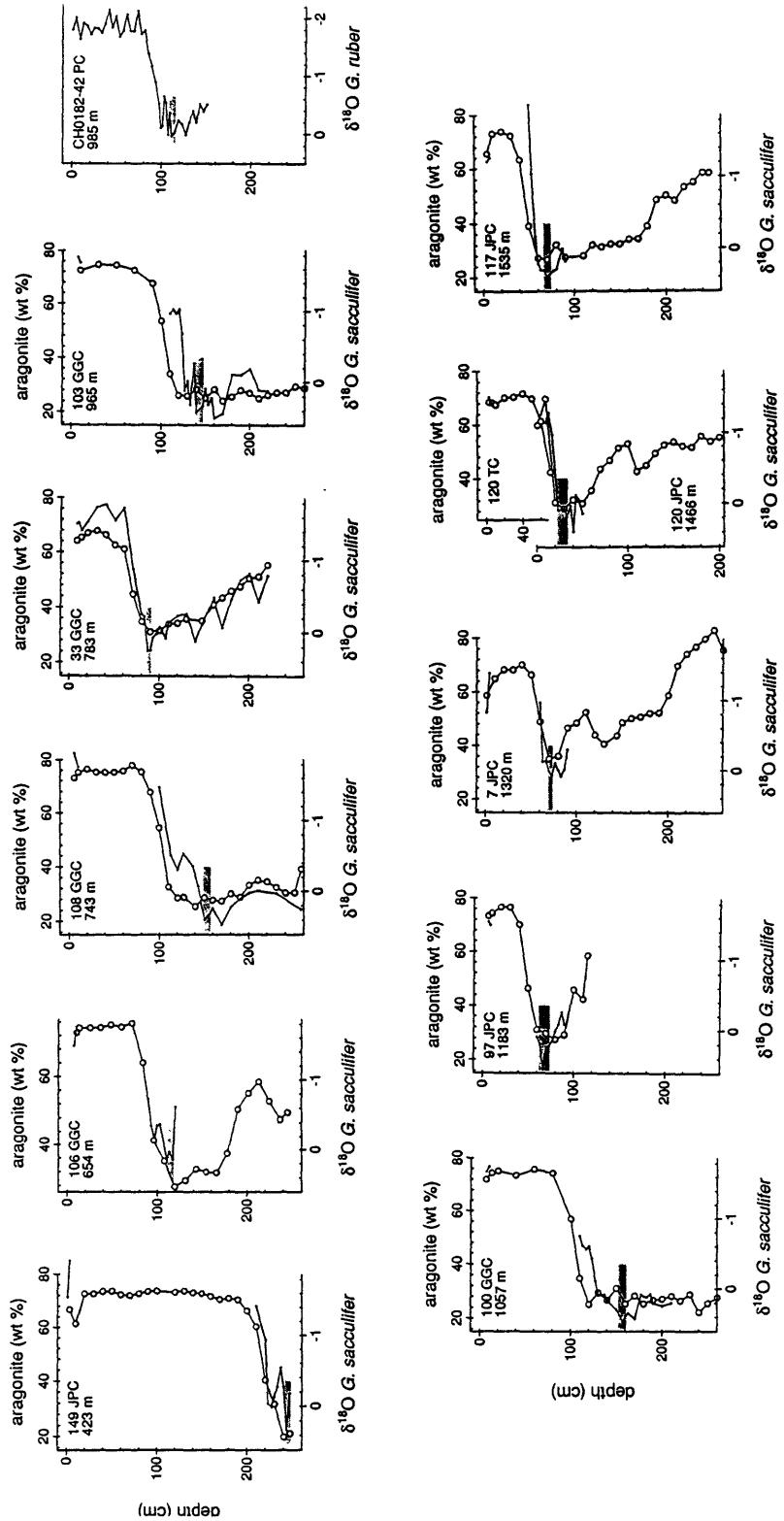
aragonite (wt %)
δ18O G. sacculifer
δ18O G. ruber
depth (cm)
149 JPC
423 m
106 GGC
654 m
108 GGC
743 m
33 GGC
783 m
103 GGC
965 m
CH0182-42 PC
985 m
100 GGC
1057 m
97 JPC
1183 m
7 JPC
1320 m
120 TC
120 JPC
1466 m
117 JPC
1535 m

Figure 3.

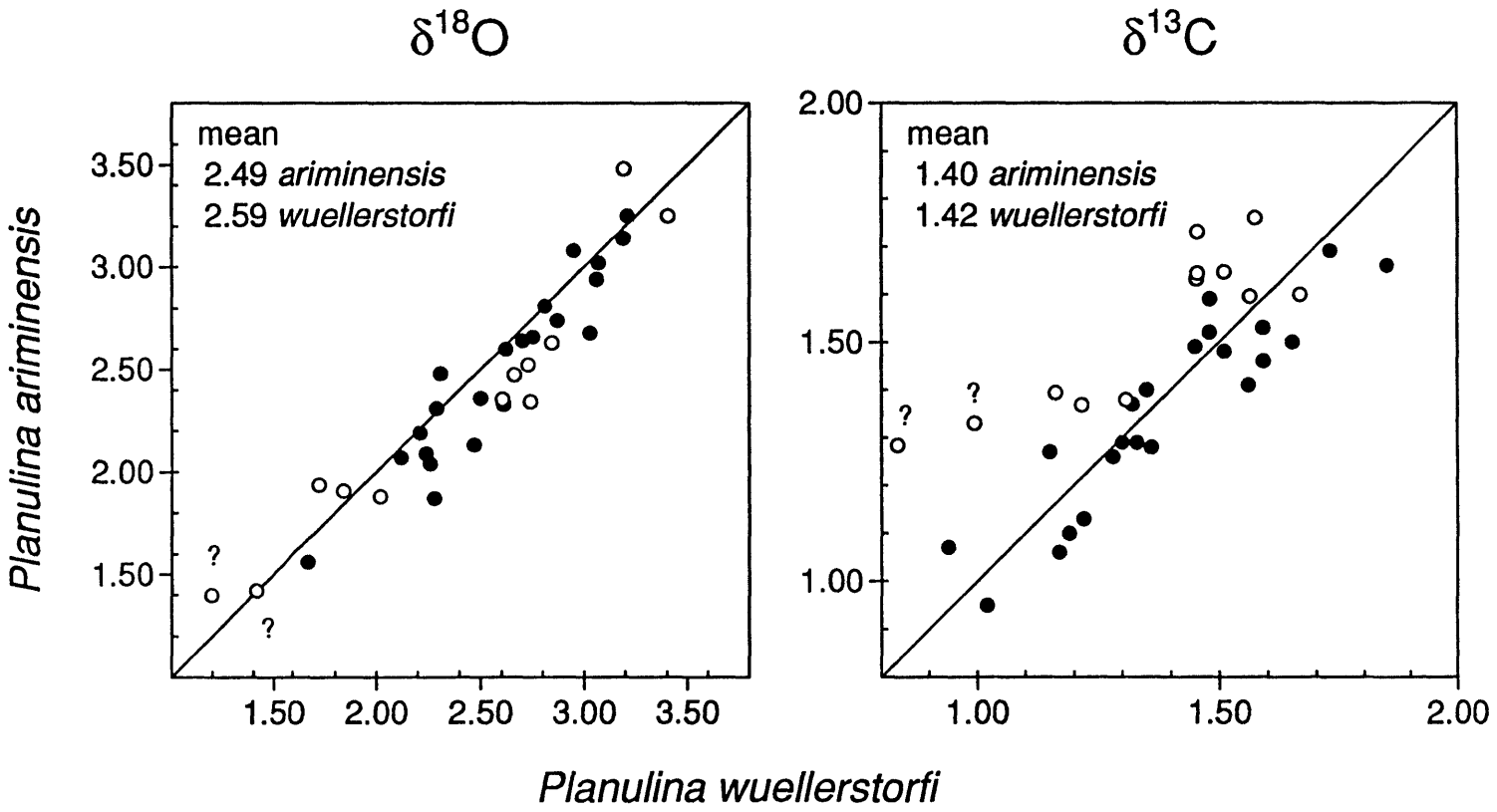
δ18O
δ13C
mean
2.49 ariminensis
2.59 wuellerstorfi
mean
1.40 ariminensis
1.42 wuellerstorfi
Planulina ariminensis
Planulina wuellerstorfi
3.50
3.00
2.50
2.00
1.50
2.00
1.50
1.00
1.50
2.00
2.50
3.00
3.50
1.00
1.50
2.00
?
?
?
?

Figure 4.

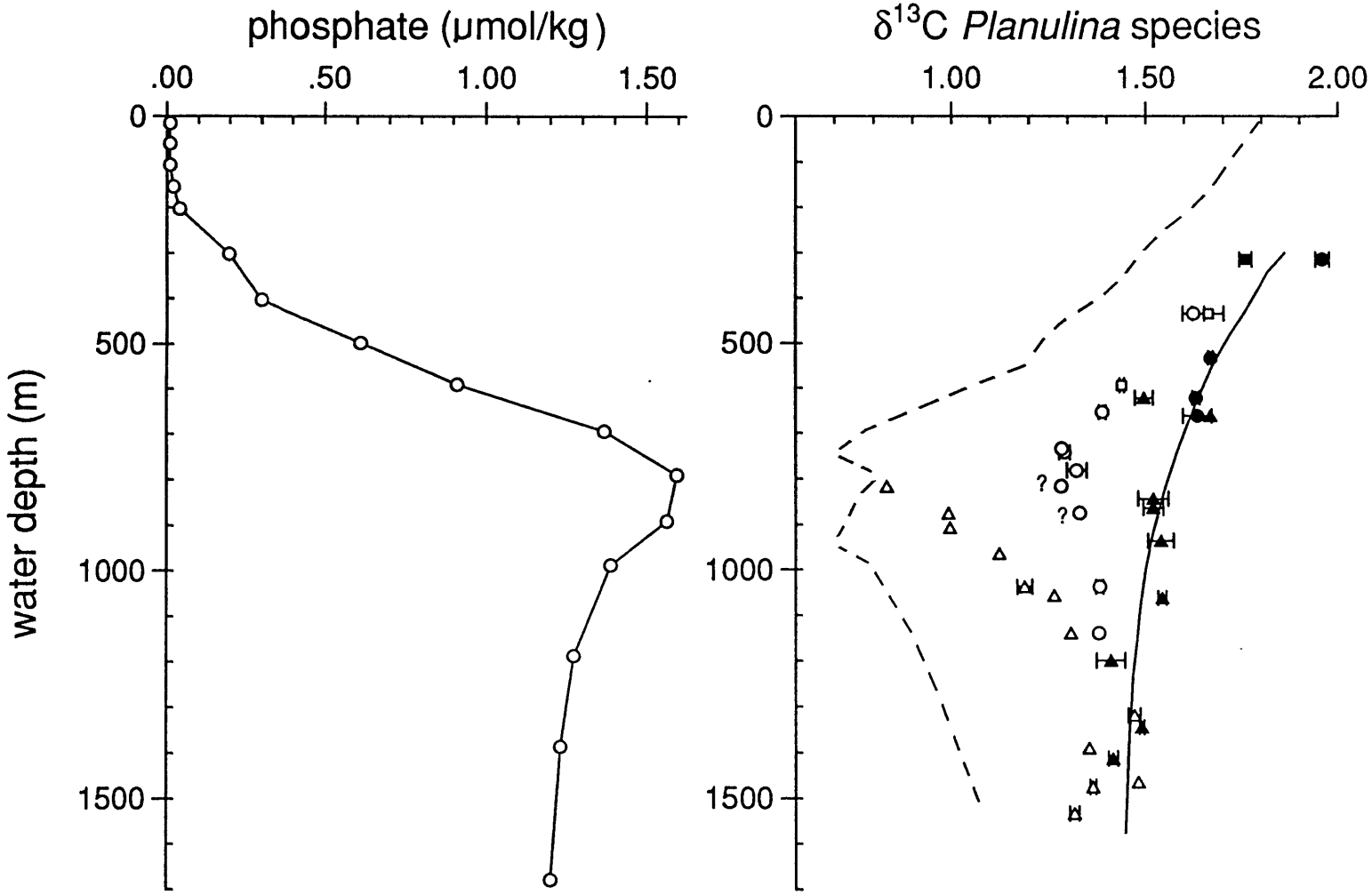
phosphate (µmol/kg)
.00
.50
1.00
1.50
δ13C Planulina species
1.00
1.50
2.00
water depth (m)
0
500
1000
1500
?
?

Figure 5.

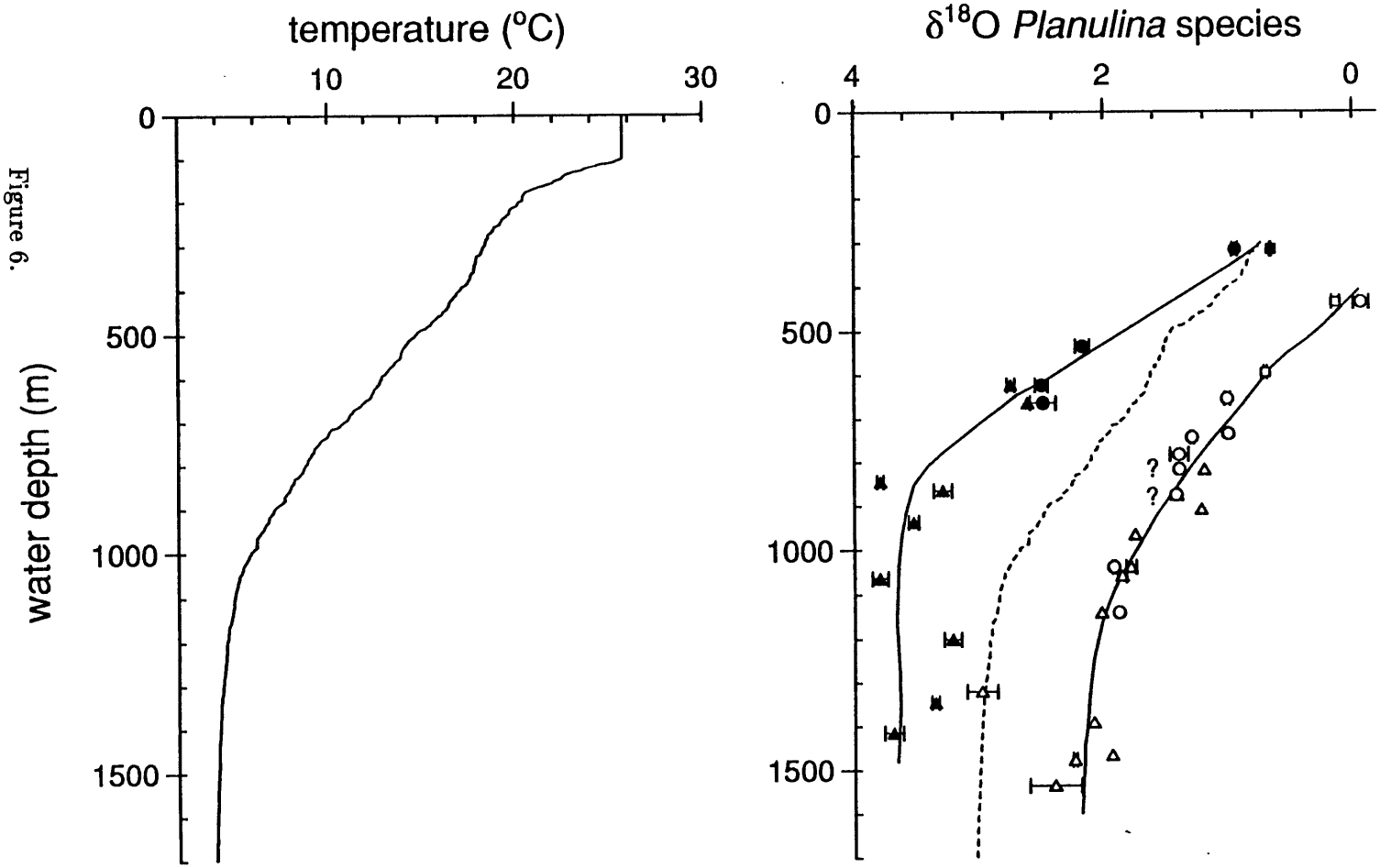
temperature (°C)
10
20
30
0
500
1000
1500
water depth (m)
δ18O Planulina species
4
2
0
0
500
1000
1500
?
?

Figure 6.

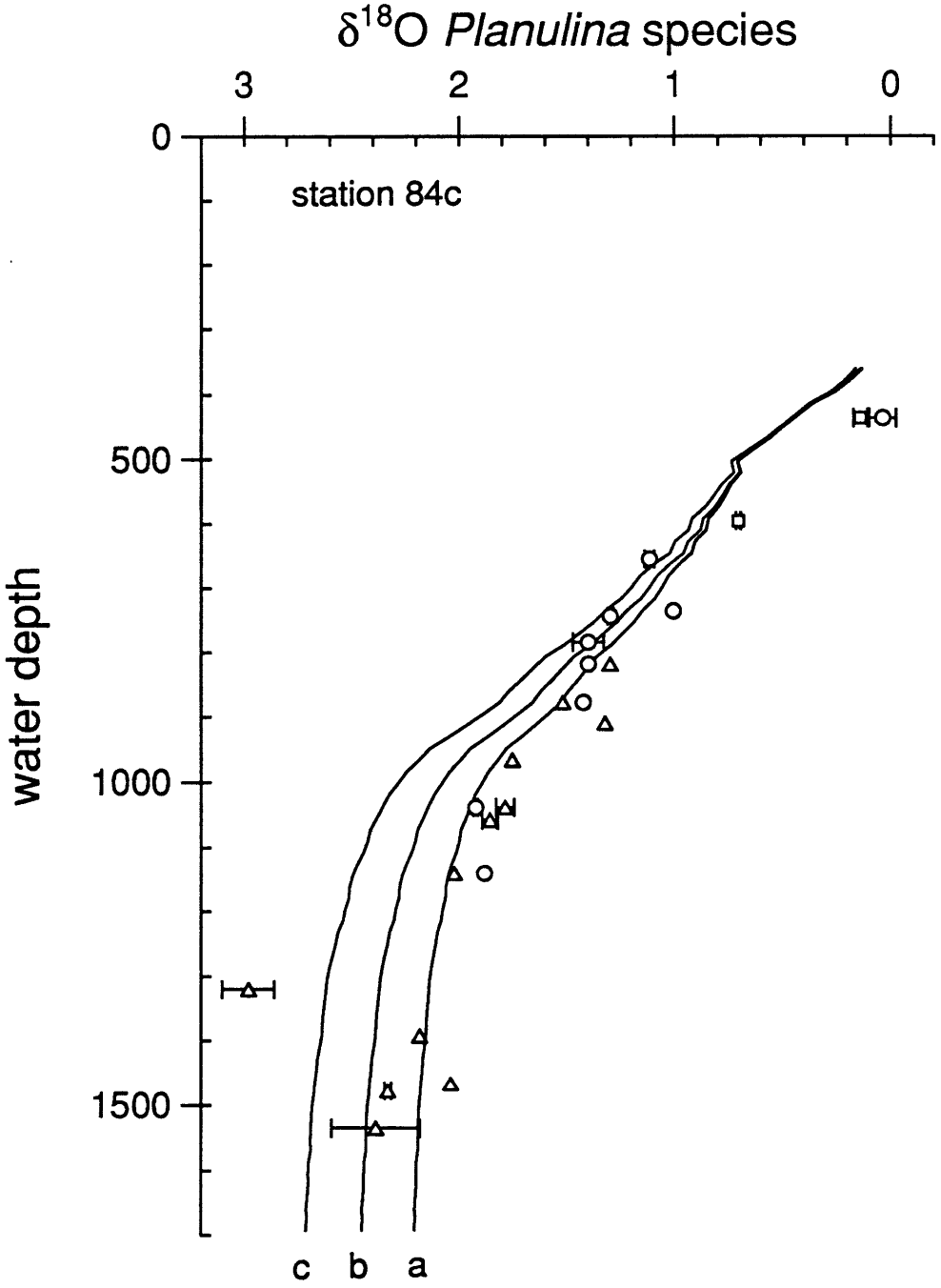
δ18O Planulina species
3
2
1
0
0
station 84c
500
1000
1500
water depth
c
b
a

Figure 7.

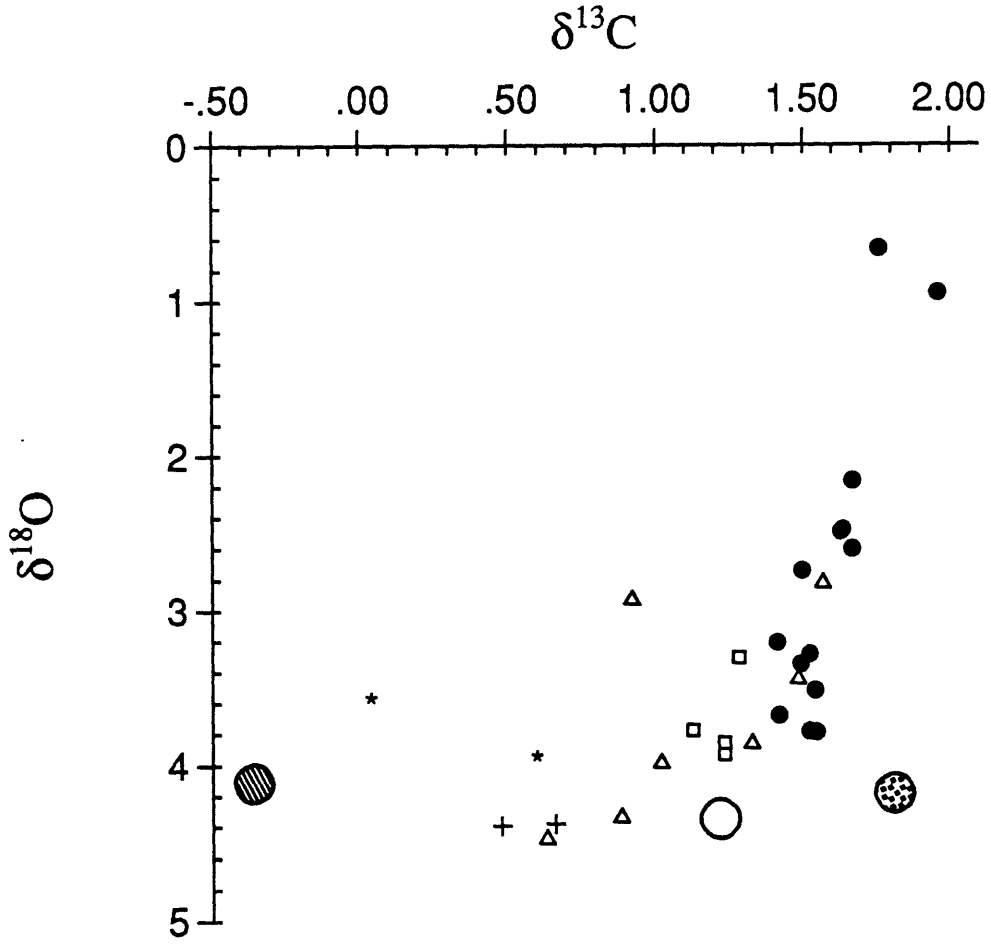

- this study
- △ Zahn et al. (1988)
- □ Caribbean and intermediate -depth North Atlantic
  (Boyle and Keigwin, 1987)
  (Oppo and Fairbanks, 1987)
- \+ deep Atlantic (Boyle and Keigwin, 1982, 1987)
- ✱ intermediate-depth South Atlantic (Pastouret, 1978; Curry et al., 1988)
- ○ northern deep Atlantic end member (Curry et al., 1988)
- Mediterrenean end member (Oppo and Fairbanks, 1987)
- southern end member (Oppo and Fairbanks, 1987)

Figure 8.

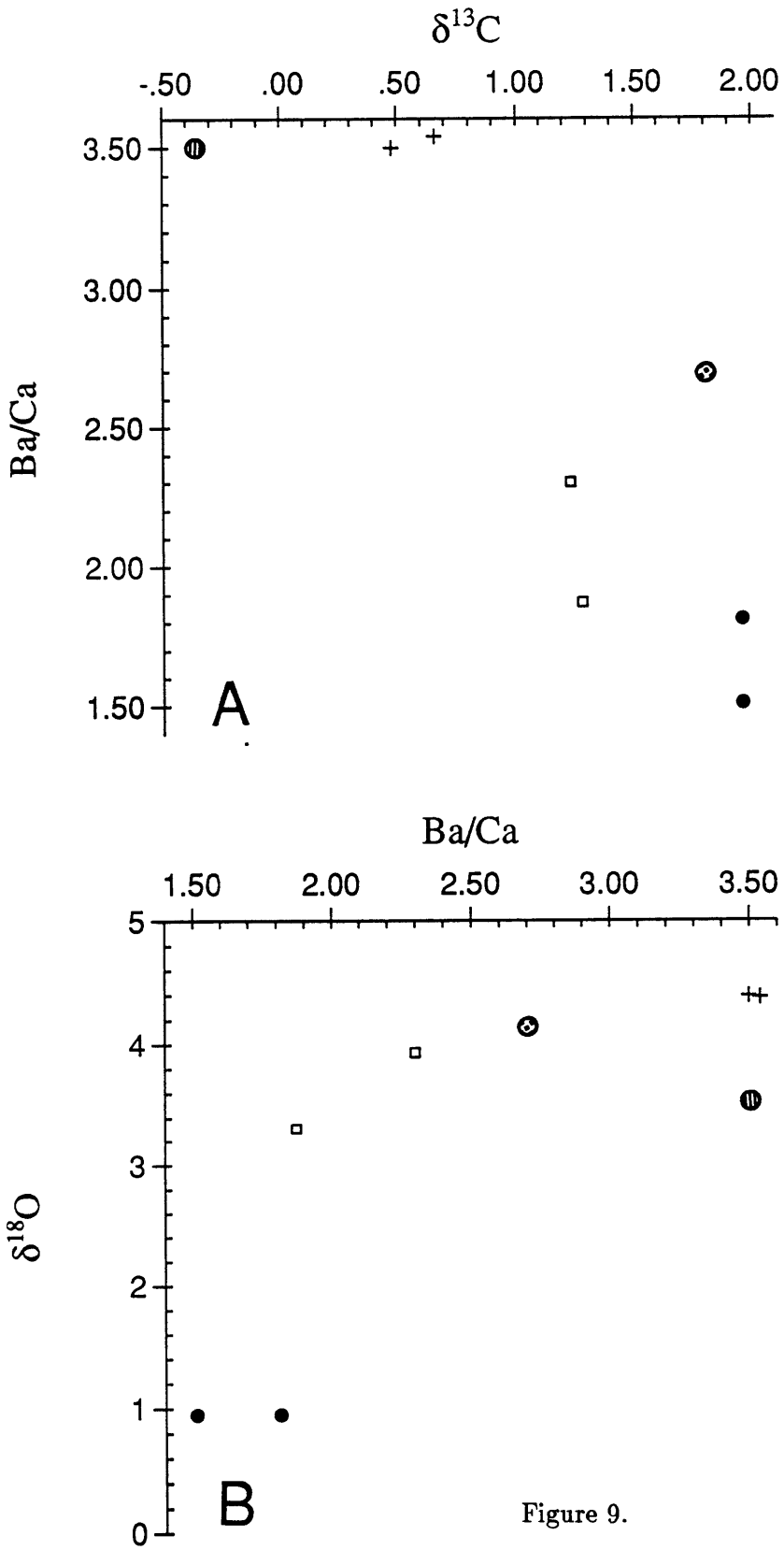
δ13C
-.50
.00
.50
1.00
1.50
2.00
3.50
3.00
2.50
2.00
1.50
Ba/Ca
A
Ba/Ca
1.50
2.00
2.50
3.00
3.50
5
4
3
2
1
0
δ18O
B

Figure 9.

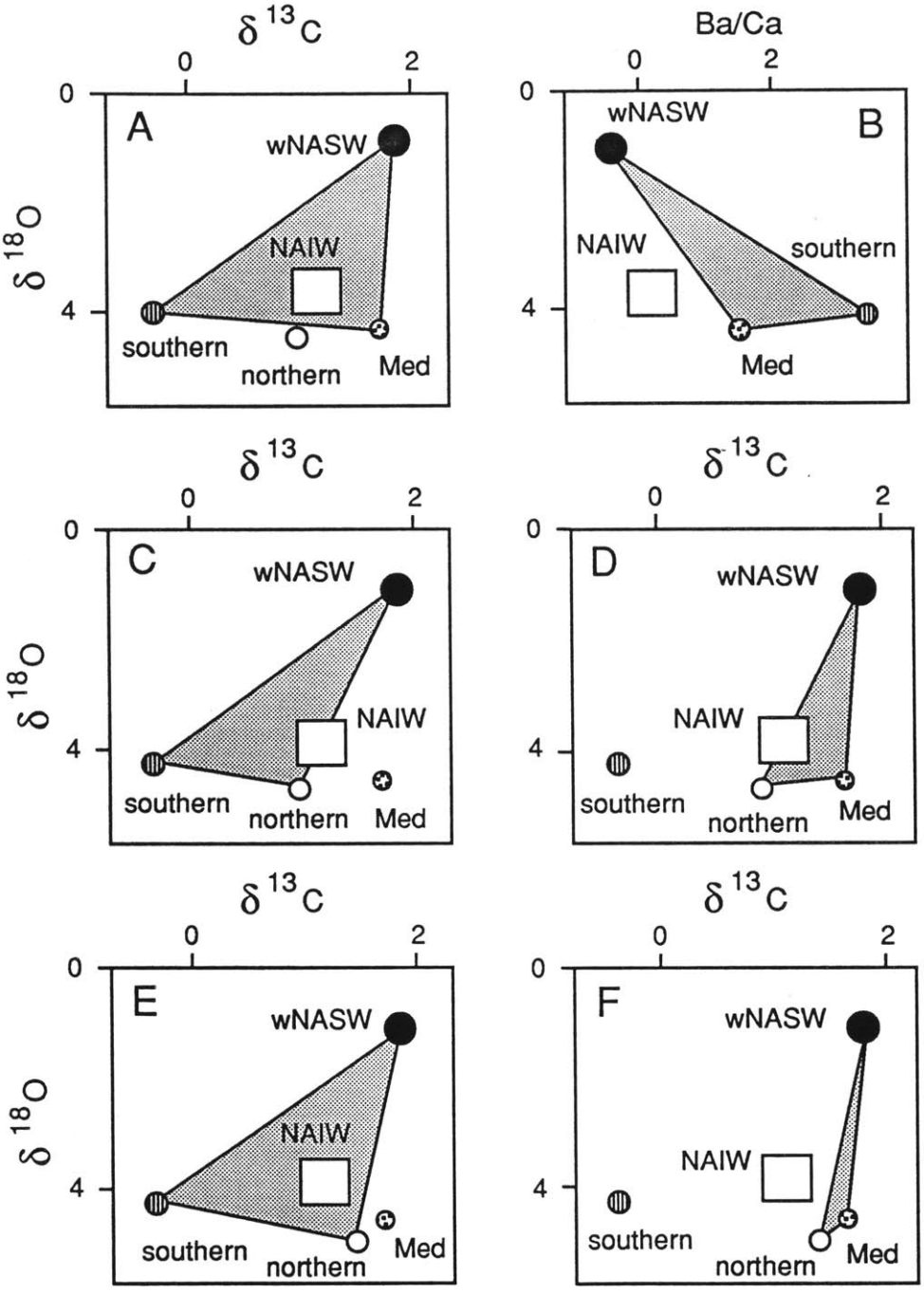
δ 13C
Ba/Ca
δ 18O
0
2
4
A
B
C
D
E
F
wNASW
NAIW
southern
northern
Med
KEY:
NAIW = North Atlantic Intermediate Water
wNASW = wintertime North Atlantic surface water
southern = southern source deep waters
northern = North Atlantic deep waters
Med = Mediterranean Intermediate Water

Figure 10.

3.12 Tables

These tables contain the following: (1) the location and depth of cores utilized in this study, (2) the percentage of aragonite relative to total aragonite and calcite in bulk sediment from the cores, (3) the isotopic compositions of planktonic foraminifera (*Globigerinoides* species) from the cores, and (4) the isotopic compositions of benthic foraminifera (*Planulina* species) from the recent Holocene and last glacial Maximum.

CORE	LATITUDE (deg)	LONGITUDE (deg)	DEPTH (m)
OC205-2-50BC	26.2247 N	77.6968 W	800
OC205-2-53BC	26.1928 N	77.7092 W	1020
OC205-2-55BC	26.1685 N	77.7075 W	1125
OC205-2-59BC	26.1663 N	77.7408 W	1468
OC205-2-67BC	26.1542 N	77.7400 W	1380
OC205-2-69BC	26.2282 N	77.6915 W	720
OC205-2-70BC	26.2225 N	77.7027 W	865
OC205-2-72BC	26.2248 N	77.7118 W	886
OC205-2-74BC	26.2272 N	77.6728 W	595
OC205-2-7JPC	26.1365 N	77.7353 W	1310
OC205-2-33GGC	26.2210 N	77.6912 W	770
OC205-2-97JPC	25.9368 N	77.8537 W	1172
OC205-2-100GGC	26.0612 N	78.0277 W	1045
OC205-2-103GGC	26.0703 N	78.0562 W	950
OC205-2-106GGC	25.9767 N	78.1810 W	640
OC205-2-108GGC	25.9838 N	78.1797 W	730
OC205-2-117JPC	26.0335 N	77.8778 W	1520
OC205-2-120JPC	26.1230 N	77.7350 W	1455
OC205-2-120TC	26.1230 N	77.7350 W	1455
OC205-2-149JPC	26.2595 N	77.6715 W	423
CH0182-42PC	26.1895 N	77.6470 W	985

Core: OC205-2 7JPC

bulk sediment depth (cm)	aragonite (wt %)
1.0	58.6
10.0	65.0
20.0	68.3
30.0	68.2
40.0	70.2
50.0	66.4
60.0	48.8
70.0	35.1
80.0	36.0
90.0	46.5
100.0	48.5
110.0	52.4
120.0	43.9
130.0	40.6
144.0	43.7
150.0	48.6
160.0	50.2
170.0	50.7
180.0	52.1
190.0	52.3
200.0	58.8
210.0	69.9
220.0	74.3
230.0	76.9
240.0	79.9
250.0	83.1
260.0	75.7
270.0	59.5
280.0	35.1
287.0	37.0
291.0	38.9
300.0	47.6
310.0	50.9
320.0	54.4
330.0	64.9
340.0	64.5
350.0	43.8
360.0	46.9
370.0	53.4
380.0	67.6
390.0	72.8
400.0	71.8
410.0	60.9
420.0	42.9
430.0	49.4
440.0	54.9
447.0	58.9

G. sacculifer (300-350 microns)

depth (cm)	O-18 (PDB)	C-13 (PDB)
1.0	-.82	.96
4.0	-1.38	1.22
60.0	-.96	1.23
63.0	-.12	1.58
67.0	-.13	1.33
70.0	.02	1.52
73.0	.08	1.44
77.0	-.10	1.40
80.0	.00	1.39
83.0	.09	1.20
87.0	-.01	1.50
90.0	-.29	1.47

Core: OC205-2 33GGC

bulk sediment	
depth (cm)	aragonite (wt %)
8.0	64.1
13.0	65.4
20.0	67.0
30.0	67.8
40.0	66.3
50.0	62.5
60.0	61.0
70.0	44.7
80.0	34.7
90.0	30.9
100.0	31.5
110.0	33.9
120.0	34.1
130.0	35.8
147.0	35.0
160.0	41.0
170.0	43.5
180.0	45.9
190.0	47.5
200.0	50.4
210.0	51.0
220.0	55.4

G. sacculifer (300-350 microns)		
depth (cm)	O-18 (PDB)	C-13 (PDB)
8.0	-1.57	1.02
8.0	-1.45	1.20
10.0	-1.53	1.11
13.0	-1.42	1.34
20.0	-1.55	1.30
30.0	-1.74	1.22
40.0	-1.78	.88
50.0	-1.56	1.34
60.0	-1.73	1.20
70.0	-.88	1.32
80.0	-.26	1.17
83.0	.03	1.26
83.0	-.48	1.11
87.0	.25	1.61
87.0	.24	1.53
90.0	.25	1.54
93.0	.33	1.37
93.0	-.20	1.61
97.0	.07	1.61
97.0	-.04	1.81
100.0	-.08	1.36
103.0	-.02	1.26
107.0	.08	1.59
110.0	-.14	1.49
120.0	-.23	1.36
130.0	-.26	1.10
140.0	.12	1.39
147.0	-.11	.55
160.0	-.49	1.31
170.0	-.07	1.54
180.0	-.46	1.65
190.0	-.73	1.17
200.0	-.82	1.62
210.0	-.43	1.21
220.0	-.79	1.13

Core: OC205-2 97JPC

bulk sediment depth (cm)	aragonite (wt %)
6.0	73.3
10.0	74.3
20.0	76.6
30.0	76.5
40.0	70.1
50.0	46.4
60.0	31.0
70.0	29.6
80.0	27.4
90.0	29.1
100.0	45.9
110.0	42.3
115.0	58.5

G. sacculifer (300-350 microns) depth (cm)	O-18 (PDB)	C-13 (PDB)
6.0	-1.54	1.48
8.0	-1.49	1.35
60.0	.09	1.56
63.0	.19	1.55
67.0	.55	1.47
70.0	.23	1.62
73.0	.22	1.71
77.0	.14	1.76
80.0	.02	1.77
83.0	-.08	1.87
87.0	-.25	1.56
90.0	-.08	1.27

Core: OC205-2 100GGC

bulk sediment depth (cm)	aragonite (wt %)
7.0	71.8
13.0	74.2
20.0	75.0
40.0	73.3
60.0	75.6
80.0	74.2
100.0	56.8
110.0	34.7
120.0	25.0
130.0	29.4
140.0	26.6
150.0	30.9
160.0	25.3
170.0	28.2
180.0	25.2
190.0	26.6
200.0	27.0
210.0	28.0
220.0	26.4
230.0	28.7
240.0	22.1
250.0	25.5
260.0	27.6
280.0	41.3

G. sacculifer (300-350 microns) depth (cm)	O-18 (PDB)	C-13 (PDB)
7.0	-1.68	1.11
10.0	-1.75	1.16
110.0	-.75	1.48
113.0	-.61	1.07
117.0	-.56	1.43
120.0	-.60	1.08
123.0	-.43	1.08
127.0	-.11	1.32
130.0	.09	1.30
133.0	.08	1.43
137.0	.08	1.39
140.0	.16	1.54
150.0	.21	1.68
150.0	.44	1.33
150.0	.21	1.71
153.0	.37	1.35
157.0	.47	1.52
160.0	.44	1.53
160.0	.33	1.87
163.0	.34	1.47
170.0	.42	1.86
177.0	.08	1.72
180.0	.27	1.79
180.0	-.06	1.24
183.0	.12	1.50
187.0	.07	1.38
190.0	.20	1.63
200.0	.24	1.26
210.0	.20	1.76

Core: OC205-2 103GGC

bulk sediment depth (cm)	aragonite (wt %)
10.0	72.5
30.0	74.6
50.0	74.4
70.0	72.5
90.0	67.5
100.0	53.4
110.0	33.9
120.0	25.9
130.0	25.8
140.0	28.1
150.0	24.9
160.0	28.2
170.0	23.9
180.0	25.4
190.0	27.9
200.0	26.8
210.0	24.8
220.0	26.1
230.0	27.0
240.0	27.0
250.0	29.3
260.0	28.6
270.0	26.0
280.0	26.8

G. sacculifer (300-350 microns) depth (cm)	O-18 (PDB)	C-13 (PDB)
8.0	-1.78	1.19
10.0	-1.70	.96
110.0	-.97	1.31
113.0	-1.03	.93
117.0	-.86	1.06
117.0	-1.07	1.15
120.0	-1.05	1.02
120.0	-1.01	1.02
123.0	-.98	1.46
123.0	-.39	1.33
127.0	.12	1.56
127.0	.09	1.32
130.0	.10	1.41
130.0	-.14	1.23
130.0	-.03	1.38
133.0	.29	1.58
133.0	.32	1.48
137.0	-.41	1.53
137.0	-.13	1.35
140.0	.51	1.71
140.0	.33	1.44
147.0	.34	1.50
147.0	.32	1.49
150.0	.18	1.46
150.0	-.01	1.55
153.0	.41	1.57
153.0	.21	1.62
157.0	.30	1.57
157.0	.14	1.65
160.0	.57	1.73
160.0	.44	1.92
170.0	.82	2.13
170.0	.07	1.77
180.0	-.11	1.49
190.0	-.11	1.45
200.0	-.19	1.53
210.0	.11	1.47
220.0	.12	1.32

Core: OC205-2 106GGC

bulk sediment	
depth (cm)	aragonite (wt %)
7.0	72.8
10.0	74.3
20.0	74.3
30.0	74.3
40.0	75.2
50.0	74.5
60.0	75.6
70.0	64.0
80.0	41.2
90.0	35.1
100.0	27.5
110.0	29.4
120.0	32.7
130.0	31.8
140.0	31.7
150.0	37.3
160.0	50.4
170.0	55.0
180.0	58.3
190.0	52.7
200.0	47.4
207.0	49.5

G. sacculifer (300-350 microns)		
depth (cm)	O-18 (PDB)	C-13 (PDB)
7.0	-1.49	1.36
10.0	-1.76	.85
90.0	-.73	1.24
93.0	-.36	1.26
97.0	-.18	1.44
100.0	-.37	1.42
103.0	-.39	1.25
110.0	.13	1.62
113.0	.03	1.26
117.0	.14	1.37
120.0	-.62	1.38

Core: OC205-2 108GGC

bulk sediment		G. sacculifer (300-350 microns)		
depth (cm)	aragonite (wt %)	depth (cm)	O-18 (PDB)	C-13 (PDB)
6.0	73.0	6.0	-1.97	.85
10.0	75.1	10.0	-1.77	.36
20.0	76.4	100.0	-1.48	.66
30.0	75.2	113.0	-.07	1.00
40.0	75.1	113.0	-.96	1.13
50.0	75.2	120.0	.19	1.38
60.0	75.6	120.0	-.82	1.06
70.0	77.8	127.0	-.40	.96
80.0	75.3	127.0	-.67	1.08
90.0	67.6	137.0	-.43	1.24
100.0	54.4	137.0	-.29	1.24
110.0	32.5	143.0	-.17	1.27
120.0	28.4	143.0	.01	1.36
127.0	28.7	150.0	.62	1.30
140.0	25.3	150.0	.16	1.38
150.0	28.5	157.0	.43	1.62
160.0	27.7	157.0	.15	1.80
170.0	27.3	160.0	.26	1.29
180.0	29.9	160.0	.20	1.39
190.0	28.7	170.0	.46	1.59
200.0	33.1	180.0	.22	1.43
210.0	34.9	190.0	.10	1.43
220.0	34.4	200.0	.02	1.42
230.0	32.2	210.0	-.01	1.51
240.0	30.2	230.0	.03	1.26
250.0	30.3	257.0	.25	1.50
257.0	39.0			

Core: OC205-2 117JPC

bulk sediment depth (cm)	aragonite (wt %)
4.0	65.6
10.0	73.0
20.0	73.9
30.0	72.2
40.0	63.2
50.0	39.1
60.0	27.2
70.0	26.8
80.0	32.1
90.0	27.4
110.0	28.0
120.0	31.9
130.0	31.3
140.0	32.3
150.0	32.2
160.0	34.1
170.0	34.2
180.0	38.8
190.0	48.4
200.0	50.0
210.0	48.1
220.0	53.0
230.0	54.7
240.0	58.2
247.0	58.1

G. sacculifer (300-350 microns)

depth (cm)	O-18 (PDB)	C-13 (PDB)
4.0	-1.22	1.14
7.0	-1.27	.85
50.0	-2.02	-2.04
53.0	-1.04	.07
57.0	-.17	.86
60.0	.22	1.05
63.0	.30	1.43
67.0	.31	1.46
70.0	.40	1.59
73.0	.36	1.74
77.0	.31	1.54
80.0	.29	1.52
83.0	.15	1.64
87.0	.01	1.71
90.0	.18	1.51

Core: OC205-2 120TC

bulk sediment depth (cm)	aragonite (wt %)
3.0	68.5
7.0	68.3
10.0	67.6
20.0	70.2
30.0	70.4
40.0	71.7
50.0	69.7
60.0	61.3
70.0	42.3

G. sacculifer (300-350 microns)

depth (cm)	O-18 (PDB)	C-13 (PDB)
3.0	-1.51	1.31
7.0	-1.39	1.76

Core: OC205-2 120JPC

bulk sediment		G. sacculifer (300-350 microns)		
depth (cm)	aragonite (wt %)	depth (cm)	O-18 (PDB)	C-13 (PDB)
1.0	59.8	10.0	-1.15	1.45
10.0	69.6	13.0	-1.29	1.06
20.0	31.2	17.0	-.97	1.22
30.0	28.8	20.0	-.48	1.60
40.0	32.2	23.0	.09	1.76
50.0	30.8	27.0	.08	1.57
60.0	35.5	30.0	.07	1.59
70.0	43.4	33.0	.18	1.61
80.0	46.6	37.0	.03	1.56
90.0	51.1	40.0	.38	1.61
100.0	52.8	43.0	-.12	1.86
110.0	42.4	46.0	-.06	1.57
120.0	44.6	50.0	.14	1.28
130.0	49.1			
140.0	52.2			
150.0	53.3			
160.0	51.7			
170.0	51.2			
180.0	55.5			
190.0	53.5			
200.0	55.0			
210.0	59.2			
220.0	66.5			
230.0	71.3			
240.0	73.3			
250.0	75.6			
260.0	79.4			
270.0	81.5			
280.0	82.4			
290.0	77.3			
300.0	64.0			
310.0	28.7			
320.0	28.0			
330.0	30.2			

Core: OC205-2 149JPC

bulk sediment depth (cm)	aragonite (wt %)
3.0	66.6
10.0	61.2
20.0	72.6
30.0	72.5
40.0	73.4
50.0	73.6
60.0	72.2
70.0	71.9
80.0	72.7
90.0	73.5
100.0	73.7
120.0	73.2
130.0	73.7
140.0	73.0
150.0	72.7
160.0	71.7
170.0	70.5
180.0	70.9
190.0	70.4
200.0	66.2
210.0	60.2
220.0	40.4
230.0	31.6
240.0	19.7
247.0	21.0

G. sacculifer (300-350 microns)

depth (cm)	O-18 (PDB)	C-13 (PDB)
1.0	-1.55	1.54
3.0	-2.07	.65
210.0	-1.38	.65
210.0	-1.47	1.15
220.0	-.94	.99
223.0	-.04	1.35
227.0	.01	1.62
230.0	-.32	1.37
230.0	.07	1.44
233.0	-.27	1.60
237.0	-.54	1.46
240.0	-.27	1.26
243.0	.32	1.48
247.0	-.18	1.21

Core: CH01-82 42PC

G. ruber (212-250 microns)

depth (cm)	O-18 (PDB)	C-13 (PDB)	depth (cm)	O-18 (PDB)	C-13 (PDB)
1.0	-1.81	.48	85.0	-1.39	.17
3.0	-1.91	.49	85.0	-1.41	.00
5.0	-2.02	-.06	89.0	-1.17	.16
5.0	-1.83	.34	93.0	-.89	.07
9.0	-1.65	.26	97.0	-.53	.10
9.0	-1.89	.10	99.0	-.11	.53
13.0	-1.93	-.18	101.0	-.14	.31
13.0	-1.88	-.55	103.0	-.65	.27
17.0	-1.88	.20	105.0	-.54	.17
17.0	-1.87	-.20	107.0	.01	.38
21.0	-1.73	.54	107.0	-.40	.33
25.0	-1.84	.30	109.0	-.37	.33
29.0	-1.83	.13	109.0	-.19	.03
33.0	-1.75	.22	111.0	.03	.71
37.0	-1.91	-.17	111.0	.02	.35
41.0	-2.16	-.12	113.0	-.05	.39
45.0	-1.85	.21	113.0	.05	.34
45.0	-1.93	-.11	115.0	-.07	.50
49.0	-2.04	-.18	115.0	-.04	.46
49.0	-2.15	-.74	119.0	-.23	.40
53.0	-1.69	-.02	123.0	-.16	.45
57.0	-1.79	-.02	127.0	.01	.35
61.0	-2.07	-.12	131.0	-.20	.50
65.0	-1.79	.11	135.0	-.40	.37
69.0	-1.79	.01	139.0	-.20	.58
73.0	-2.14	-.23	139.0	-.14	.28
77.0	-1.86	-.16	143.0	-.52	.21
77.0	-1.61	.06	147.0	-.39	.27
81.0	-1.79	-.11	151.0	-.51	.10
81.0	-1.81	.01			

CORE	CORE DEPTH (cm)	PLANULINA SPECIES	O-18	C-13
OC205-2 74BC	0-1.0	foveolata	.719	1.446
OC205-2 74BC	0-1.0	foveolata	.687	1.430
OC205-2 50BC	0-1.0	ariminensis	1.396	1.283
OC205-2 53BC	0-1.0	ariminensis	1.934	1.393
OC205-2 53BC	0-1.0	ariminensis	1.906	1.368
OC205-2 55BC	0-1.0	ariminensis	1.879	1.379
OC205-2 69BC	0-1.0	ariminensis	1.003	1.284
OC205-2 70BC	0-1.0	ariminensis	1.420	1.330
OC205-2 50BC	0-1.0	wuellerstorfi	1.195	.834*
OC205-2 53BC	0-1.0	wuellerstorfi	1.842	1.216
OC205-2 53BC	0-1.0	wuellerstorfi	1.724	1.162
OC205-2 55BC	0-1.0	wuellerstorfi	2.020	1.307
OC205-2 59BC	0-1.0	wuellerstorfi	2.252	1.374
OC205-2 59BC	0-1.0	wuellerstorfi	2.206	1.352
OC205-2 67BC	0-1.0	wuellerstorfi	2.080	1.354
OC205-2 70BC	0-1.0	wuellerstorfi	1.415	.993
OC205-2 72BC	0-1.0	wuellerstorfi	1.219	.997

*small sample analyzed when mass spectrometer not optimized for small samples

CORE	CORE DEPTH (cm)	PLANULINA SPECIES	O-18	C-13
OC205-2 149J	1.0	foveolata	0.267	1.617
OC205-2 149J	1.0	foveolata	0.068	1.522
OC205-2 149J	3.0	foveolata	0.168	1.761
OC205-2 149J	3.0	foveolata	0.100	1.750
OC205-2 149J	7.0	foveolata	0.089	1.655
OC205-2 149J	243.0	foveolata	0.652	1.737
OC205-2 149J	247.0	foveolata	0.668	1.781
OC205-2 149J	1.0	ariminensis	0.023	1.583
OC205-2 149J	3.0	ariminensis	-0.153	1.663
OC205-2 106G	7.0	ariminensis	1.011	1.371
OC205-2 106G	10.0	ariminensis	0.950	1.391
OC205-2 106G	13.0	ariminensis	1.073	1.375
OC205-2 106G	13.0	ariminensis	1.016	1.415
OC205-2 108G	6.0	ariminensis	1.320	1.260
OC205-2 108G	10.0	ariminensis	1.305	1.295
OC205-2 108G	13.0	ariminensis	1.261	1.319
OC205-2 33G	10.5	ariminensis	1.499	1.357
OC205-2 33G	13.0	ariminensis	1.295	1.286
OC205-2 33G	87.0	ariminensis	2.731	1.700
OC205-2 33G	90.0	ariminensis	2.376	1.545
OC205-2 33G	90.0	ariminensis	2.332	1.653
OC205-2 149J	243.0	ariminensis	0.913	1.984
OC205-2 149J	247.0	ariminensis	0.982	1.934
OC205-2 106G	110.0	ariminensis	2.363	1.656
OC205-2 106G	110.0	ariminensis	2.184	1.657
OC205-2 106G	113.0	ariminensis	2.176	1.650
OC205-2 106G	117.0	ariminensis	1.970	1.684
OC205-2 106G	117.0	ariminensis	2.130	1.690
OC205-2 108G	147.0	ariminensis	2.521	1.645
OC205-2 108G	150.0	ariminensis	2.474	1.631
OC205-2 108G	153.0	ariminensis	2.630	1.643
OC205-2 108G	157.0	ariminensis	2.341	1.595
OC205-2 103G	10.0	wuellerstrofi	1.750	1.124
OC205-2 100G	7.0	wuellerstrofi	1.903	1.264
OC205-2 100G	10.0	wuellerstrofi	1.804	1.265
OC205-2 7J	1.0	wuellerstrofi	3.125	1.483

CORE	CORE DEPTH (cm)	PLANULINA SPECIES	O-18	C-13
OC205-2 7J	4.0	wuellerstrofi	2.677	1.433
OC205-2 7J	7.0	wuellerstrofi	3.133	1.495
OC205-2 117J	4.0	wuellerstrofi	2.891	1.337
OC205-2 117J	7.0	wuellerstrofi	2.122	1.289
OC205-2 117J	10.0	wuellerstrofi	2.143	1.322
OC205-2 120T	10.0	wuellerstrofi	1.936	1.480
OC205-2 108G	147.0	wuellerstrofi	2.729	1.510
OC205-2 108G	150.0	wuellerstrofi	2.662	1.453
OC205-2 108G	153.0	wuellerstrofi	2.843	1.455
OC205-2 108G	157.0	wuellerstrofi	2.739	1.563
OC205-2 33G	90.0	wuellerstrofi	2.604	1.666
OC205-2 103G	140.0	wuellerstrofi	3.824	1.574
OC205-2 103G	140.0	wuellerstrofi	3.751	1.464
OC205-2 CH42	109.0	wuellerstrofi	3.458	1.566
OC205-2 CH42	111.0	wuellerstrofi	3.192	1.455
OC205-2 CH42	113.0	wuellerstrofi	3.405	1.574
OC205-2 CH42	115.0	wuellerstrofi	3.100	1.482
OC205-2 100G	153.0	wuellerstrofi	3.554	1.569
OC205-2 100G	157.0	wuellerstrofi	3.580	1.588
OC205-2 100G	160.0	wuellerstrofi	3.429	1.459
OC205-2 97J	63.0	wuellerstrofi	3.844	1.529
OC205-2 97J	63.0	wuellerstrofi	3.910	1.536
OC205-2 97J	67.0	wuellerstrofi	3.796	1.570
OC205-2 97J	70.0	wuellerstrofi	3.891	1.568
OC205-2 97J	73.0	wuellerstrofi	3.522	1.506
OC205-2 7J	70.0	wuellerstrofi	3.234	1.422
OC205-2 7J	73.0	wuellerstrofi	3.052	1.478
OC205-2 7J	73.0	wuellerstrofi	3.352	1.328
OC205-2 120J	27.0	wuellerstrofi	3.299	1.474
OC205-2 120J	27.0	wuellerstrofi	3.355	1.507
OC205-2 120J	30.0	wuellerstrofi	3.444	1.487
OC205-2 120J	33.0	wuellerstrofi	3.308	1.486
OC205-2 117J	67.0	wuellerstrofi	3.552	1.424
OC205-2 117J	70.0	wuellerstrofi	3.939	1.443
OC205-2 117J	73.0	wuellerstrofi	3.574	1.377
OC205-2 117J	73.0	wuellerstrofi	3.669	1.414

CORE	CORE DEPTH	PLANULINA SPECIES	AVERAGE O-18	AVERAGE C-13	STANDARD ERROR O-18	STANDARD ERROR C-13
OC205-2 50BC	CT	wuellerstorfi	1.195	.834		
OC205-2 72BC	CT	wuellerstorfi	1.219	.997		
OC205-2 67BC	CT	wuellerstorfi	2.080	1.354		
OC205-2 59BC	CT	wuellerstorfi	2.229	1.363	.016	.008
OC205-2 70BC	CT	wuellerstorfi	1.415	.993		
OC205-2 55BC	CT	wuellerstorfi	2.020	1.307		
OC205-2 53BC	CT	wuellerstorfi	1.783	1.189	.042	.019
OC205-2 50BC	CT	ariminensis	1.396	1.283		
OC205-2 55BC	CT	ariminensis	1.879	1.379		
OC205-2 53BC	CT	ariminensis	1.920	1.381	.010	.009
OC205-2 70BC	CT	ariminensis	1.420	1.330		
OC205-2 69BC	CT	ariminensis	1.003	1.284		
OC205-2 74BC	CT	foveolata	.703	1.438	.011	.006

core-top=CT, glacial=G
average includes replicates

CORE	CORE DEPTH	PLANULINA SPECIES	AVERAGE O-18	AVERAGE C-13	STANDARD ERROR O-18	STANDARD ERROR C-13
OC205-2 149J	CT	foveolata	0.138	1.661	.032	.040
OC205-2 149J	G	foveolata	0.660	1.759	.006	.016
OC205-2 149J	CT	ariminensis	-.065	1.623	.062	.028
OC205-2 106G	CT	ariminensis	1.013	1.388	.022	.009
OC205-2 108G	CT	ariminensis	1.295	1.291	.014	.014
OC205-2 33G	CT	ariminensis	1.397	1.322	.072	.025
OC205-2 33G	G	ariminensis	2.480	1.633	.103	.037
OC205-2 149J	G	ariminensis	0.948	1.959	.024	.018
OC205-2 106G	G	ariminensis	2.165	1.667	.056	.007
OC205-2 108G	G	ariminensis	2.492	1.629	.052	.010
OC205-2 103G	CT	wuellerstorfi	1.750	1.124		
OC205-2 100G	CT	wuellerstorfi	1.854	1.265	.035	.000
OC205-2 7J	CT	wuellerstorfi	2.978	1.470	.123	.016
OC205-2 117J	CT	wuellerstorfi	2.385	1.316	.206	.012
OC205-2 120T	CT	wuellerstorfi	1.936	1.480		
OC205-2 108G	G	wuellerstorfi	2.743	1.495	.032	.023
OC205-2 33G	G	wuellerstorfi	2.604	1.666		
OC205-2 103G	G	wuellerstorfi	3.788	1.519	.026	.039
OC205-2 CH42	G	wuellerstorfi	3.289	1.519	.074	.026
OC205-2 100G	G	wuellerstorfi	3.521	1.539	.038	.033
OC205-2 97J	G	wuellerstorfi	3.793	1.542	.063	.011
OC205-2 7J	G	wuellerstorfi	3.213	1.409	.071	.036
OC205-2 120J	G	wuellerstorfi	3.352	1.489	.029	.006
OC205-2 117J	G	wuellerstorfi	3.684	1.415	.077	.012

core-top=CT, glacial=G
average includes replicates

3.13 Appendix A. Determining the carbonate mineralogy of sediments

The ratio of aragonite to total aragonite and calcite in bulk sediments was determined using x-ray diffraction. The procedure utilized in this study is adapted after that described by Neumann (1965). See Neumann (1965) and Milliman (1974) for further discussion of the methods of sample preparation and data analysis.

Samples were prepared in the following manner: Dry sediments were ground (~1 minute) into a fine powder using an agate mortar and pestle. The powder was packed into a standard dry powder x-ray diffraction slide by pressing on it with a small block of aluminum. This approach is a compromise between (1) loosely packing powder by hand and smoothing its surface with a glass slide (J. Milliman, personal communication), and (2) pressing the powder into the slide against a flat piece of metal at a consistent pressure with a hydraulic press to obtain a very smooth surface (G. Jones, personal communication). The approach was choosen because it was quick, consistent and held the powder in the slide well. All approaches to packing yielded similar results (Table A1).

Analysis was carried out at the Woods Hole Oceanographic Institution using a Philips Electronic Instruments model XRG–3000 x-ray diffraction unit. Cu K α radiation was employed (generated at 40 kilovolts and 20 milliampres). The intensity of diffracted energy was typically measured over the range of 25–32° 2θ by counting for 1 second at intervals of 0.01° 2θ (Figure A1). There was no advantage to using a longer counting time of 2 or 3 seconds (Table A2).

The high and low Mg calcite that occur in marine sediments have the same weight percent–peak area relationship (Milliman, 1974). Known mixtures of coral aragonite and oyster calcite were analyzed (3 second count time) to construct a standard curve. A computer program (Table A3) calculated the areas under the aragonite and calcite peaks (less background) and checked their ratios against those of the standard curve to determine the weight percent of aragonite relative to total aragonite and calcite. No distiction is made between high and low Mg calcite.

Note that the position of a peak for quartz is directly between those of the two primary aragonite peaks. The computer program cannot differentiate the area of quartz peaks from aragonite, so the ratio of aragonite to total aragonite and calcite would be over estimated

in sample containing quartz. Fortunately, the Bahamian sediments considered in this study are typically about 93 percent calcium carbonate and little of the non-carbonate material is quartz. This deficiency could be reduced by changing the 2θ range over which the aragonite peak area is determined from 25.75–26.74° to 25.75–26.4°.

3.13.1 References

Neumann, A. C., 1977, Processes of recent carbonate sedimentation in Harrington Sound, Bermuda: Bulletin of Marine Science, v. 15, p. 987–1035.

Milliman, J. D., 1974, Marine Carbonates, Springer-Verlag, New York, 375 pp.

3.13.2 Tables, Figure and Computer Program

Figure 1A. Examples of x-ray diffraction traces for samples with (a) high ratio of aragonite to calcite and (b) low ratio of aragonite to calcite.

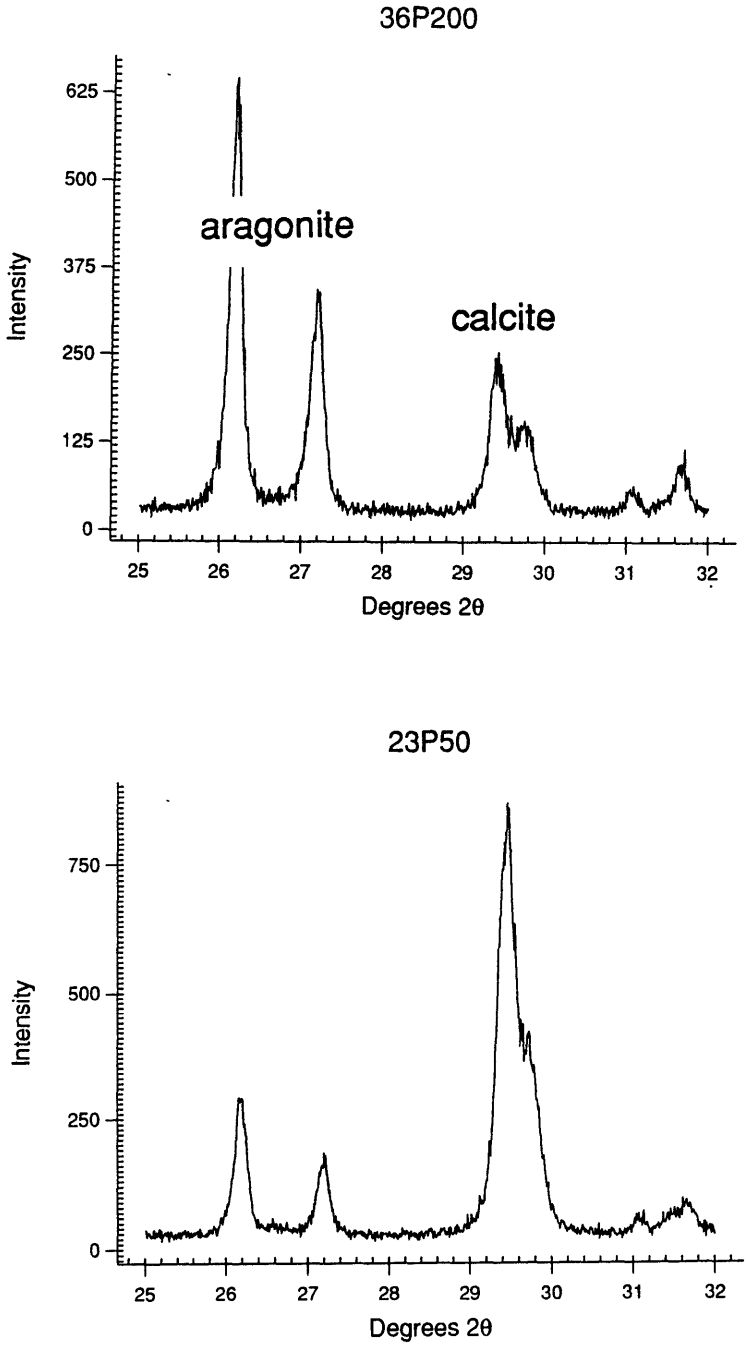

Table A1. Effect of packing method on weight percent aragonite.

	weight % aragonite	
depth (cm)	hand pressed with glass slide	hydraulically pressed at 2 tons
20	70.1	68.3
30	70.6	68.2
70	35.5	35.1
80	38.5	36.0

notes:

1) Samples are from 7 JPC.

2) A separate portion of sediment from each depth was used for each packing approach. Therefore, some some variability may reflect actual differences in the mineralogy of the sediment.

3) The standard deviations of these measurements are about 1 % or less--a nice precision for the x-ray method.

4) According to Milliman (1974, p. 26), 'high' pressure causes calcite to convert to aragonite. Since the hydraulically pressed samples have less aragonite than those pressed by hand, the pressure during hydraulic pressing does not appear great noticably affect the aragonite content of the samples.

Table A2. Effect of counting time on weight percent aragonite

depth (cm)	counting time (sec)	weight % aragonite	mean	standard deviation
	3	84.9		
120	2	85.3	85.0	0.2
	1	84.9		
	3	86.7		
130	2	86.7	86.6	0.1
	1	86.4		
	3	87.5		
140	2	87.6	87.5	0.1
	1	87.4		
	3	32.8		
180	2	32.7	32.7	0.1
	1	32.7		
	3	32.5		
200	2	32.5	32.8	0.5
	1	33.5		
	3	36.3		
220	2	37.7	36.9	0.6
	1	36.7		

notes:

1) Samples are from 144 JPC.

2) Visual inspection of the x-ray traces suggests that the signal to noise ratio is directly related to counting time. As a consequence, the difference between the 3 and 2 second count traces (33% decrease in time) appears less thatn the difference between the 2 and 1 second count traces (50% decrease in time).

3) It is not certain from this comparison that the smallest counting times would be adaquate for resolving the overlapping peaks of high and low Mg calcite.

```
c program:  answer.for
c purpose:  calculate the areas of calcite and aragonite peaks
c           (method modified after Neumann 1965) produced during
c           x-ray difraction run of 25-31 degrees with 0.01 degree
c           steps and determine weight percent of aragonite relative
c           to total aragonite and calcite using a standard curve
c           generated with known mixtures of aragonite and calcite.
c language:  Microsoft Fortran 3.31 for IBM PC
c
      DIMENSION DEG(800),COUN(800)
      CHARACTER*64 INFILE,XINFILE
      OPEN(UNIT=11,FILE='DIR',STATUS='OLD')
c enter xrd data
   10 READ(11,100,END=77)INFILE
c file with names of ascii data files
c do not include extension to filename--it is assumed to be '.as9'
  100 FORMAT(A)
      XINFILE=INFILE
      L = 1 + KLEN(INFILE)
      LL = L+4
      INFILE(L:LL) = '.AS9'
      OPEN (UNIT=10, FILE=INFILE, STATUS='OLD')
      I=1
      DO 20 I=1,800
c data: degree 2 theta and intensity
   20 READ(10,200,END=30,ERR=70)DEG(I),COUN(I)
  200 FORMAT(F10.2,F10.0)
      GO TO 30
   70 write(*,*)' ERROR READING FILE, PROGRAM STOPPED '
      GO TO 80
   30 CONTINUE
c determine average background/step starting at 25.35 degrees for 25 steps
      X=25.35
      CALL FIND(X,I,DEG)
      J=25
      CALL INTEG(I,J,COUN,BACK1)
c determine aragonite peak starting at 25.75 degrees for 100 steps (to 26.74 degrees)
      X=25.75
      CALL FIND(X,I,DEG)
      J=100
      CALL INTEG(I,J,COUN,ARAG)
c determine average backgound/step starting at 28.1 degrees for 25 steps
      X=28.1
      CALL FIND(X,I,DEG)
      J=25
      CALL INTEG(I,J,COUN,BACK2)
c determine calcite peak starting at 28.75 degrees for 175 steps (to 30.49 degrees)
      X=28.75
      CALL FIND(X,I,DEG)
      J=175
      CALL INTEG(I,J,COUN,CAL)
c determine average background/step starting at 30.7 degrees for 25 steps
      X=30.7
      CALL FIND(X,I,DEG)
      J=25
      CALL INTEG(I,J,COUN,BACK3)
c calculate ratio:  aragonite/(aragonite + total calcite)
      ARAG=ARAG-(BACK1+BACK2)*2.0
      IF(ARAG.LT.(0.0))ARAG=0.0
      CAL=CAL-(BACK2+BACK3)*3.5
      IF(CAL.LT.(0.0))CAL=0.0
      RATIO=ARAG/(ARAG+CAL)
      CALL STD(RATIO,X1,Y1,X2,Y2)
      CALL INTERP(X1,Y1,X2,Y2,RATIO,PERCENT)
      write(*,150)XINFILE,PERCENT
  150 FORMAT(1X,A,F10.1)
   15 FORMAT(1X,20A,F10.1)
   80 CONTINUE
      CLOSE(10)
      GO TO 10
   77 CONTINUE
      CLOSE(10)
      CLOSE(11)
```

```
      STOP
      END

      SUBROUTINE INTEG(I,J,COUN,SUM)
      DIMENSION COUN(800)
      SUM=0.0
      DO 42 K=I,I+J-1
   42 SUM=SUM+COUN(K)
      RETURN
      END

      SUBROUTINE FIND(X,I,DEG)
      DIMENSION DEG(800)
      DO 10 I=1,800
   10 IF(X.EQ.DEG(I))GO TO 20
      write(*,100)'DID NOT FIND ',X
  100 FORMAT(F10.4)
   20 CONTINUE
      RETURN
      END


      SUBROUTINE STD(X,X1,Y1,X2,Y2)
c  peak area ratios for known mixtures of aragonite and calcite (standards from STD.DAT)
      REAL RATIO(11),PERCENT(11)
      DATA RATIO/0.0026,0.0210,0.0445,0.0735,0.1095,0.1597,0.2337,
     &          0.3076,0.4389,0.6536,1.0000/
      DATA PERCENT/0.0,10.1,20.1,30.1,40.1,50.0,60.1,70.1,80.0,
     &            90.0,100.0/
      DO 10 I=2,11
   10   IF(RATIO(I).GE.X)GO TO 20
   20 CONTINUE
      X1=RATIO(I-1)
      Y1=PERCENT(I-1)
      X2=RATIO(I)
      Y2=PERCENT(I)
      RETURN
      END

      SUBROUTINE INTERP(X1,Y1,X2,Y2,X,Y)
C
C  given two (x,y) pairs of data, determine the line that goes through
C  them and then given the x values for points on that line, find the
C  corresponding y values
C
C  declare variables
C
C  find slope of line
      S=(Y2-Y1)/(X2-X1)
C  find y-intercept of line
      B=Y1-S*X1
C  find corresponding y value that corresponds to given x value
      Y=S*X+B
      RETURN
      END

      INTEGER FUNCTION KLEN(S)
      CHARACTER*64 S
      J = 65
    1 J = J-1
      IF(J.LE.0) GO TO 2
      IF(S(J:J).EQ.' ') GO TO 1
    2 KLEN = J
      RETURN
      END
```

Chapter 4

Using ^{230}Th or ^{231}Pa in marine sediments to reconstruct the late Quaternary history of sea level

4.1 Abstract

We propose a method to determine past sea levels based on the record of ^{230}Th or ^{231}Pa accumulating in seafloor sediments. The decay of uranium in seawater produces these nuclides, which then adsorb rapidly onto particles settling to the seafloor. Since the concentration of uranium is similar at all depths in the water column, the fluxes of ^{230}Th and ^{231}Pa to the seafloor at any location are proportional to water column height. Consequently changes in sea level must cause changes in these fluxes. At shallow depths (<1000 m), fluctuations of sea level cause changes in the expected ^{230}Th and ^{231}Pa fluxes that are large enough to produce measurable changes in the ^{230}Th and ^{231}Pa content of the sediment.

We have developed two approaches to determine past sea levels from the content of ^{230}Th or ^{231}Pa in sediments: (1) in a single core, the ratio of the past and present fluxes of ^{230}Th or ^{231}Pa to a site on the seafloor is a measure of the ratio of the past and present depths of the site below sea level, and (2) in two or more cores from a region where the vertical input of sediment is similar at all depths in the water column, the concentrations of ^{230}Th or ^{231}Pa in synchronous sediment samples are linearly related to depth and indicate past sea level as the depth where the concentrations extrapolate to zero. The latter approach requires fewer assumptions and allows sea level to be estimated at discrete points in time.

We have applied approach (1) to a core recovered from the margin of Little Bahama Bank, and our preliminary results suggest that this methodology holds promise for sea level reconstruction.

4.2 Introduction

The history of sea-level changes has been partially reconstructed using radiometrically dated coral and mollusc fossils on emergent coastlines. Sea-level history has also been inferred from the continuous $\delta^{18}O$ records of deep-sea foraminifera. For various reasons neither of these two methods is entirely satisfactory, leaving our present understanding of the history of late Quaternary sea-level fluctuations incomplete. In this paper we present an alternative method to determine past sea levels based on the record of ^{230}Th and ^{231}Pa preserved in seafloor sediments. Our method has advantages over some previous approaches: it can reconstruct a continuous record of sea level (not just high or low stands) and it does not require assumptions of constant temperature or uplift rate. Its weakness is that sedimentary processes (down-slope or advective reworking) can alter the record and bias our sea level estimates. Our preliminary results suggest that this method has great potential for providing independent estimates of Quaternary sea-level history.

Ages and elevations of past high stands of sea level have been estimated from radiometrically dated fossils recovered from coral reef terraces and other sea-level indicating features along emergent coastlines (see review by Moore, 1982). It is supposed that reef terraces reflect the combined effects of fluctuating eustatic sea level and the tectonic uplift. Sea levels at the times of reef deposition are derived after assuming sea level at one past point in time and constant uplift rates. A number of difficulties and potential sources of error exist with this method. First, though active uplift serves to separate and preserve the geologic features associated with high stands, the need to assume constant uplift introduces uncertainty into the sea-level estimates. The impact of such uncertainty is less for areas of little or no uplift, but, in these cases, it is more difficult to establish facies relationships and locate datable fossils. Second, diagenesis associated with subaerial exposure upon emergence may alter the isotopic compositions and radiometric ages of the fossils. Finally, fossils deposited during low stands are typically destroyed or buried during subsequent rises of sea level. Lack of

much evidence for low stands is particularly troublesome because without it the sea-level history is incomplete.

By drilling submerged coral reefs offshore from Barbados, Fairbanks (1989) has minimized these difficulties while constructing the best sea-level curve yet for the last deglaciation. A near continuous sequence of corals was recovered—including fossils representative of the low stand during the last glacial maximum (~18 kyrs). During this time, the locality apparently experienced only minimal uplift and the fossils were not subaerially exposed. Unfortunately, older corals cannot be used to extend this sea level reconstruction without encountering the difficulties typically associated with emergent coastlines.

In another approach, the $\delta^{18}O$ of foraminiferal calcite has been used to infer changes in sea level. Since these values reflect both the temperature and $\delta^{18}O$ of the seawater where the calcite precipitated (Epstein et al., 1953), changes in $\delta^{18}O$ indicate some combination of changes in temperature, the mean $\delta^{18}O$ of seawater due to fluctuations in the volume of glacial ice or the local ratio of evaporation to precipitation. Assuming the relationship between the $\delta^{18}O$ and volume of the ice, and assuming constant temperature or using temperature estimates based on faunal assemblages, various authors have inferred sea-level history directly from foraminifera $\delta^{18}O$ records (e.g. Emiliani, 1955; Shackleton, 1967; Shackleton and Opdyke, 1973; Laberyie et al., 1987). However, several uncertainties limit this method. The temperature history of seawater must be determined more precisely to properly account for temperature's influence on both the $\delta^{18}O$ of foraminifera and the empirically determined relationship between changes in the $\delta^{18}O$ of seawater and sea level (Fairbanks and Matthews, 1978; Dodge et al., 1983). Moreover, there are few determinations of the $\delta^{18}O$–sea level relationship (Fairbanks and Matthews, 1978; Chappell and Shackleton, 1986), and the relationship is made complex by the heterogeneous distribution of $\delta^{18}O$ in glacial ice (e.g. Mix and Ruddiman, 1984) and the uncertain mass of glacial ice stored in marine ice shelves (Broecker, 1975; Williams et al., 1981).

Here we propose a method to reconstruct late Quaternary sea level history using the ^{230}Th or ^{231}Pa content of seafloor sediments. The decay of uranium in seawater produces ^{230}Th and ^{231}Pa which adsorb rapidly onto particles settling to the seafloor. Since the concentration of uranium is virtually constant throughout the water column, the flux of

these nuclides to a site on the seafloor is proportional to the height of the water column above the site. This relationship underlies two approaches to estimate past sea level. First, the depth of a site, and hence sea level, at some past time can be inferred from the corresponding rate of ^{230}Th or ^{231}Pa accumulation at that site. Second, when the flux of sediment is the same to several sites spanning a range of depths, the concentration of ^{230}Th or ^{231}Pa in the sediment at any site is proportional to its depth. The relationship between ^{230}Th or ^{231}Pa concentrations and the present-day depths can be extrapolated to sea level at the time of sediment deposition. We describe the assumptions, advantages and disadvantages inherent in this method, illustrating some of them with preliminary estimates of ^{230}Th and ^{231}Pa fluxes for the last glacial maximum and the Holocene in a core from the margin of Little Bahama Bank, Bahamas.

4.3 ^{230}Th and ^{231}Pa in the Ocean

The decay of uranium in seawater produces most of the ^{230}Th and ^{231}Pa found in marine sediments (see review of U- and Th- series by Cochran, 1982). Occurring principally in the form of uranyl carbonate ions, dissolved uranium behaves conservatively and its concentration varies only with salinity. Today, the average concentration of uranium in seawater of 35 ppt is $\sim 3.3 \mu$g/l with a U/salinity ratio of $\sim 9.3 \times 10^{-8}$g/g (Turekian and Chan, 1971; Ku et al., 1977; Chen et al., 1986). This ratio is very uniform throughout the oceans because the mixing time of the oceans ($\sim$1000 yrs) is very short with respect to the residence time of uranium in seawater (Turekian and Chan, 1971; Ku et al., 1977; Cochran, 1982). The mass of uranium in the oceans probably has not undergone large changes during recent glacial-interglacial cycles because the residence time of uranium in sea water ($\sim$200–400 kyrs) (Turekian and Chan, 1971; Ku et al., 1977; Cochran, 1982) is several times longer than the climatic cycles (e.g. Shackleton and Opdyke, 1973).

Uranium in seawater consists of the isotopes ^{238}U, ^{235}U and ^{234}U, which decay as follows: $^{238}\text{U} \rightarrow ^{234}\text{U} \rightarrow ^{230}\text{Th} \rightarrow ^{206}\text{Pb}$ and $^{235}\text{U} \rightarrow ^{231}\text{Pa} \rightarrow ^{204}\text{Pb}$. The production rate of ^{230}Th and ^{231}Pa in a column of water is a function of the intergrated concentration of uranium (Cochran and Osmond, 1976). Since the concentration varies little with depth, the relations are essentially linear:

$$P_i = K_i \int_0^Z U(z)dz \approx K_i U Z \tag{4.1}$$

where i denotes ^{230}Th or ^{231}Pa; P is production rate; U is average uranium concentration; z is depth in meters; Z is seafloor depth; and K is the product of the decay constant for i, the activity ratio of the uranium parent of i and ^{238}U, the mass-activity conversion factor for ^{238}U and the conversion factor for units of length.

Both ^{230}Th and ^{231}Pa are rapidly adsorbed or scavenged onto the surfaces of particles in the water column so that their residence times in the water column are on the scale of decades (Moore and Sackett, 1964; Brewer et al., 1980; Anderson et al., 1983a, 1983b; Nozaki and Nakanishi, 1985). However, a significant difference between these two nuclides is that ^{230}Th is more reactive than ^{231}Pa. As a result, there is less time for ^{230}Th to be advected laterally within the ocean basins before it is scavenged, so there is less spatial variability in the intensity with which it is scavenged (see reviews by Cochran, 1982, and Bacon, 1988). For any area of the seafloor, the average rate of ^{230}Th accumulation is typically within ~30 percent of the rate at which ^{230}Th is produced in the overlying water column. In contrast, only about one third of the ^{231}Pa produced in the ocean's interior accumulates on the underlying seafloor; the remainder is resident in the water column long enough to be advected to the ocean's margins where it is removed.

The flux of ^{230}Th or ^{231}Pa on particles to the seafloor depends directly on its rate of production in the column and the intensity of scavenging:

$$F_i = S P_i \tag{4.2}$$

where F is flux and S is scavenging intensity. The initial concentration of the isotope in sediment at the seafloor is proportional to its flux and inversely proportional to the flux of sediment through the water column:

$$C_i = F_i / F_{sed} \tag{4.3}$$

where C is concentration. Cochran and Osmond (1976) discussed the ratio (R) between the isotope's flux to the seafloor and its accumulation (A) at a given location on the seafloor:

$$R = A_i / F_i \tag{4.4}$$

When sediment accumulates on the seafloor directly beneath the water through which it settled, R equals 1. However, processes such as topographic focusing, bioturbation, winnowing and gravity-driven processes may redistribute sediment at the seafloor so that at any given location R may be more or less than 1.

4.4 Effect of Sea-level Change on ^{230}Th and ^{231}Pa Flux

Above a given location on the seafloor, how does F_{Th} or F_{Pa} respond to glacial-interglacial climatic fluctuations? The mass of oceanic uranium is relatively insensitive to these fluctuations. Yet, as the volume of glacial ice increases, for example, the volume of water in the oceans decreases with the following effects: 1) U increases, which increases F_{Th}, and 2) Z decreases, which decreases F_{Th}.

Consider the effects of a glacial sea-level fall of about 120 meters (Figure 1). At locations where Z is great (for example at typical seafloor depths of 4000 or more meters) the increase in U is about 3 percent and the decrease in Z is about 3 percent. These two effects essentially balance so F_{Th} is nearly constant through time. In such cases, the initial C_{Th} provides a scale against which to compare the relative accumulation rates of other sediment components (Bacon, 1984). At shallow sites, however, the proportional change in water column height is significantly greater than that of U, resulting in a measurable decrease in F_{Th} because of sea-level change. For example, where the seafloor is initially at about 500 meters depth, a sea level fall of 120 meters will increase U still only about 3 percent, while the decrease in sea level is 24 percent of Z, resulting in a 21 percent net decrease in F_{Th}. It is at these shallow depths where our approach can best be used to reconstruct sea level.

4.5 Reconstructing Sea-level History

In this section we describe two approaches for reconstructing sea-level history based on the ^{230}Th and ^{231}Pa found in shallow sediment cores. Though this description focuses on ^{230}Th, in theory, the approaches also apply to ^{231}Pa and sea level estimates for both nuclides will

be presented. In practice, ^{230}Th is potentially more useful than ^{231}Pa because it is more readily scavenged (less spatial and temporal variability of S), it has a longer half life (72,500 versus 34,800 yrs) and it is more easily measured.

4.5.1 Approach 1: one core

One approach to determine past sea level is to compare the past flux of ^{230}Th to the seafloor with the flux today. After accounting for the effects of changing U, the difference between past and present fluxes is proportional to the difference between past and present sea levels. The average F_{Th} for past intervals of time can be inferred from the corresponding A_{Th} in a sediment core. For a given time interval, A_{Th} is the product of the sedimentation rate, the bulk density and C_{Th} at the time of sediment deposition. C_{Th} is calculated from the measured average concentration of ^{230}Th in the corresponding sediments by correcting for the decay of ^{230}Th since deposition, the ^{230}Th supported by sedimentary uranium, and detrital ^{230}Th. Preliminary data and sea level estimates from core CH0182-36 illustrate some processes that affect ^{230}Th accumulation at the seafloor.

Core 36 was recovered from 651 meters depth along the southern margin of Little Bahama Bank, Bahamas (Burns and Neumann, 1987). The sediments are a mixture of pelagic and bank-top carbonate material termed "peri-platform ooze" by Schlager and James (1978), deposition of which occurred primarily by settling through the water column (Burns and Neumann, 1987). Figure 2a displays the δ^{18}O composition of the planktonic foraminifera *Globogerinoides ruber* (white variety, 212–250 μm) versus depth in core 36 (Slowey and Curry, 1987). The negative values at the top of the core correspond to the recent Holocene and the positive values in the lower portion of the record identify sediments from the last glacial maximum. Figure 2b is a plot of the bulk density of dry sediment versus depth. Values were obtained by drying and weighing a known volume of sediment that had been extracted from the core with a calibrated syringe. (These density measurements may be biased because of partial drying between the times of core recovery and density sampling.) The concentration of ^{230}Th was measured in two samples each from the recent Holocene and the last glacial maximum (Figure 2c, Table 1). Stipples in Figures 2a and 2b indicate the δ^{18}O and bulk density measurements which correspond to these ^{230}Th mea-

surements. The concentrations of ^{238}U, ^{235}U, ^{234}U, ^{231}Pa and ^{232}Th were also determined so that the concentrations of ^{230}Th and ^{231}Pa at the time of sediment deposition could be estimated (Table 1). Radio-isotope measurements were made in the laboratory of Michael Bacon at the Woods Hole Oceanographic Institution using standard techniques (Anderson and Fleer, 1982).

Estimating past accumulations of ^{230}Th requires accurate estimates of the sedimentation rate. For core 36, sedimentation rates are based on three age–depth models (Figure 3). One is based on the bulk sediment ^{14}C ages of Burns and Neumann (1987), except the core-top age is assumed to be zero kyrs rather than 1.3 kyrs as indicated by ^{14}C because bioturbation caused the old ^{14}C age (e.g. Nozaki et al., 1977; Peng, et al., 1977). The other two age–depth models are based on correlating the $\delta^{18}O$ record of core 36 to that of core V19–30 (Shackleton et al., 1983) and using the chronologies of Imbrie et al. (1984) and Shackleton and Pisias (1985) for oxygen-isotope stage boundaries 1–2 and 2–3. Since there are no ^{14}C ages to constrain stage two, we do not use the ^{14}C age model to calculate the glacial accumulation of ^{230}Th.

Using ages derived from these models (via linear interpolation), the measured concentrations of ^{238}U, ^{234}U and ^{232}Th, and assuming the sediments have remained a closed system with respect to uranium and thorium, the radio-active decay equations are solved (Bateman, 1910) to yield the concentrations of ^{230}Th and ^{232}Th at the time of sediment deposition (Table 2). The portion of thorium produced by uranium dissolved in seawater is that which remains after accounting for thorium produced by uranium incorporated in detrital sediment.

Assuming that only detrital sediment contains ^{232}Th, detrital ^{230}Th is accounted for by indexing it to ^{232}Th. Since our purpose is simply to illustrate the potential of the ^{230}Th method, no attempt was made to experimentally determine this ratio in core 36. Rather, it was assumed to be 1 based on the approximate abundances of Th and U in continental crust (Taylor and McLennan, 1985) and assuming secular equilibrium among detrital ^{238}U, ^{234}U and ^{230}Th. To account for detrital ^{231}Pa, a $^{235}U/^{238}U$ activity ratio of 0.046 and secular equilibrium between ^{235}U and ^{231}Pa were assumed for detrital sediments. It is possible that the actual ratios are different and, as discussed below, this would affect the calculated

values of A_{Th} and sea-level change.

Average values of A_{sed}, A_{Th} and A_{Pa} for stages 1 and 2 based on the preliminary data for core 36 are shown in Table 3. Notice that A_{Th} for stage 1 ($\sim$3.3 dpm/cm^2/kyr) is nearly twice the P_{Th} of the overlying waters today (1.73 dpm/cm^2/kyr). Whether or not more data would continue to support this difference, it is instructive to assume that it would and to consider the processes involved. One way to account for this would be for the activity ratio of detrital ^{230}Th and ^{232}Th to be 4.6 rather than 1 as we assumed. We suspect that this is not the case since such a ratio would be outside the range of values other workers have reported. According to Ku and Liang (1984), the ratio commonly lies between 1 and 3, and in the specific case of marine sediments, Anderson et al. (1990) estimated the ratio to be 0.8$\pm$0.2. It is also not likely that the difference between A_{Th} and P_{Th} results from sea level being appreciably higher during the recent Holocene than it is today. This would require—unrealistically—that the average recent Holocene sea level be $\sim$300 meters higher than modern sea level.

It does not seem likely that the excess ^{230}Th reflects a high intensity of ^{230}Th scavenging in the overlying waters (i.e. $S > 1$). The Holocene ratio of ^{230}Th to ^{231}Pa from the water in core 36 is 17.8, within the range of values typically found under pelagic conditions (Cochran, 1982; Bacon, 1988). Also, the A_{sed} for the Holocene in core 36 is about 5 g/cm^2/kyr. For the same value of sediment flux through the water in pelagic conditions, the corresponding flux of ^{230}Th to the seafloor about equals the rate of production (Bacon, personal communication). The sediment flux would have to be significantly greater for intense scavenging to account for much of the difference between ^{230}Th production and accumulation at the site of core 36.

Much of the excess ^{230}Th could result from a large difference between the general flux of ^{230}Th to the seafloor and its accumulation locally at the site of core 36 (i.e. $R > 1$). Among the reasons that we selected core 36 to illustrate this approach to using ^{230}Th to reconstruct past sea levels is that the core displayed no obvious evidence of sediment redistribution by turbidity or debris flows. Nevertheless, it is easy to envision processes along the steep margin of Little Bahama Bank that could cause local variations of sediment (and ^{230}Th) accumulation such as topographic focusing, bioturbation, winnowing and fine

scale down-slope transport. One way to evaluate this possibility would be to compare the sediment accumulations measured in one core with the regional average.

Having considered some of the processes that affect the accumulation of ^{230}Th at the seafloor, how are these accumulations used to estimate past sea levels? Combining equations (1), (2) and (4) yields the general relationship among the depth and accumulation of ^{230}Th or ^{231}Pa on the seafloor today and the depth and accumulation during the past:

$$z_{past} = \frac{A_{past}/(KS_{past}R_{past}U_{past})}{A_{today}/(KS_{today}R_{today}U_{today})} z_{today} \tag{4.5}$$

We assume that the activity ratios among the uranium isotopes in seawater remain constant so K also remains constant. We assume that R has not varied between stages 1 and 2. High resolution 3.5 kHz profiles of the site of core 36 suggest that the spatial pattern of sediment deposition has not varied significantly during the last several hundred thousand years (Burns and Neumann, 1987). Therefore, the effect of sediment focusing on R probably did not vary much either. Nevertheless, we recognize that "random" effects such as bioturbation or sediment ripples on R cannot be evaluated with data from just one core. We assume that scavenging efficiency (S) has also remained constant over this period of time. Importantly, such constancy is generally more likely for ^{230}Th than for ^{231}Pa. There is little change in the ratio of ^{230}Th to ^{231}Pa between stages 1 and 2 in core 36, consistent with little change in the processes and intensity of scavenging. Further, the difference between the sediment accumulation rates of stages 1 and 2 is only about 1 g/cm^2/kyr and there is probably little change of scavenging intensity with such a small change of flux (Bacon, personal communication). If such a flux change for peri-platform sediments does noticeably affect scavenging intensity, then assuming that S is a constant will result in an over estimate of sea-level change from stages 2 to 1.

Assuming that U is also constant through time, the relationship can be simplified to:

$$z_{past} = \frac{A_{past}}{A_{today}} z_{today} \tag{4.6}$$

Actually, as noted above, U varies during the late Quaternary because the volume of the oceans changes as glaciers advance and retreat while the mass of uranium in the ocean does not. In the absence of large floating marine ice sheets, the effect of assuming U constant is

that estimated changes of sea level (difference between present and estimated past seafloor depths) are minimum values.

Changes of U with time can be accounted for by assuming that changes in sea level and mean ocean uranium concentration are linearly related with a slope of m:

$$U_{past} = m(Z_{past} - Z_{today}) + U_{today} \tag{4.7}$$

Based on several different lines of reasoning, Broecker and Peng (1982, p. 448) concluded that mean ocean salinity increases by about 3.5 percent if sea level falls 150 meters. Since U is proportional to salinity, this suggests 3.5 percent of today's mean ocean uranium concentration divided by 150 meters as a reasonable value for m. If S and R are constant through time, equations (5) and (7) combine into the following equation:

$$Z_{past} + Z_{past}\frac{U_{today} - mZ_{today}}{m} - \frac{A_{past}U_{today}Z_{today}}{mA_{today}} = 0 \tag{4.8}$$

This approach has been applied to our preliminary data for core 36 to estimate the rise in sea level from $\delta^{18}O$ stage 2 to stage 1 (Table 3). Depending on the age–depth model and nuclide used, these estimates range from about 170 to 235 m. If only the uncertainties in measuring sediment density ($\sim 5\%$) and counting decays of ^{230}Th ($\sim 2\%$) or ^{231}Pa ($\sim 5\%$) are considered, then the uncertainty in the estimates of sea-level rise is about ± 70 m or ± 95 m when they are based upon the accumulation of ^{230}Th or ^{231}Pa, respectively. Within this uncertainty, our results are consistent with the determination by Fairbanks (1989) that this rise was 121 ± 5 m. This favorable comparison supports the reasoning which underlies our approach and is particularly encouraging considering the preliminary nature of the data for core 36.

Estimates of sea-level change based upon the accumulation of ^{230}Th or ^{231}Pa in core 36 can be improved by reducing several sources of uncertainty. First, the age–depth models are quite coarse and could be developed in greater detail. Second, the sediment density and nuclide concentrations in $\delta^{18}O$ stages 1 and 2 are characterized by only two measurements each. Since sediment properties fluctuate with depth in the core due to variation of environmental conditions in the ocean with time (e.g. difference between nuclide concentrations within each stage is greater than counting uncertainty), the average density and

nuclide concentrations could be better characterized with more measurements. More measurements would also reduce the effect of random error. Third, detrital ^{230}Th and ^{231}Pa are accounted for by assuming the detrital ^{230}Th/^{232}Th and ^{235}U/^{238}U activity ratios—instead, these ratios might be measured directly. As illustrated in Figure 4, estimates of the rise in sea level based on ^{230}Th accumulations in core 36 are sensitive to this ratio. Fourth, the analytical uncertainty involved in measuring sediment density and nuclide concentrations can be reduced by calculating bulk density from water content and grain density, and measuring nuclides by mass spectrometry instead of α-spectrometry (Edwards et al., 1986) or at least increasing counting time in the case of α-spectrometry.

Approach 2: two or more cores

Another approach to determine past sea level is based on the relationship between depth and the flux of ^{230}Th (or ^{231}Pa) to the seafloor. This relationship indicates sea level as the depth where the flux of ^{230}Th equals zero. If the flux of sediment to several sites on the seafloor is the same, sea level can be inferred from the relationship between the depths and the concentrations of ^{230}Th in synchronous sediments from these sites. These concentrations are calculated by correcting the measured ^{230}Th concentrations in the corresponding sediments for ^{230}Th supported by sedimentary uranium and detrital ^{230}Th.

The following are the theoretical bases and the underlying assumptions of the approach. Combining equations (1), (2) and (3) yields the following linear relationship:

$$C = \frac{KUS}{F_{sed}} z. \tag{4.9}$$

Given synchronous sediment samples from cores recovered from a range of depths, the slope of this relationship is the change of C divided by the change depth. Sea level at the time of sediment deposition can be determined by simply fitting a line to a plot of C versus core depth and extrapolating it to the depth where C equals zero (Figure 5). We assume that at any particular time, K, U, S and F_{sed} are the same in the waters overlying each core site.

F_{sed} varies from region to region in the oceans because the processes governing biologic activity in overlying waters and the physical input of sediment from other sources vary geographically. Since spatial variability of F_{sed} within a region is generally continuous, if

core sites are spaced closely enough, the values of F_{sed} at all sites will be essentially the same. The same reasoning applies to both S and U. In addition, U and K will be essentially the same since uranium in seawater behaves conservatively and has a long residence time relative to the mixing time of the oceans.

This second approach to reconstructing sea level using ^{230}Th and ^{231}Pa has several advantages relative to the first approach. In the first approach, changes of sea level through time are inferred from changes in the accumulation rates of these isotopes through time. One difficulty is that accumulation rates are sensitive to the precision of bulk density measurements and, as the preliminary sea level estimates from core CH0182–36 showed, the age–depth model employed. Other difficulties are that accumulation rates are affected by temporal variations in U and may be affected by temporal variations in local sedimentary processes (R) and the intensity of scavenging (S). The second approach avoids these difficulties. First, it does not require rates of ^{230}Th and ^{231}Pa accumulation at the seafloor to be measured. Second, it is independent of temporal variations of F_{sed}, S, U and K because only synchronous sediment samples are utilized. Finally, the length of the intervals of time for which the first approach yields estimates of average sea level is constrained by our ability to develop the resolution of the age–depth model for a given sediment core. In contrast, following the second approach past sea levels can be estimated at discrete points in time including sea-level maxima, minima and the transitions between these extremes.

4.6 Summary

^{230}Th and ^{231}Pa in marine sediments have unique properties that make them useful for reconstructing the late Quaternary history of sea level. The production of these isotopes in the column of water overlying a site on the seafloor is a direct function of the water column's height. Since both ^{230}Th and ^{231}Pa are rapidly scavenged by particles settling to the seafloor, the content of these isotopes in marine sediments preserves continuous records of water column height or sea level. The half-lives of ^{230}Th and ^{231}Pa are long enough (72,500 and 34,800 yrs, respectively) so that these records span significant sea-level events during the last few hundred-thousand years.

We have presented two approaches for reconstructing sea-level history using this ^{230}Th

and ^{231}Pa. First, changes in sea level are inferred from changes in the accumulation rates of these isotopes in sediment. Application of this approach to preliminary data to core CH0182–36 from Little Bahama Bank illustrates some of its advantages and disadvantages, and yields reasonable estimates for sea level during the last glacial maximum. Second, the relationship between concentrations of ^{230}Th or ^{231}Pa from synchronous sediment samples collected from limited geographic and wide bathymetric ranges indicates sea level at the time of sediment deposition, circumventing many disadvantages associated with the first approach. This second approach will be applied to a suite of sediment cores that we collected from the margin of Little Bahama Bank during December of 1988.

4.7 Acknowledgements

We thank A. C. Neumann for permission to sample CH0182–36. We thank A. Fleer for making the radio-isotope measurements. We are indebted to M. Bacon for many helpful discussions about the marine chemistries of U, ^{230}Th and ^{231}Pa. We thank E. Boyle, R. Fairbanks, L. Keigwin, G. P. Lohmann and D. Suman for helpful discussions. We thank M. Bacon, E. Bard and E. Boyle for reviewing the manuscripts first draft. This work was supported by NSF grants OCE85-11014 and OCE88-13307.

4.8 References

Anderson, R. F., and A. P. Fleer, Determination of natural actinides and plutonium in marine particulate material, *Analytical Chemistry,* 54, 1142–1147, 1982.

Anderson, R. F., M. P. Bacon and P. G. Brewer, Removal of ^{230}Th and ^{231}Pa from the open oceans, *Earth Planet. Sci. Lett.,* 62, 7–23, 1983.

Anderson, R. F., M. P. Bacon and P. G. Brewer, Removal of ^{230}Th and ^{231}Pa at ocean margins, *Earth Planet. Sci. Lett.,* 66, 73–90, 1983.

Anderson, R. F., Y. Lao, W. S. Broecker, S. E. Trumbore, H. J. Hofmann and W. Wolfli, Boundary scavengin in the Pacific Ocean: a comparison of ^{10}Be and ^{231}Pa, *Earth Planet. Sci. Lett.,* 96, 287–304, 1990.

Bacon, M. P., Glacial to interglacial changes in carbonate and clay sedimentaion in the Atlantic ocean estimated from ^{230}Th measurements, *Isotope Geoscience,* 2, 97–111, 1984.

Bacon, M. P., Tracers of chemical scavenging in the ocean: boundary effects and large-scale chemical fractionation, *Phil. Trans. R. Soc. Lond.,* 325, 147–160, 1988.

Bateman, H., Solution of a system of differential equations occuring in the theory of radioactive transformations, *Proc. Cambridge Phil. Soc.,* 15, 423–427, 1910.

Bloom, A. L., W. S. Broecker, J. Chappell, R. K. Matthews and K. J. Mesolella, Quaternary sea elvel fluctuations on a tectonic coast: new ^{230}Th/^{234}U dates from the Huon Peninsula, New Guinea, *Quat. Res.,* 4, 185–205, 1974.

Brewer, P. G., Y. Nozaki, D. W. Spencer and A. P. Fleer, Sediment trap experiments in the deep North Atlantic: isotopic and elemental fluxes, *J. Mar. Res.,* 38, 703–728, 1980.

Broecker, W. S., and D. L. Thurber, Uranium-series dating of corals and oolites from Bahaman and Florida Key limestones, *Science* 149, 58–60, 1965.

Broecker, W. S., Floating glacial ice in the Arctic Ocean, *Science* 149, 58–60, 1965.

Broecker, W. S., D. L. Thurber, J. Goddard, T-L. Ku, R. K. Matthews and K. J. Mesolella, Milankovitch hypothesis supported by precise dating of coral reefs and deep-sea sediments, *Science* 159, 1–4, 1968.

Broecker, W.S., and Peng, T-H., Tracers in the Sea, 690 pp., Eldigio Press, New York, 1982.

Burns, S. J., and A. C. Neumann, Pelagic sedimentation on an inactive gullied slope, Northwest Providence Channel, Bahamas, *Mar. Geol.,* 77, 277–286, 1987.

Chappell, J., Geology of coral terraces, Huon Peninsuls, New Guinea: a study of Quaternary tectonic movements and sea-level changes, *Geol. Soc. Am. Bull.,* 85, 553–570, 1974.

Chappell, J., and N. J. Shackleton, Oxygen isotopes and sea level, *Nature*, 324, 137–140, 1986.

Chen, J. H., R. L. Edwards and G. J. Wasserburg, ^{238}U, ^{234}U, and ^{232}Th in seawater, *Earth Planet. Sci. Lett.*, 80, 241–251, 1986.

Cochran, J. K., The oceanic chemistry of the U- and Th-series nuclides, in *Uranium Series Disequilibrium: Applications to Environmental Problems*, edited by M. Ivanovitch and R. S. Harmon, pp. 384–430, Clarendon Press, Oxford, 1982.

Cochran, J. K., and J. K. Osmond, Sedimentation patterns and accumulation rates in the Tasman Basin, *Deep-Sea Res.*, 23, 193–210, 1976.

Dodge, R. E., R. G. Fairbanks, L. K. Benninger and F. Maurrasse, Pleistocene sea levels from raised coral reefs of Haiti, *Science*, 219, 1423–1425, 1983.

Edwards, R. L., J. H. Edwards and G. J. Wasserburg, ^{238}U- ^{234}U- ^{230}Th- ^{232}Th systematics and the precise measurement of time over the past 500,000 years, *Earth Planet. Sci. Lett.*, 81, 175–192, 1986/87.

Emiliani, C., Pleistocene temperatures, *J. Geol.*, 63, 538–578, 1955.

Epstein, S., R. Buchsbaum, H. A. Lowenstam and H. C. Urey, REvised carbonate-water isotopic temperature scale, *Geol. Soc. Am. Bull.*, 64, 13115–1325, 1953.

Fairbanks, R. G., A 17,000-year glacio-eustatic sea level record: influence of glacial melting rates on the Younger Dryas event and deep-ocean circulation, *Nature* 342, 637–642, 1989.

Fairbanks, R. G., and R. K. Matthews, The marine oxygen isotope record in Pleistocene coral, Barbados, West Indies, *Quat. Res.*, 10, 181–196, 1978.

Imbrie, J., J. D. Hays, D. G. Martinson, A. McIntyre, A. C. Mix, J. J. Morley, N. G. Pisias, W. L. Prell and N. J. Shackleton, The orbital theory of Pleistocene climate: support from a revised chronology of the marine $\delta^{18}O$ record, in *Milankovitch Climate, Part 1*, edited by A. L. Berger et al., pp. 269–305, 1984

Konishi, K., S. O. Schlanger and A. Omura, Neotectonic rates in the central Ryukyu Islands derived from ^{230}Th coral ages, *Mar. Geol.*, 9, 225–240, 1970.

Ku, T.-L., M. A. Kimmel, W. H. Easton and T. J. O'Neil, Eustatic sea level 120,000 years ago on Oahu, Hawaii, *Science*, 183, 959–962, 1974.

Ku, T.-L., K. G. Knauss and G. G. Mathieu, Uranium in open ocean: concentration and isotopic composition *Deep-Sea Res.*, 24, 1005–1017, 1977.

Ku, T.-L., and Z.-C. Liang, The dating of impure carbonates with decay-series isotopes, *Nucl. Instr. and Meth.*, 223, 563–571, 1984.

Labeyrie, L., J. C. Duplessy and P. L. Blanc, Variations in mode of formation and temperature of oceanic deep eater over the past 125,000 years, *Nature,* 327, 477–482, 1987.

Land, L. S., F. T. Mackenzie and S. J. Gould, Pleistocene history of Bermuda, it Geol. Soc. Am. Bull., 78, 993–1006, 1967.

Matthews, R. K., Relative elevation of late Pleistocene high sea level stands: Barbados uplift rates and their implications, *Quat. Res.,* 3, 147–153, 1973.

Mesolella, K. J., R. K. Matthews, W. S. Broecker and D. L. Thurber, The astronomical theory of climatic change: Barbados data, *J. Geol.,* 77, 250–274, 1969.

Mix, A. C., and W. R. Ruddiman, Oxygen-isotope analyses and Pleistocene ice volumes, *Quat. Res.,* 21, 1–20, 1984.

Moore, W. S., Late Pleistocene sea-level history, in *Uranium Series Disequilibrium: Applications to Environmental Problems,* edited by M. Ivanovitch and R. S. Harmon, pp. 384–430, Clarendon Press, Oxford, 1982.

Moore, W. S., and W. M. Sackett, Uranium and thorium series inequilibrium in sea water, *J. Geophys. Res.,* 69, 5401–5405, 1964.

Neumann, A. C., and W. S. Moore, Sea level events and Pleistocene coral ages in the northern Bahamas, *Quat. Res.,* 5, 215–224, 1975.

Nozaki, Y., and T. Nakanishi, ^{231}Pa and ^{230}Th profiles in the open ocean water column, *Deep-Sea Res.,* 32, 1209–1220, 1985.

Nozaki, Y., J. K. Corchran, K. K. Turekian and G. Keller, Radio-carbon and ^{210}Pb distribution in submersible-taken deep-sea core from Project Famous, *Earth and Planet. Sci. Lett.,* 34, 167–173, 1977.

Osmond, J. K., J. R. Carpenter and H. L. Windom, Th^{230}/U^{234} age of Pleistocene corals and oolites of Florida, *J. Geophys. Res.,* 70, 1843–1847, 1965.

Peng, T.-H., W. S. Broecker, G. Kipphut and N. Shackleton, Benthic mixing in deep sea cores as determined by ^{14}C dating and its implications regarding climatic change, stratigraphy, and the fate of fossil fuel CO_2, in *The Fate of Fossil Fuel CO_2 in the Oceans,* edited by N. R. Anderson and A. Malahoff, pp. 355–374, Plenum, New York, 1977.

Schlager, W., and N. P. James, Low-magnesian calcite limestones forming at the deep-sea floor, Tongue of the Ocean, Bahamas, *Sedimentology,* 25, 675–702, 1978.

Shackleton, N. J., Oxygen isotope analyses and Pleistocene temperatures, re-assessed, *Nature,* 215, 15–17, 1967.

Shackleton, N. J., and N. D. Opdyke, Oxygen isotope and paleomagnetic stratigraphy of equatorial Pacific core V28–238: oxygen isotope temperatures and ice volumes on a 10^5 and a 10^6 year time scale, *Quat. Res,* 3, 39–55, 1973.

Shackleton, N. J., and N. G. Pisias, Atmospheric carbon dioxide, orbital forcing, and climate, in *The Carbon Cycle and Atmospheric CO_2: Archean to Present, Geophysical Monograph 32,* edited by E. T. Sunquist and W. S. Broecker, pp. 303–317, American Geophysical Union, Washington, 1985.

Shackleton, N. J., J. Imbrie and M. A. Hall, Oxygen and carbon isotope record of East Pacific core V19–30: implications for the formation of deep water in the late Pleistocene North Atlantic *Deep-Sea Res.,* 65, 233–244, 1983.

Slowey, N. C., and W. B. Curry, Structure of the glacial thermocline at Little Bahama Bank, *Nature* 328, 54–58, 1987.

Stearns, C. E., and D. L. Thurber Th^{230}/U^{234} dates of late Pleistocene marine fossils from the Mediterranean and Moroccan littorals, *Quaternaria,* 7, 29–42, 1965.

Taylor, S.R., and McLennen, S.M., The Continental Crust: its Composition and Evolution, 312 pp., Balckwell Scientific Publications, Oxford, 1985.

Turekian, K. K., and L. H. Chan, The marine geochemistry of the uranium isotopes, Th^{230} and Pa^{231}, in *Activation Analysis in Geochemistry and Cosmochemistry,* edited by A. O. Brunfeldt and E. Steinnes, pp. 311–320, Universitetsforlaget, Oslo, 1971.

Veeh, H. H., Th^{230}/U^{238} and U^{234}/U^{238} ages of Pleistocene high sea level stand, *J. Geopys. Res.,* 71, 3379–3386, 1966.

Veeh, H. H., and J. Chappell, Astronomical theory of climatic change: support from New Guinea, *Science,* 167, 862–865, 1970.

Williams, D. F., W. S. Moore and R. H. Fillon, Role of glacial Actic Ocean ice sheets in Pleistocene oxygen isotope and sea level records, *Earth and Planet. Sci. Lett.,* 56, 157–166, 1981.

4.9 Tables

TABLE 1. CH0182–36 Nuclide Concentrations (dpm/g)

Depth (cm)	^{230}Th	^{232}Th	^{231}Pa	^{238}U	^{234}U/^{238}U
5.0	0.717±.013	0.0675±.0029	0.0384±.0022	2.213±.020	1.137±.009
8.5	0.864±.017	0.0782±.0036	0.0501±.0014	2.533±.021	1.141±.021
58.5	0.797±.014	0.1382±.0044	0.0528±.0019	0.736±.009	1.082±.017
64.0	0.700±.013	0.1232±.0042	0.0225±.0015	0.659±.011	1.112±.023

TABLE 2. CH0182–36 Nuclide Concentrations (dpm/g) at Time of Sediment Deposition

Age–depth Model†	Depth (cm)	Age (yr)	Total ^{238}U	Total ^{234}U	Total ^{230}Th	Total ^{235}U	Total ^{231}Pa	Total ^{232}Th	Water ^{230}Th	Water ^{231}Pa
a	5.0	1133	2.213	2.517	0.698	0.102	0.0370	0.0675	0.631	0.0338
	8.5	1927	2.533	2.892	0.828	0.117	0.0475	0.0782	0.750	0.0439
	58.5	—	—	—	—	—	—	—	—	—
	64.0	—	—	—	—	—	—	—	—	—
b	5.0	1370	2.213	2.517	0.694	0.102	0.0366	0.0675	0.627	0.0335
	8.5	2328	2.533	2.893	0.820	0.116	0.0469	0.0782	0.742	0.0434
	58.5	17952	0.736	0.800	0.797	0.034	0.0609	0.1382	0.659	0.0546
	64.0	20306	0.659	0.737	0.693	0.030	0.0186	0.1232	0.569	0.0129
c	5.0	1304	2.213	2.517	0.695	0.102	0.0367	0.0675	0.628	0.0336
	8.5	2217	2.533	2.892	0.822	0.116	0.0471	0.0782	0.744	0.0435
	58.5	16688	0.736	0.799	0.797	0.034	0.0603	0.1382	0.659	0.0539
	64.0	18750	0.659	0.737	0.693	0.030	0.0190	0.1232	0.570	0.0133

†Age–depth model bases: (a) bulk sediment ^{14}C ages of Burns and Neumann (1987), (b) correlation to δ^{18}O chronology of Imbrie et al. (1984), and (c) correlation to δ^{18}O chronology of Shackleton and Pisias (1985).

TABLE 3. CH0182–36 Accumulation Rates of Sediment ($g/cm^2/kyr$) and Nuclides ($dpm/cm^2/kyr$) with Estimated Change of Sea level (m)

	Age–depth	Accumulation Rate		Sea-level Change	
	Model†	stage 2	stage 1	$U = const$	$U = f(sea\ level)$
sediment	a	—	5.42		
	b	3.39	4.49		
	c	3.87	4.72		
^{230}Th	a	—	3.74	—	—
	b	2.38	3.24	172	193
	c	2.08	3.08	210	234
^{231}Pa	a	—	0.21	—	—
	b	0.15	0.16	170	190
	c	0.13	0.18	186	207

†Age–depth models same as for Table 2.

4.10 Figure captions

Figure 1. The response of ^{230}Th flux to shallow and deep sites on the seafloor to a hypothetical glacial fall in sea level. At the deep site, resulting percentage decrease of the site's depth and increase of the uranium concentration in seawater balance so that the ^{230}Th flux does not change. At the shallow site, the percentage decrease in site depth is much greater than the increase of uranium concentration so that the glacial ^{230}Th flux decreases.

Figure 2. Measurements of (a) the ^{18}O of *G. ruber*, (b) dry bulk density and (c) the concentration of ^{230}Th versus depth in core CH0182–36. Stippling indicates ^{18}O and density data corresponding to ^{230}Th measurements.

Figure 3. The δ^{18}O of *G. ruber* versus depth and three age–depth models for core CH0182–36. Boundaries of oxygen-isotope stages 1 and 2 are recognizable from the shape of the δ^{18}O record. Triangles indicate bulk sediment ^{14}C dates of Burns and Neumann (1987), except that we have assumed that the core-top age is zero rather than use their date of 1.27 kyrs. Circles indicate ages obtained by correlating the δ^{18}O record of core CH0182–36 to core V19–30 (Shackleton et al., 1983) and using the ages of Imbrie et al. (1984) and Shackleton and Pisias (1985) for the boudaries of stages 1 and 2.

Figure 4. Estimated sea-level change between stages 1 and 2 based on the accumulation of ^{230}Th in CH0182–36 versus the ratio of detrital ^{230}Th and ^{232}Th activities. The sea-level change increases as the ratio increases. Increasing the ratio decreases ^{230}Th accumulations more during stage 2 than stage 1 because the ^{232}Th concentration in stage 2 is about twice that in stage 1.

Figure 5. If at any given time the flux of sediment through the water is constant to sites on the seafloor at several depths, then the concentrations of this ^{230}Th in the sediments will be linearly related to the depths. A line fitted through a plot of the ^{230}Th concentrations of synchronous samples versus depth indicates sea level at the time of sediment deposition as the depth where the concentration extrapolates to zero.

4.11 Figures

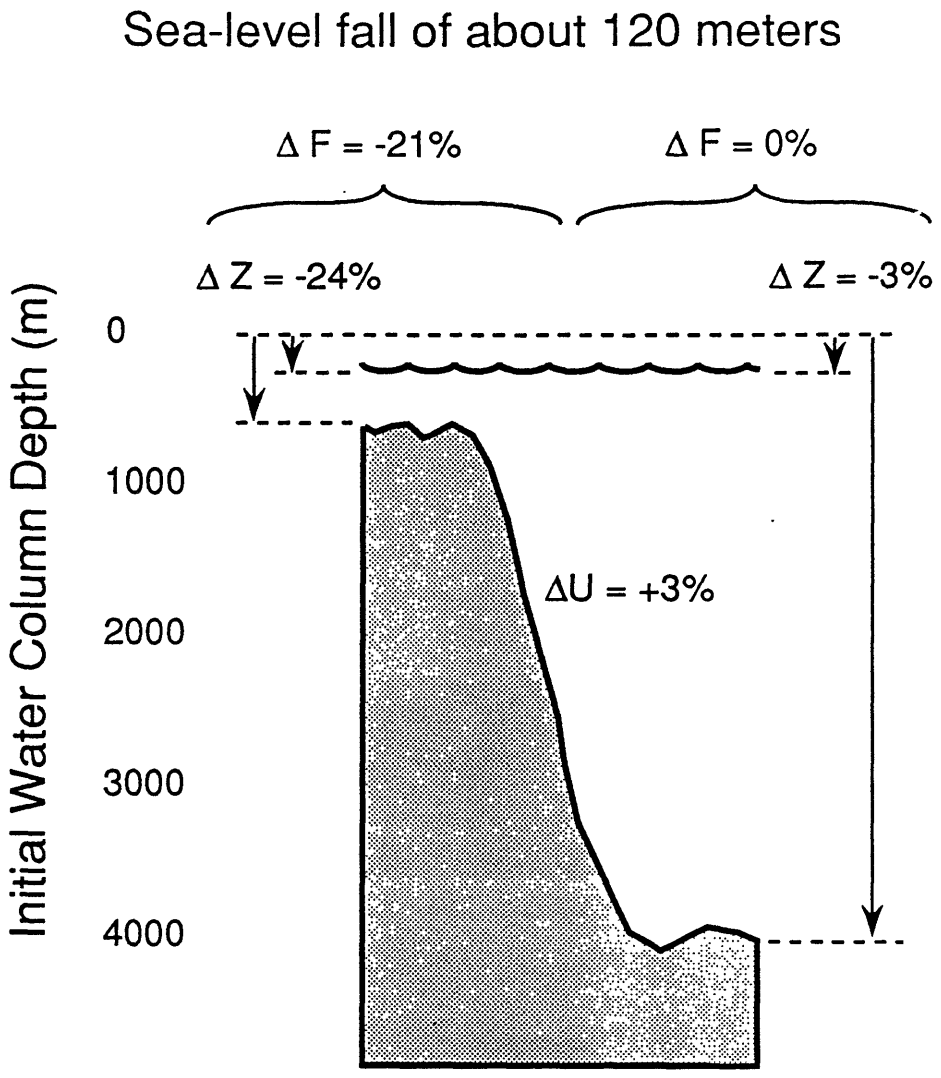
Sea-level fall of about 120 meters
Δ F = -21%
Δ F = 0%
Δ Z = -24%
Δ Z = -3%
Initial Water Column Depth (m)
0
1000
2000
3000
4000
ΔU = +3%

Figure 1.

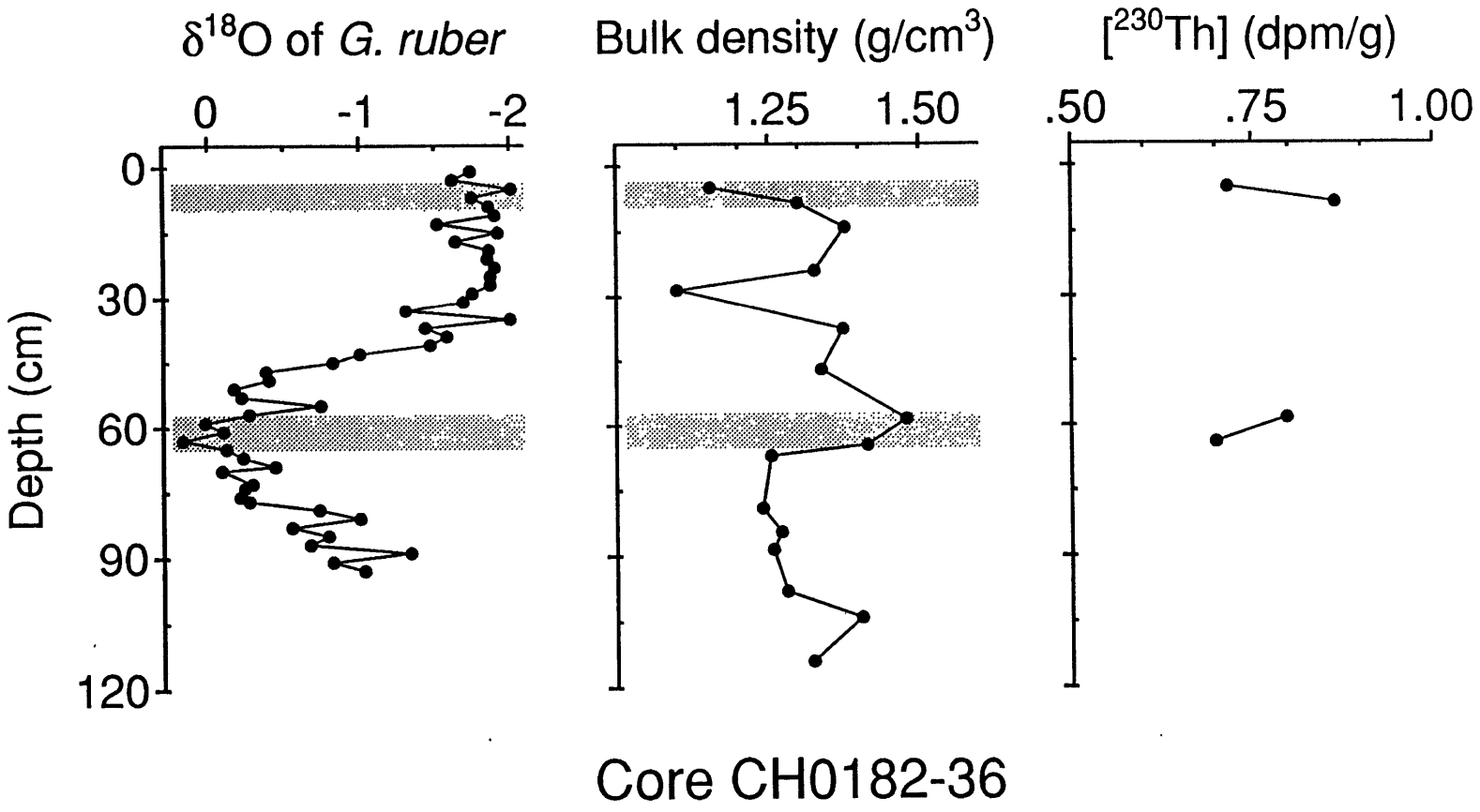
δ18O of G. ruber
0
-1
-2
Bulk density (g/cm3)
1.25
1.50
[230Th] (dpm/g)
.50
.75
1.00
Depth (cm)
0
30
60
90
120
Core CH0182-36

Figure 2.

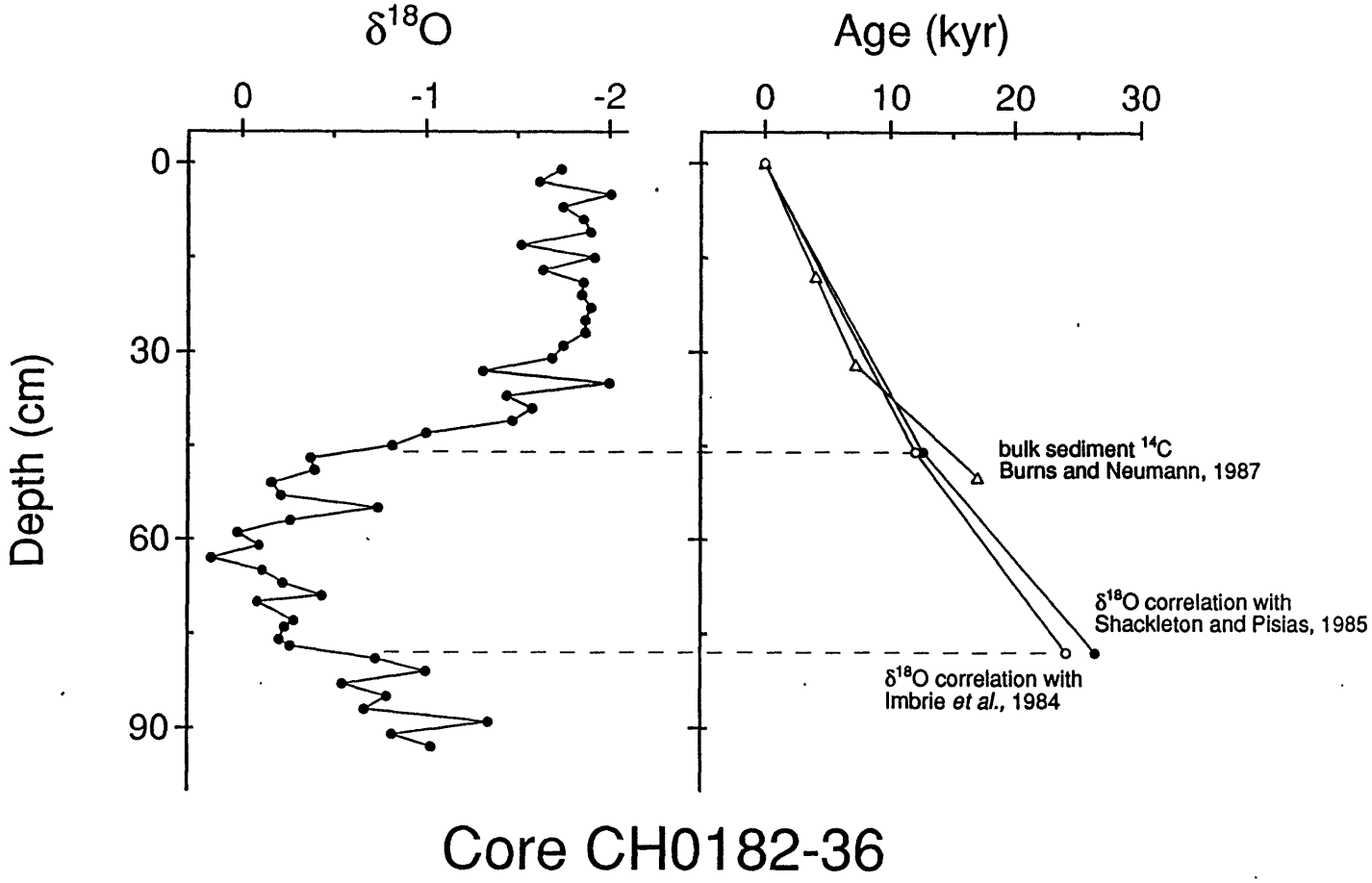
δ18O
0
-1
-2
Age (kyr)
0
10
20
30
Depth (cm)
0
30
60
90
bulk sediment 14C
Burns and Neumann, 1987
δ18O correlation with
Shackleton and Pisias, 1985
δ18O correlation with
Imbrie et al., 1984
Core CH0182-36

Figure 3.

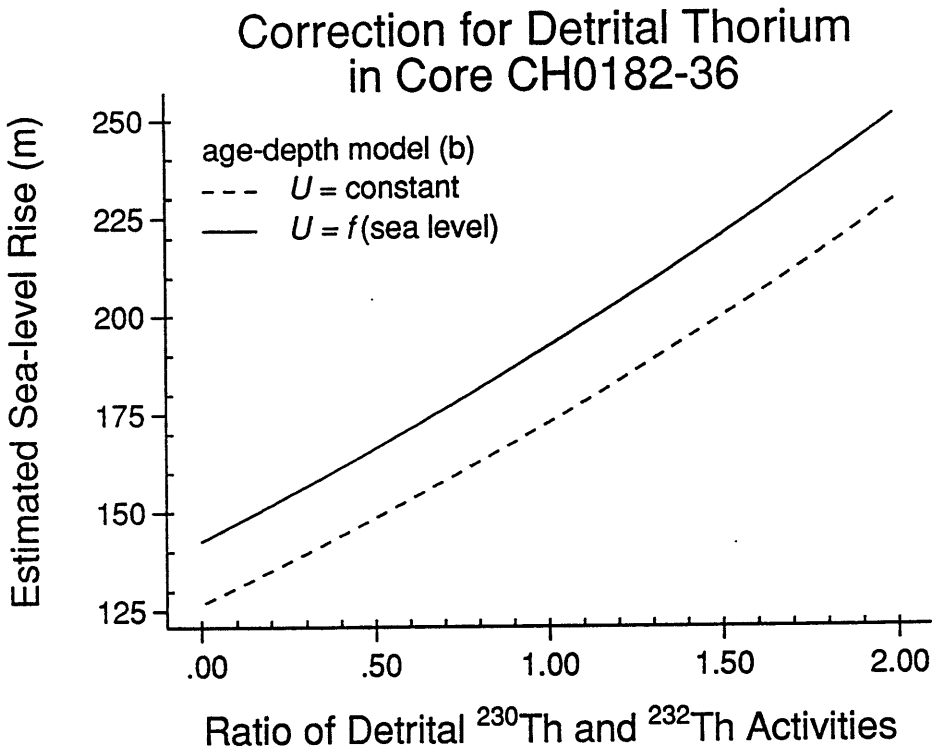
Correction for Detrital Thorium
in Core CH0182-36
Estimated Sea-level Rise (m)
250
225
200
175
150
125
age-depth model (b)
U = constant
U = f(sea level)
.00
.50
1.00
1.50
2.00
Ratio of Detrital 230Th and 232Th Activities

Figure 4.

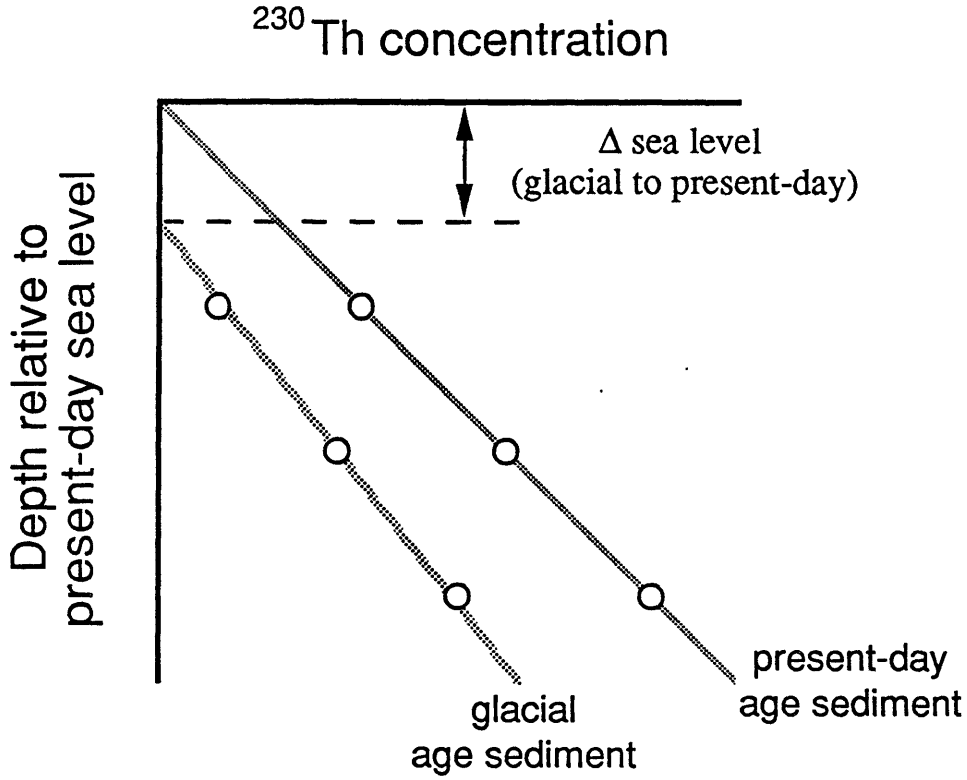
230Th concentration
Δ sea level
(glacial to present-day)
Depth relative to
present-day sea level
present-day
age sediment
glacial
age sediment

Figure 5.